

# Computational Modelling of a Resonant Microwave Cavity

A new method for obtaining sensitivity factors  
allowing the quantitative analysis of  
Time Resolved Microwave Conductivity data

Jim Sander Koning

# Computational Modelling of a Resonant Microwave Cavity

A new method for obtaining sensitivity factors  
allowing the quantitative analysis of  
Time Resolved Microwave Conductivity data

by

Jim Sander Koning

## **Master Thesis Applied Physics**

to obtain the degree of Master of Science at the Delft University of Technology  
to be defended publicly on Wednesday July 5, 2023 at 09:00 AM.

Department of Chemical Engineering  
Faculty of Applied Sciences  
Delft University of Technology

Student number:	4481674
Project duration:	September, 2022 - June, 2023
Thesis committee:	Dr. Ir. T.J. Savenije (supervisor) Prof. Dr. F.C Grozema Prof. Dr. E.H. Brück J. Nespoli (daily supervisor)

# Preface

*This master thesis was written to as a part of the last requirement to fulfill the Master degree of Science for Applied Physics at the Delft University of Technology. Although it does not encapsulate everything, it shows the most interesting results produced. Before starting the actual thesis, I would like to express my gratitude to all the individuals who were of importance the past months first.*

*Jasmeen, you were of great importance for my work. You continuously put in significant effort over the duration of my thesis I want to thank you for that. The steady, continuous support helped me at every step during my work. Despite our differences in background, you are for me a prime example that two different ways of thinking can still converge to the same conclusions.*

*Tom, I am grateful for your guidance during my thesis and granting me autonomy to perform my research. You were able to give feedback on the results, without delving into the computational methods I employed. Despite my stubbornness, you were often right, making me backtrack my mistakes and generating correct results.*

*I would like to extend my thanks to Jiashang for allowing me to use your samples. My vague requirements I set up for my experimental work and validation of the sensitivity of the microwave cavity fitted previous work of yours, and I got your samples without a single questions asked.*

*Ferdinand, I would like to thank you as well for allowing me to be a teaching assistant in one of your courses, resparking my joy in transferring knowledge to the younger generation. I actually forgot I liked teaching, but I won't forget again.*

*Adittionally, I would also like to express my thanks my fellow students starting the journey at approximately the same time as I did. Abhi, thanks for the laughs when it came to discussing code and coding. Clementine, thank you for assisting me with the TRMC setup during the start of the experiments. Jos  f, thanks for the support when it came to the course we assisted. Mourijn thanks for showing me knowledge beyond perovskites. Lennart, thanks the conceptual help, talks and constant laughs. I enjoyed my time in the student room, whether we were discussing, drinking coffee or working together.*

*Jim Sander Koning  
Delft, June 2023*

# Abstract

Photoactive layers in opto-electronic materials, e.g. solar cells are of high importance. They determine the efficiency of the absorbance of photons, allowing electrical energy to be harvested out of light. A key aspect of photoactive layer research is the analysis of charge carrier dynamics, investigated by Time Resolved Microwave Conductivity (TRMC). This is achieved by measuring the conductance ( $G$ ) of a sample after photoexcitation. First, a sample is placed in a resonant cavity. This cavity is energized by microwaves, generating a strong oscillating electric field. Next, a laser is pulsed to excite free charge carriers in the sample. These excited free charge carriers will be accelerated by the electric field, losing some energy in the process. This characterization method includes the usage of a sensitivity factor ( $K$ ), inherent to the shape and materials of the used of the resonant microwave cavity. This sensitivity factor can be determined in multiple ways, most of these methods include the experimentally obtained power reflection coefficient, either as a function of frequency and/or at the resonance frequency. Despite the importance of the sensitivity in TRMC measurements, it often receives minimal attention in different research groups around the world. The use of different resonant cavities by groups introduces inherent variations in sensitivity. As a consequence, quantitative analysis, sample comparison, and the comparability of findings across different research groups is hindered.

In this master thesis, a resonant cavity is modelled using a finite element method. This has been achieved by modelling the dimensions of the cavity cell and the relevant properties involved. This cavity has been computationally energized at varying frequencies, simulating the resonant characteristics. These modelled characteristics have been compared to the experimental results obtained during steady state microwave conductivity measurements. Furthermore, a novel method to determine the  $K$  factor and absolute sensitivity of a resonant microwave cavity is included, allowing precise quantitative research for thin film samples with varying dark conductance.

To determine the sensitivity factor, a thin film sample approximated as a transition boundary condition is placed on the surface of the quartz in the model. This allows the conductance ( $G$ ) of the sample to be varied numerically, while studying the power reflection coefficient at the resonant frequency. This allows the sensitivity factor to be calculated at  $K \approx -64,000$ . This corresponds in this model to a power reflection coefficient at resonance ( $R_0$ ) of  $R_0 = 0.64$ , induced solely by the quartz slide and a numerically modelled thin film with a thickness of 250 nm, conductance of  $G = 0$  S and relative permittivity ( $\epsilon_r$ ) of  $\epsilon_r = 30$ . When increasing the (dark) conductance, the  $K$  factor decreases monotonically, having asymptotic behaviour at  $R_0 \approx 0$ . This can be attributed to the factor  $R_0^{-1}$  present in its method of calculation, dominating the determined  $K$  factor.

Furthermore, the absolute sensitivity of the cavity has been studied numerically. This is defined as the change in power reflection coefficient, induced due to some conductance ( $dR/dG$ ). This absolute sensitivity increases approximately linearly with  $R_0$ , having a maximum at zero dark conductance with a value of  $dR/dG = -42,000$  showing opposite characteristics to the  $K$  factor.

The effect of the electric field strength on the obtained results during a TRMC measurement have been studied as well. This has been achieved by varying the power of the microwave generator. Literature describes various methods of determining the  $K$  factor, none being dependent on electric field strength (or indirectly: microwave power supplied). However, there are indications that the mobilities measured in TRMC are limited by grain size, hence possibly indirectly relating to electric field strength. However, no clear relation could be found in CsMAFA samples of 100 nm and 200 nm grain sizes between power supplied and mobility. This confirms that grain size is of little importance to the sensitivity of the resonant microwave cavity.

# Contents

<b>Preface</b>	<b>i</b>
<b>Summary</b>	<b>ii</b>
<b>Nomenclature</b>	<b>v</b>
<b>1 Introduction</b>	<b>1</b>
<b>2 Theoretical background</b>	<b>5</b>
2.1 Semiconductor fundamentals . . . . .	5
2.1.1 Valence-conduction band . . . . .	5
2.1.2 Photons . . . . .	6
2.1.3 Photovoltaic effect . . . . .	6
2.1.4 Conductivity . . . . .	7
2.1.5 Carrier (re)combination . . . . .	7
2.1.6 Prerequisites for current . . . . .	8
2.1.7 Drude model . . . . .	9
2.1.8 Carrier mobility . . . . .	10
2.1.9 Current due to mobility . . . . .	11
2.2 Electrodynamics fundamentals . . . . .	11
2.2.1 Maxwell equations . . . . .	11
2.3 Skin depth . . . . .	12
2.4 Waveguides . . . . .	14
2.4.1 Wave and phase velocity . . . . .	14
2.5 Resonant cavity . . . . .	15
2.5.1 Quality factor . . . . .	17
2.5.2 Power to electric field strength . . . . .	17
<b>3 Characterisation techniques</b>	<b>18</b>
3.1 Steady State Microwave Conductivity . . . . .	18
3.2 Time resolved microwave conductivity . . . . .	20
<b>4 Modelling</b>	<b>23</b>
4.1 Meshing . . . . .	23
4.1.1 Number of elements . . . . .	24
4.1.2 Element order shape . . . . .	24
4.1.3 Element order solution . . . . .	25
4.1.4 Meshing quality . . . . .	25
4.2 Solver . . . . .	25
4.2.1 Direct solver . . . . .	26
4.2.2 Iterative solver . . . . .	26
4.3 Geometry . . . . .	26
4.3.1 Iris modelling . . . . .	27
4.3.2 Grating modelling . . . . .	28
4.3.3 Perfectly matched layers . . . . .	29
4.4 Electrodynamics node . . . . .	30
4.4.1 Wave equation - Electric . . . . .	30
4.4.2 Wave equation - Lossy dielectric . . . . .	31
4.4.3 Impedance boundary condition . . . . .	31
4.4.4 Transition boundary condition . . . . .	31
4.4.5 Port excitation . . . . .	32
4.5 Calibration . . . . .	33

4.5.1	Empty cavity cell . . . . .	33
4.5.2	Quartz slide . . . . .	33
<b>5</b>	<b>Simulation details</b>	<b>34</b>
5.1	Simulation approach . . . . .	34
5.2	Simulation details . . . . .	35
5.3	Hardware and software details . . . . .	36
<b>6</b>	<b>Results and Discussion</b>	<b>38</b>
6.1	Steady state microwave conductivity . . . . .	38
6.1.1	Empty cavity cell . . . . .	38
6.1.2	Quartz slide . . . . .	39
6.2	Sample conductivity . . . . .	40
6.2.1	Electric field distribution . . . . .	42
6.2.2	Electric field along the surface of the sample . . . . .	45
6.3	Time resolved microwave conductivity . . . . .	47
6.3.1	K factor - signal strength . . . . .	47
6.3.2	K factor - high dark conductance . . . . .	47
6.3.3	Notes on previous work . . . . .	50
6.4	Simulation inaccuracies . . . . .	50
6.5	Influence of electric field strength . . . . .	51
<b>7</b>	<b>Conclusion</b>	<b>55</b>
7.1	Electric field distribution . . . . .	55
7.2	K factor for high dark conductance . . . . .	55
7.3	Power dependency on signal strength . . . . .	55
7.4	Summary . . . . .	56
<b>8</b>	<b>Outlook</b>	<b>57</b>
8.1	Time dependent studies . . . . .	57
8.2	Experimental validation . . . . .	58
8.3	Power dependency on signal strength . . . . .	58
	<b>References</b>	<b>59</b>
<b>A</b>	<b>Appendix A - Modelled geometry</b>	<b>63</b>
<b>B</b>	<b>Appendix B - Example job script</b>	<b>65</b>
<b>C</b>	<b>Appendix C - Cleaning of quartz slides</b>	<b>66</b>
<b>D</b>	<b>Appendix D - Electric field distribution for various conductivities</b>	<b>67</b>
<b>E</b>	<b>Appendix E - SSMC at various powers</b>	<b>70</b>
<b>F</b>	<b>Appendix F - Absorption spectra</b>	<b>72</b>
<b>G</b>	<b>Appendix G - Domain sizes</b>	<b>73</b>

# Nomenclature

## Abbreviations

Abbreviation	Definition
FEM	Finite Element Method
FWHM	Full Width Half Maximum
LHS	left hand side
PBS	Parallel Batch System
RHS	right hand side
SCP	Secure Copy Protocol
SSMC	Steady State Microwave Conductivity
TE <sub>mnl</sub>	Transverse Electric (mode mnl)
TRMC	Time Resolved Microwave Conductivity

## Symbols

Symbol	Definition	Unit
$a$	Length of cavity	m
$A$	Surface area	m <sup>2</sup>
$\vec{a}$	Acceleration	m/s
$b$	width of cavity	m
$c$	Speed of light	m/s
$dR/dG$	Absolute sensitivity	S <sup>-1</sup>
$\vec{D}$	Electric displacement field	V/m
$e$	Elementary charge	C
$E_c$	Conduction band energy	eV
$E_v$	Valence band energy	eV
$E_g$	Band gap energy	eV
$\vec{E}$	Electric field	V/m
$\vec{E}_i$	Incidence electric field	V/m
$\vec{E}_r$	Reflected electric field	V/m
$f$	Frequency	s <sup>-1</sup>
$f_{mn}$	Cutoff frequency of mode $mn$	s <sup>-1</sup>
$F_A$	Fraction of absorbed light	[ - ]
$\vec{F}$	Force	N
$\vec{F}_L$	Lorentz force	N
$G$	Conductance	S
$\Delta G$	Induced photoconductance	S
$h$	Planck constant	J/Hz
$\vec{H}$	Magnetic field strength	A/m
$I_0$	Incidence photon density	cm <sup>-3</sup>
$\vec{j}_f$	Free current density	A/m <sup>2</sup>
$k_0$	Free space wavevector	rad/m
$K$	K factor, calibration factor	S <sup>-1</sup>
$KR_0$	Absolute sensitivity	S <sup>-1</sup>
$L$	Thickness of sample	m

Symbol	Definition	Unit
$m$	Mass	kg
$n$	$n$ factor of cavity, calibration factor	[ - ]
$n_0$	Density of free electrons	$\text{cm}^{-3}$
$\delta n(t)$	Photoinduced density of electrons	$\text{cm}^{-3}$
$\vec{n}$	Normal vector	[ - ]
$p_0$	Density of free holes	$\text{cm}^{-3}$
$\delta p(t)$	Photoinduced density of holes	$\text{cm}^{-3}$
$P_i$	Incidence power	W
$P_r$	Reflected power	W
$P_{ref}$	Reference power	W
$\vec{p}$	Momentum	$\text{kg}\cdot\text{m/s}$
$Q$	Quality factor	[ - ]
$R(f)$	Power reflection coefficient	[ - ]
$R_0$	Power reflection coefficient at resonance	[ - ]
$S_{11}$	Scattering parameter for a 1 port system	[ - ]
$t$	Time	s
$U_{diss}$	Average dissipated energy/cycle	J
$U_s$	Average total electromagnetic energy stored/cycle	J
$V_r$	Reference voltage	V
$\Delta V$	Change in voltage	V
$\vec{v}$	Velocity	$\text{m/s}$
$\langle \vec{v} \rangle$	Average velocity	$\text{m/s}$
$\alpha$	Number of charge carriers	[ - ]
$\delta$	Penetration depth	m
$\epsilon$	Absolute permittivity	F/m
$\epsilon_0$	Vacuum permittivity	F/m
$\epsilon_r$	Relative permittivity	[ - ]
$\sigma$	Conductivity (general)	$\Omega\text{m}$
$\sigma_0$	Conductivity (dark)	$\Omega\text{m}$
$\sigma(t)$	Conductivity (transient)	$\Omega\text{m}$
$\mu$	Absolute permeability	$\text{N/A}^2$
$\mu_0$	Vacuum permeability	$\text{N/A}^2$
$\mu_n$	Mobility of electrons	$\text{cm}^2/\text{Vm}$
$\mu_p$	Mobility of holes	$\text{cm}^2/\text{Vm}$
$\mu_r$	Relative permeability	[ - ]
$\lambda$	Wavelength	m
$\tau$	Scattering time	s
$\phi$	Yield/efficiency	[ - ]
$\Omega$	Angular frequency	$\text{rad/s}$

# Introduction

Global energy consumption has increased significantly over the past decades, followed by a skyrocketing in the use of fossil fuels accompanied by a rise in average global carbon emission. Future scenarios are highly uncertain and highly dependent on policies adopted by the global system. The energy consumption globally is widely anticipated to increase over the coming decades, with ideal scenarios focusing on shifting away from fossil fuels to so renewable sources to reduce harm full emissions in the atmosphere. One of these options is solar energy, allowing energy to be harvested using solar cells. [41]

Since the sun provides a reliable and virtually inexhaustible source of energy that is able to sustain the world's energy need, solar energy has the potential to become a leading factor in the generation of energy in the coming years. Furthermore, prices have decreased over the year, making solar a more attractive option for generation of energy [12]. Extensive research has been conducted over the past decades and has enhanced the overall performance of solar devices. Significant advancements have been made, as shown by the historic chart in figure 1.1, which showcases record efficiencies achieved across different types of photovoltaic technologies.

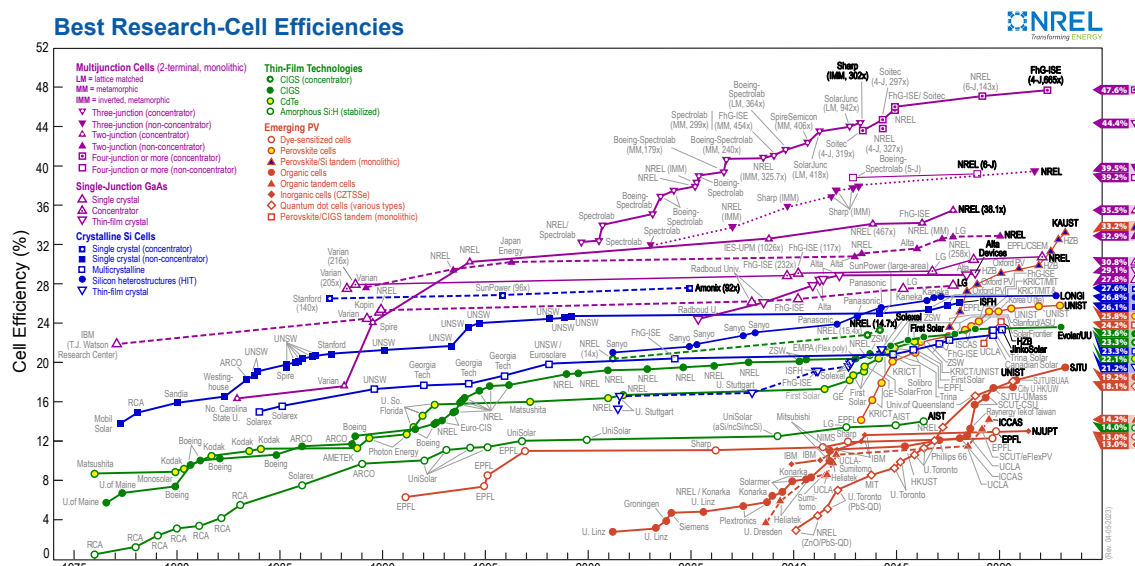


**Figure 1.1:** The innovations in photoactive layers research. Efficiencies of various types has been rapidly increasing over the past few years, with many new types of opto-electronic layers being developed over past decades. Taken from [39].

It is projected that solar energy will be adopted more in the coming years to meet the growing global energy consumption as the world is making an attempt to transition to more sustainable energy. [41]

One of the important aspects of solar cells are the photoactive layers responsible for the generation of excited charge carriers. In these layers, the main focus is generation of electron-hole pairs that are able to generate current. Hence, it is usually preferred to have a high efficiency in the generation of mobile charge carriers to have a high conversion to electrical power. Furthermore, these excited charge carriers must have a sufficiently high mobility to allow the generated charges to be extracted from the photoactive layer to other components, such as electrodes or transport materials, producing a current.

One of the vital components in solar cell research is the characterization of these photoactive layers. One of such methods is Time Resolved Microwave Conductivity (TRMC), allowing the charge generation dynamics of photovoltaic devices to be studied. This method has already been used for decades and has been used thoroughly in literature. It uses a microwave source to generate a high oscillating electric field in a resonant cavity, interacting with charges generated by a laser pulse. These generated charges will be accelerated by the electric field in the cavity, losing some power in the process that is measured by the setup. A schematic of a cavity used during a TRMC measurement is given in figure 1.2.

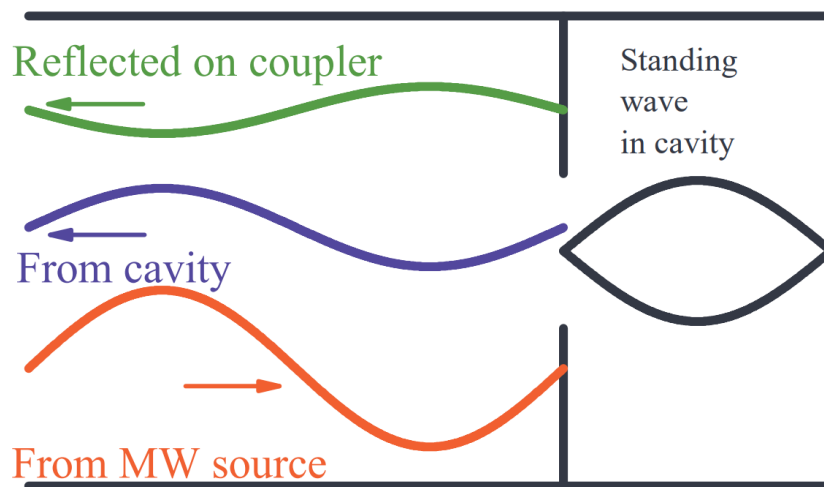


**Figure 1.2:** Schematic of a waveguide coupled with a microwave cavity. The waveguide (shown on the left) is a rectangular structure with highly conductive walls, guiding microwaves to travel in a low-loss manner. Shown on the right, a resonant cavity, allowing standing waves to form due to the harmonic nature of a superposition of incident electromagnetic waves. Both the waveguide and resonant cavity are coupled using an iris, a hole in a thin metallic plate allowing a fraction of electromagnetic energy to travel between waveguide and cavity. Taken from [24].

The exact quantities of power reflected from the coupler, power leaking from the cavity and induced losses is not clear in current literature. Although approximations exist [56] [48] [45], these are only valid for 'perfect' resonators, adhering to specific unrealistic requirements which are not valid in practical measurements. An cavity cell used in experimental work is shown in figure 1.3

In recent years, the semiconductor industry has made big advancements in the increase of computing power. This makes it possible to model complex systems using numerical methods such as the finite element method (FEM). This allows calculation of properties that are not available analytically due to complex shapes or complex systems. Using this new computing power, the microwave cavity of the TRMC shown in figure 1.3 can be modelled using the FEM. This allows the exact characteristics of the cavity, such as electric field strength, to be computationally obtained. This allows an exact quantification of the signals obtained by the TRMC characterization method, such as photoconductance and the product of the yield and mobility. In specific, the power reflection coefficient of the microwave cavity will be modelled due to various dark conductances of a thin film sample during a Steady State Microwave Conductivity (SSMC) measurement. This (computational) dark conductance can be due to various unspecified reasons, with the requirements that it is constant during a measurement and inherent to the material studied. These results will be related to the sensitivity of the cavity during a TRMC measurement, in which the conductance will be induced due to a laser pulse.

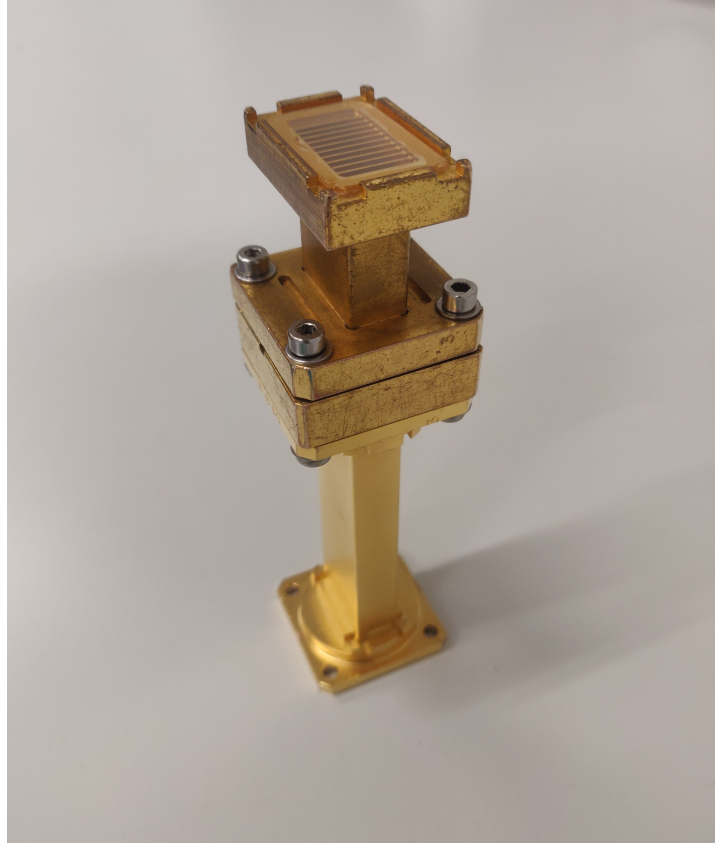


**Figure 1.3:** Figure of the studied TRMC cell. At the top of the figure the grating is shown, allowing (pulsed laser) light to pass through. The bottom can be connected to a waveguide to excite the cavity with electromagnetic energy. More images can be found in appendix A

To arrive at the sensitivity, usually described as the  $K$  factor, the formulas historically used in literature [53] [48] will be rewritten as an explicit derivative, not previously described in literature. This allows the  $K$  factor to be determined in a seemingly continuous manner for various dark conductances. Since the  $K$  factor does not contain all the information of the system, also the relatively new term *absolute sensitivity* formulated by Reid et al. in 2017 will be calculated. The absolute sensitivity will also be derived as an explicit derivative, allowing it to be derived for various dark conductances in a continuous manner.

Furthermore, in current literature there is no relation between the electric field strength and the measured signals using SSMC and TRMC. However, there are indications that electric field strength plays a role in the measured mobilities using TRMC, especially when the grain sizes are relatively small [49]. By varying the microwave power, the electric field strength in the cavity can be varied, allowing electric field strength to be studied. If a (significant) relation exists between microwave power and measured mobilities, the  $K$  factor should be reevaluated to incorporate this dependence.

In literature, various research groups utilize different TRMC setups with varying microwave cavities [48][53][8]. This leads to a disparity in the sensitivity of these microwave cavities among research groups. Consequently, comparing researched samples becomes challenging since identical samples can yield different signal strengths based on the cavity used. Ideally, each research group employing a microwave cavity should accurately and fairly determine the  $K$  factor, enabling precise comparisons of samples. However, currently research groups make minimal efforts to determine the sensitivity of their microwave cavities, resulting in qualitative research rather than quantitative. Moreover, comparing samples between groups is exceedingly difficult due to the varying sensitivity factors. In the current approach, "freely" choosing sensitivity factors may inadvertently create a misleading perception of sample performance. By accurately determining the  $K$  factor, TRMC signals can be precisely

quantified, thereby offering fair insights into researched semiconductor materials. Ideally, each group should conduct an analysis to determine the sensitivity of their own resonant microwave cavities as a global academic effort to aid in thin film semiconductor research. In this thesis, the sensitivity of the resonant microwave cavity used by the Opto-electronic Materials group of the Delft University of Technology will be determined for various dark conductances of a thin film sample, by the use of the FEM, which requires accurate modelling the geometry of the cavity, while simultaneously modelling the equations that govern the electromagnetic behaviour of the microwave cavity. Furthermore, a novel method is developed to determine the sensitivity of the resonant microwave cavities for varying dark conductances of thin film samples.

Summarized, this thesis will aim to answer the following research questions:

1. What is the electric field distribution in the resonant microwave cavity used during SSMC and TRMC measurements.
2. What is the  $K$  factor of this resonant microwave cavity and how is this influenced by dark conductance of the sample?
3. What is the absolute sensitivity of this resonant microwave cavity and how is this influenced by dark conductance of the sample?
4. How does the electric field strength in the resonant microwave cavity influence the measured signals during a SSMC and TRMC measurement?

To answer these objectives, first a theoretical background will be established in chapter 2. This chapter is designed to develop a basic understanding of the underlying physical principles of the the following chapters. Next in chapter 3 the characterization techniques SSMC and TRMC will be discussed. This chapter will start of in the usual manner often found in literature and theses, giving an overview of the setup and current knowledge. However, this chapter will also be used to introduce the new method to determine the sensitivity factors, both the  $K$  factor and absolute sensitivity. Afterwards, the underlying physical principles used in the modelling of the cavity will be discussed in chapter 4. This chapter will be mainly focused on the governing equations describing the different characteristics of the microwave cavity. This will build a understanding of the electromagnetic principles governing the cavity. This will also include the governing equations used in the commercial FEM software COMSOL [38] used in the model. The computational requirements used to simulate the model will be described in chapter 5. Furthermore, software used to simulate the model will be discussed as well. A link to the Github repository containing the code used to analyze the data to arrive at the results is included as well. The results and discussion are given in chapter 6. This will also include (some of) the limitations of the model and the possible effects on the results. This is followed by the conclusion in chapter 7, summarizing the most important results. Lastly, possible future research opportunities will be discussed in chapter 8. Additionally, some options will be discussed to address the limitations of the model.

# 2

## Theoretical background

### 2.1. Semiconductor fundamentals

Semiconductor devices are described by devices that have specific properties in terms of band structure. These properties are understood generally well by the use of quantum physics. In this thesis, mainly the optoelectronic properties of a bulk semiconductor will be discussed. This will include notions of structure and electric properties that arise due to the interaction with light.

#### 2.1.1. Valence-conduction band

Semiconductors usually present bonds between atoms leading to a crystalline or polycrystalline structure. A structure like this is a solid, with an arrangement of atoms or molecules in a specific pattern, generating a three dimensional periodic lattice structure. An example of the spatial structure of a semiconductor is shown in figure 2.1. A unit cell, the smallest possible method of describing a repeating crystal structure is shown on the left, while on the right the connection with its neighbouring unit cells is shown.

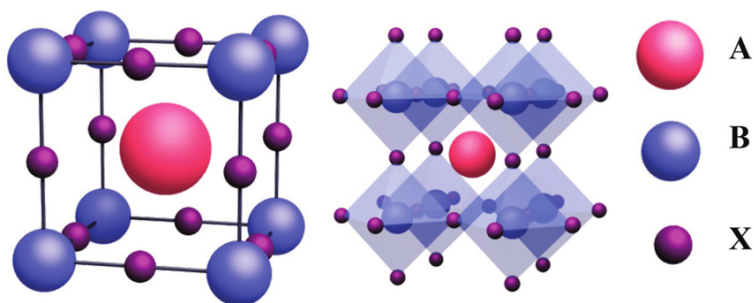


**Figure 2.1:** On the left, a unit cell of a perovskite with structure  $ABX_3$ : a semiconductor material currently subject to extensive research. On the right, an extended version showing how the unit cell is placed in a periodic lattice. Adapted from [67].

This pattern of placement of atoms and molecules is repeating in 3D. Each unit cell shares the B cations with its neighbouring cells, as shown in figure 2.1. The electrons in the lattice have wavefunctions, assigning probabilities to the radial location of their electron. However, due to the nature of the repeating lattice, these wavefunctions will start to overlap due to the discrete available spacing for each atom. This overlapping of wavefunctions will generate discrete energy levels the electrons are able to occupy. More precisely, the Pauli exclusion principle states that identical particles with a half integer spin, such as electrons and their respective holes, cannot occupy the same quantum state within a system simultaneously. Since all these particles are in the same system, due to their placement in the reciprocal lattice, a maximum of two half spin particles, with opposite spin, can occupy the same energy level [40]. This results in the fact that all electrons will occupy the lower energy levels, up to a

specific energy dependent on temperature.

In semiconductors, the allowed energy levels are aligned in such a way that it requires a specific amount of energy to excite an electron to a higher allowed energy level. Specifically for semiconductors, a gap between allowed energies exists, requiring a minimum energy ( $E_G$ ) to cross this (band)gap. This allows an electron to be promoted from the valence band with an energy  $E_v$  to the conduction band with an energy of  $E_c$ . A schematic of the allowed energy levels are shown in figure 2.2.

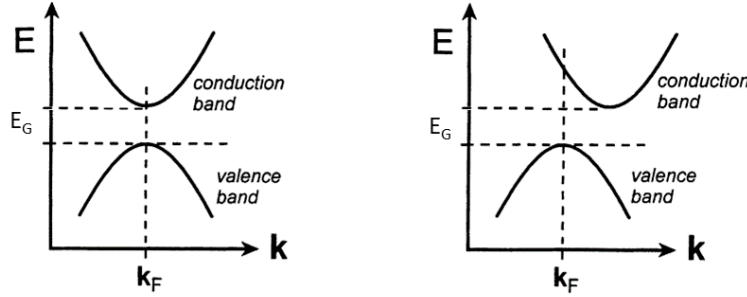


**Figure 2.2:** Direct bandgap of a semiconductor shown on the left, while an indirect bandgap is shown on the right. The energy between the bandgap is denoted here as  $E_G$ . Adapted from [1].

In this figure, the x axis represents the k-vector, representing the momentum space. This can loosely be understood as a momentum vector in classical physics [33]. The y axis represents energy. Only the states along the 'curve' of the valence band or conduction band can be occupied with either electrons or holes. In semiconductors, electrons are mainly occupying the valence band, while their counterpart holes are mainly occupying the conduction band [40].

### 2.1.2. Photons

To generate energy in a photovoltaic cell, or more specific: excite electrons to the conduction band, we need a source of energy. This energy is in the form of a photon, an elementary quantum particle with a discrete energy in the form of electromagnetic energy. A photon is massless, hence always moves at the speed of light, yet is still able to carry energy. The energy a photon carries is defined in equation 2.1.

$$E_{ph} = hf = \frac{hc}{\lambda} \quad (2.1)$$

Here,  $E$  is the energy,  $h$  the Planck constant ( $6.626 \cdot 10^{-34}$  Js),  $f$  the frequency ( $s^{-1}$ ),  $\lambda$  the photon's wavelength (m) and  $c$  the speed of light ( $2.9979 \cdot 10^8$  m/s). To harvest the energy of light, one needs to convert the photon energy to mobile charges and utilize the properties of these charges. [40]

### 2.1.3. Photovoltaic effect

After an electron is promoted to the conduction band due to absorption of a photon and its counterpart, hole, left in the valence band, free charges are created. However, for this in order to happen, the photon must have an energy above the bandgap energy of the material i.e.  $E_{ph} > E_g$ . A schematic of this is given in figure 2.3.

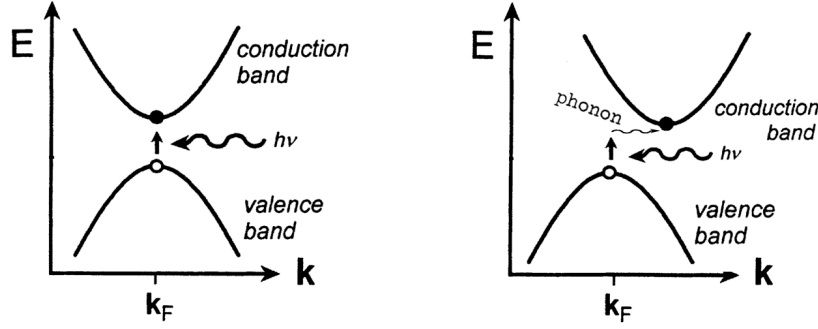


**Figure 2.3:** Excitation of an electron to the conduction band. Adapted from [1].

Here it is important to notice two differences between the graphs shown in figure 2.3. In the first example the material has a direct bandgap. In a direct bandgap the electron can be excited to the conduction band with only the required photon energy. However, when an indirect bandgap is present, as is in many semiconductor materials, extra energy is required to put the electron in the conduction band. This energy is obtained from the one or multiple phonons, i.e a lattice vibration in the crystal structure. In most photovoltaic devices, a direct bandgap is preferred. This is because extracting a phonon from the lattice is usually less efficient, and hence induces a lower overall efficiency [2].

#### 2.1.4. Conductivity

Conductivity is the description how well a material is able to conduct electricity, giving rise to a current of charged electric particles moving (on average) in a specific direction. The conductivity is denoted by  $\sigma_0$  and its units in Siemens per meter (S/m). In matter the conductivity is often given as in equation 2.2 [40].

$$\sigma_0 = e \cdot (\mu_n n_0 + \mu_p p_0) \quad (2.2)$$

Here,  $e$  is the absolute elementary electronic charge,  $\mu_n$  and  $\mu_p$  the mobility of electrons or holes in units  $\text{cm}^2/\text{Vs}$ , and  $n_0$  and  $p_0$  the density of free electrons and holes respectively with no influence of light, in units of  $\text{cm}^{-3}$ . The mobility is an intrinsic property of the lattice structure. One can have many free electrons and holes, but if the mobility is low, the rate at which charge can be transported will be lower, hence being represented by a lower conductivity [40].

#### 2.1.5. Carrier (re)combination

It is of importance to distinguish background conductivity, inherently present due to either temperature, impurities or various other reasons, from the generated charge carriers due to incident light. This allows opto-electronic materials to be studied with a conductivity in dark. Using TRMC, only transient exposure will be studied, e.g. illumination due to a laser pulse. The conduction after transient illumination is given in equation 2.3.

$$\sigma(t) = e \cdot (\mu_n (n_0 + \delta n(t)) + \mu_p (p_0 + \delta p(t))) \quad (2.3)$$

Now,  $\delta n(t)$  is the concentration of free electrons and  $\delta p(t)$  the free concentration of holes induced, both due to a transient exposure [40]. The excited electrons and holes will decay back to their respective bands over time. This decay is (usually) always decreasing and some function of material properties [29], in specific recombination mechanisms. These recombination characteristics can be studied using the TRMC technique described in chapter 3.2. This technique has been used to characterize opto-electronic materials for decades now [16] [29] [51] [52].

Although not thoroughly discussed in this thesis, different recombination mechanisms play a role in the recombination of a excited electron-hole pair. Some of the more common recombination mechanisms can be found in figure 2.4.

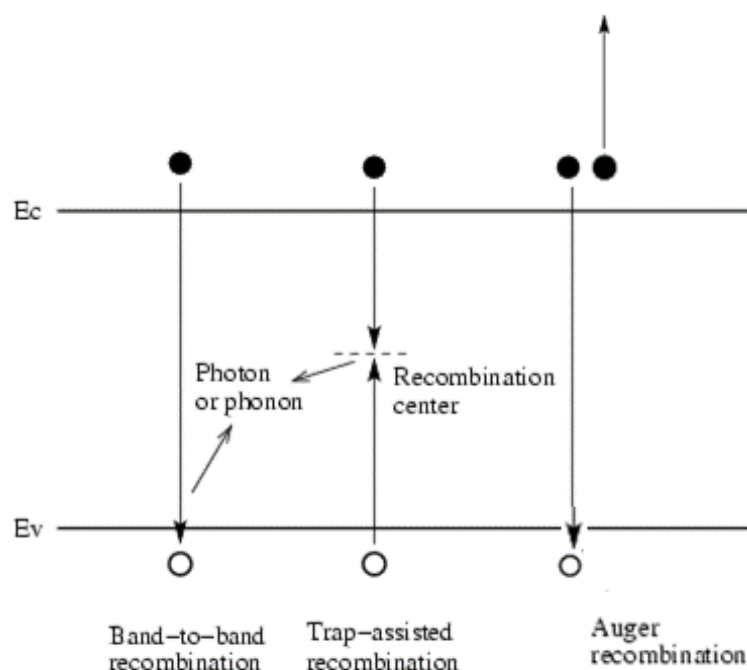


**Figure 2.4:** Relaxation of an electron to the conduction band. Some of the more common/well known recombination mechanisms are displayed. Adapted from [43].

The first recombination mechanism is a band to band transition. The release of energy is in the form of a photon (radiative), or lattice vibration (nonradiative). The second recombination mechanism is a trap assisted recombination. Here, first either a hole or electron is trapped in the trap state, making it a bound charge, but filling the trap state. Next, one opposite charge carrier is trapped in the trap state, where the pair now recombines, releasing either a photon or phonon. Lastly, the Auger recombination requires three particles, two equal charged particles, and 1 opposite charged particle. Here, a band to band transition happens while the energy released from this band to band transition is released to a other free charge carrier [43]. This free charge carrier will increase in energy, ideally exciting more electrons hole pairs to lose the excess energy obtained. In this thesis, no distinguishment will be made what type of recombination is present. But recombination plays a major role in making semiconductor devices [40], research [9] and the characterization technique TRMC studied later in chapter 3.2.

### 2.1.6. Prerequisites for current

Current is defined as the net movement of charges. The net movement of charges can be accomplished in many ways, but in this thesis only the generation of current due to the presence of an electric field is of importance. In the presence of an electric field, the electrons and holes gain momentum due to their elementary charge. Applying an external electric field will accelerate charges, resulting in a non-symmetric distribution of momentum of these electrons and holes. Effectively resulting in a current [55]. However, the material must have (induced) conductive properties, i.e have both holes and electrons in their valence and conduction band. An schematic of this is given in figure 2.5.

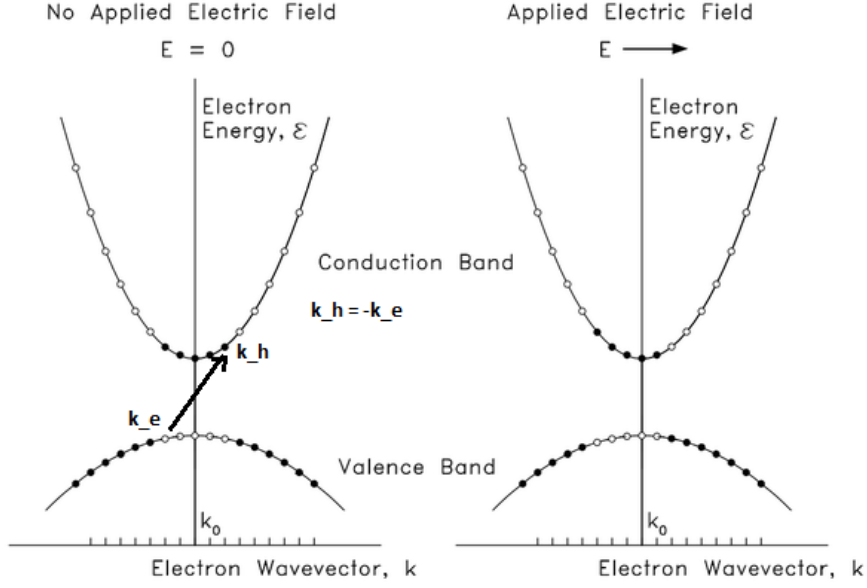


**Figure 2.5:** Excitation of some electrons and holes to their respective band. Next, the effect of an externally applied electric field is shown on the locations of the holes and electrons in  $k$  space. Image taken from [6]

In a full band, an applied electric field generates no current because any change in momentum is cancelled out by another electron/hole, with equal sign momentum, but in the opposite direction. Only partial filled bands are able to generate a net nonzero wavevector, hence a nonzero movement of charges, which is the definition of an electric current [55]. Although not explicitly described in this thesis, at some nonzero temperature nearly all semiconductors will have some electrons in the conduction band, with their corresponding holes in the valence band. This is due to electrons having some (probabilistic) energy, allowing some electrons to jump to the conduction band, creating an electron-hole pair. Due to the high number of electrons present in these studied semiconductors, there is always a density of electrons in the conduction band [40].

### 2.1.7. Drude model

Charged particles will be subjected to a force in the presence of an electric field. In specific for electrons and holes in a semiconductor, an applied external electric field will accelerate these charge carriers provided there are available energy states in the conduction and valence band. Many different models can be derived to find the equations of motion for an electric field in the presence of an externally applied electric field. In this example the Drude model will be presented, a simple kinetic model of electronic motion. In semiconductors where there are only very little free charge carriers present in the material, this model is usually a good approximation [55].

To arrive in an intuitive manner to the Drude model, it is recommended to start with (quasi) classical mechanics. Starting with the Lorentz force on a charged particle with elementary charge  $\pm e$ . Here the particle can either be considered a hole or electron, dependent on charge and mass. Masses don't have to be equal and can vary based on material studied. In the remaining of this chapter, no explicit distinction will be made in the formulas between holes and electrons, but plugging in the correct masses their respective charges will work to derive the material properties described later such as  $m = m_{e/h}$ ,  $\tau = \tau_{e/h}$ ,  $\vec{v} = \vec{v}_{e/h}$ , and  $\mu = \mu_{e/h}$ .

$$\frac{d\vec{p}}{dt} = m\vec{a} = \vec{F}_L = \pm e(\vec{E} + \vec{v} \times \vec{B}) \quad (2.4)$$

Here,  $\vec{p}$  is the momentum,  $t$  the time,  $m$  the mass,  $\vec{a}$  the acceleration,  $\vec{F}_L$  the Lorentz force,  $\vec{E}$  the electric field,  $\vec{v}$  the velocity and  $\vec{B}$  the magnetic flux density. Now, to arrive at the Drude model in a semiconductor, some assumptions are made. These are listed below [55]:

1. The magnetic field  $\vec{B}$  applied is  $\vec{0}$ . This is not a requirement for the Drude model in general, but in context of this thesis it is correct.
2. The electron/hole scattering time is  $\tau$ , this is how long an electron is allowed to move, before it collides with its environment. The probability of scattering within some time interval  $dt$ , equals  $dt/\tau$ . Furthermore, this will reset the momentum to  $\vec{0}$ . This is shown in equation 2.5

$$m\vec{v}(t + dt) = \vec{0} \quad (2.5)$$

3. In between these scattering events, the particle responds to the electric field postulated by the Lorentz force. The probability of this happening in a time interval  $dt$  equals  $1 - dt/\tau$ . The effect on the particles momentum is given in equation 2.6.

$$m\vec{v}(t + dt) = m\vec{v}(t) + \vec{F}_L dt \quad (2.6)$$

Now, to find the average momenta of these electrons/holes one can use the equations above and their corresponding probabilities.

$$m\langle\vec{v}(t + dt)\rangle = \frac{dt}{\tau}\vec{0} + \left(1 - \frac{dt}{\tau}\right)(m\langle\vec{v}(t)\rangle + \langle\vec{F}_L\rangle dt) \quad (2.7)$$

Working out the brackets recognizing that when  $\lim_{dt \rightarrow 0}$  we can neglect the  $dt^2$  terms.

$$m\langle\vec{v}(t + dt)\rangle = m\langle\vec{v}(t)\rangle + \left(\langle\vec{F}_L\rangle - m\frac{\langle\vec{v}(t)\rangle}{\tau}\right) dt + \mathcal{O}(dt^2) \quad (2.8)$$

Now, realizing the elementary definition of the derivative:

$$\frac{\langle\vec{v}(t + dt)\rangle - \langle\vec{v}(t)\rangle}{dt} = \frac{d}{dt}\langle\vec{v}(t)\rangle \quad (2.9)$$

And substituting this derivative:

$$m\frac{d}{dt}\langle\vec{v}(t)\rangle = \frac{m\langle\vec{v}(t)\rangle}{\tau} + \langle\vec{F}_L\rangle \quad (2.10)$$

For simplicity, a static electric field will be imposed, with no magnetic field component, and the Lorentz force will be explicitly substituted for the electric field. Furthermore, the system is allowed to establish an equilibrium. This will allow a steady state solution to form, setting the left hand side (LHS) to zero. This will finally result in the equations of motion for this system.

$$m\langle\vec{v}\rangle = \pm e\tau\vec{E} \quad (2.11)$$

This is for the average velocity of charge carriers in semiconductors. This solution is not universal, and only suitable for the approximations described in this chapter. However, this solution is the easiest to derive, and allows for calculation of semiconductor properties.

### 2.1.8. Carrier mobility

Now, one can define the mobility of either an electron or hole, given as the responsiveness of mobile charge carriers in the presence of an electric field.

$$\mu = \frac{|\vec{v}|}{|\vec{E}|} = \frac{e\tau}{m} \quad (2.12)$$

Important to note here is that mobility is defined as a positive value, requiring a notation of the positive charge. Intuitively, this is a function of the effective mass, and scattering time. A lower effective mass results in a higher mobility. The same applies to a higher scattering time, allowing longer accelerations and hence mobilities. Mobilities are an important characteristic in optoelectronic devices, with usually high mobilities preferred over low mobilities.

### 2.1.9. Current due to mobility

It can be considered of interest to now revisit section 2.1.4, where the conductivity is derived. Since the definition of current density ( $\vec{j}$ ) is given by the number of charge carriers (denoted  $\alpha$  to represent either the number of electrons or holes) multiplied by the velocity and elementary charge.

$$\vec{j} = -e\alpha\vec{v} = \frac{e^2\tau\alpha}{m}\vec{E} = \sigma\vec{E} \quad (2.13)$$

The right hand side (RHS) of equation 2.13 is well known as Ohm's law. One can now substitute the conductivity found in equation 2.13 with the definition of the mobility found in equation 2.12 [2].

$$\sigma = e\alpha\mu \quad (2.14)$$

Which is comparative to the conductivity derived in section 2.1.4. One should observe that the total current is simply the superposition of both the hole and electron current [55]. Unorthodoxly, the conductivity can also be considered as a superposition of both the electrons and holes conductivity. Both holes and electrons have their own separate contribution to the material properties in semiconductors although in reality these are never decoupled. These combined conductivities will result in the overall characteristics of the semiconductor.

## 2.2. Electrodynamics fundamentals

Some background in electrodynamics is required to understand the TRMC technique and model discussed in chapter 3 and 4. Some important concepts will be highlighted and derived to understand the wavelike characteristics that will play a role later on in this thesis.

### 2.2.1. Maxwell equations

The goal of this section is to derive the wave equation for the electric field in space. The most important equations in electrodynamics are the Maxwell equations; equation 2.15 is Gauss's law for the electric field, equation 2.16 is Gauss's law for magnetism, equation 2.17 is the Ampere-Maxwell equation in matter and finally equation 2.18 is Faraday's law in differential form. These equations are in many cases the foundations for many lines of work in electromagnetics. Since in this thesis, the Maxwell equations are the foundation for solving the electric field distribution (computationally) later on, the derivation is given in this section.

$$\nabla \cdot \vec{D} = \rho_f \quad (2.15)$$

$$\nabla \cdot \vec{B} = 0 \quad (2.16)$$

$$\nabla \times \vec{H} = \vec{j}_f + \frac{\partial \vec{D}}{\partial t} \quad (2.17)$$

$$\nabla \times \vec{E} = -\frac{\partial \vec{B}}{\partial t} \quad (2.18)$$

In these equations,  $\vec{D}$  is the electric displacement field,  $\rho_f$  is the free charge density,  $\vec{H}$  is the magnetic field strength and  $\vec{j}_f$  the free current density. To relate the  $\vec{D}$  and  $\vec{H}$  fields to their respective  $\vec{E}$  and  $\vec{B}$  fields, equation 2.19 and equation 2.20 can be used.

$$\vec{D} = \epsilon\vec{E} \quad (2.19)$$

$$\vec{H} = \frac{1}{\mu}\vec{B} \quad (2.20)$$

Here,  $\epsilon$  is the absolute permittivity and  $\mu$  the absolute permeability. Important to note that the permittivity is the product of the relative permittivity and the permittivity of vacuum, i.e.  $\epsilon = \epsilon_r\epsilon_0$ . The permeability behaves comparatively, i.e.  $\mu = \mu_r\mu_0$ , where  $\mu_r$  is the relative permeability and  $\mu_0$  the permeability of vacuum.

To arrive at partial differential equation that is solvable without requiring a system of equations, one should start at taking the curl on both sides of Faraday's law (in differential form) given in equation 2.18, this results in equation 2.21.

$$\nabla \times (\nabla \times \vec{E}) = -\frac{\partial}{\partial t} \nabla \times \vec{B} \quad (2.21)$$

Substituting the Ampere Maxwell equation (2.17) in the right hand side (RHS) arrives at:

$$-\nabla \times (\nabla \times \vec{E}) = \mu \frac{\partial \vec{j}_f}{\partial t} + \mu \epsilon \frac{\partial^2 \vec{E}}{\partial t^2} \quad (2.22)$$

If one assumes a time independent conductivity, we can substitute Ohm's law (given in equation 2.23), in equation 2.24.

$$\vec{j}_f = \sigma \vec{E} \quad (2.23)$$

Assuming a time independent, isotropic permeability one can split the permeability and permittivity and rearranging equation 2.22.

$$-\nabla \times \left( \frac{1}{\mu_r} \nabla \times \vec{E} \right) = \sigma \mu_0 \frac{\partial \vec{E}}{\partial t} + \epsilon_r \mu_0 \epsilon_0 \frac{\partial^2 \vec{E}}{\partial t^2} \quad (2.24)$$

Next, if one proposes the ansatz for a time harmonic wave with a constant frequency

$$\vec{E}(\vec{r}, t) = \vec{E}(\vec{r}) e^{j\omega t} \quad (2.25)$$

Substitution of equation 2.25 in equation 2.24 arrives us at:

$$\nabla \times \left( \frac{1}{\mu_r} \nabla \times \vec{E} \right) - \mu_0 (\epsilon_r \epsilon_0 \omega^2 - j\sigma \omega) \vec{E} = \vec{0} \quad (2.26)$$

To increase readability, one can plug in the wavenumber of vacuum ( $k_0$ ) given in equation 2.27.

$$k_0 = \omega \sqrt{\epsilon_0 \mu_0} = \frac{\omega}{c_0} \quad (2.27)$$

Now, finally this arrives at:

$$\nabla \times \mu_r^{-1} (\nabla \times \vec{E}) - k_0^2 (\epsilon_r - \frac{j\sigma}{\omega \epsilon_0}) \vec{E} = \vec{0} \quad (2.28)$$

Which is the governing equation for the electric field excited by a time harmonic source. For later reference, equation 2.28 is the equation used in the modelling later on in this thesis for the propagation of an electromagnetic wave.

## 2.3. Skin depth

An electromagnetic wave incident on a material with any nonzero conductivity properties will alter its electromagnetic amplitude in the material itself. A parameter of this behaviour is the skin depth. The skin depth is given as the distance an electromagnetic wave can penetrate an material where its amplitude is reduced to  $e^{-1}$  (37%) of its original value [66]. The (simplified) relation for skin depth is given in equation 2.29.

$$\delta = \sqrt{\frac{2}{\omega \mu_0 \mu_r \sigma}} \quad (2.29)$$

Here,  $\delta$  is the skin depth in meters and  $\sigma$  the conductivity. A plot of the conductivity and skin depth is for a nonmagnetic material is given in figure 2.6.

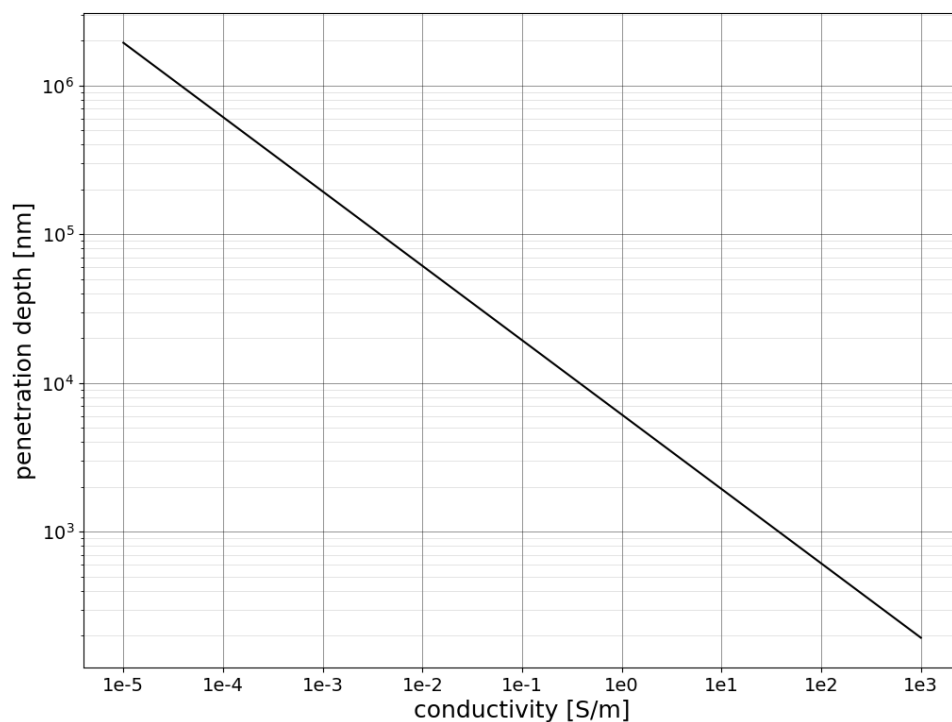


**Figure 2.6:** Penetration depth of a nonmagnetic material with an electromagnetic wave with the frequency of 8.5 GHz.

This graph can be used as a justification for chapter 4, where an incident electric field on a highly conductive material will barely penetrate the material. Furthermore, figure 2.6 can be used as a reference for (thin film) samples to see how an incident electric field drops off in the material.

## 2.4. Waveguides

To transport electromagnetic radiation in a low-loss manner, waveguides are used. These waveguides are specifically designed to use the properties of electromagnetic waves, mainly the matching conditions at surfaces or internal interfaces to guide the propagation of electromagnetic waves to desired locations. In this thesis, a waveguide consists of a electromagnetically reflecting boundaries (copper walls) with a specific shape encapsulating a low-loss material (air). The total electromagnetic field inside the waveguides is generally well understood in literature, using its properties extensively to transmit signals [66]. The electric field distribution inside a waveguide is given in figure 2.7.

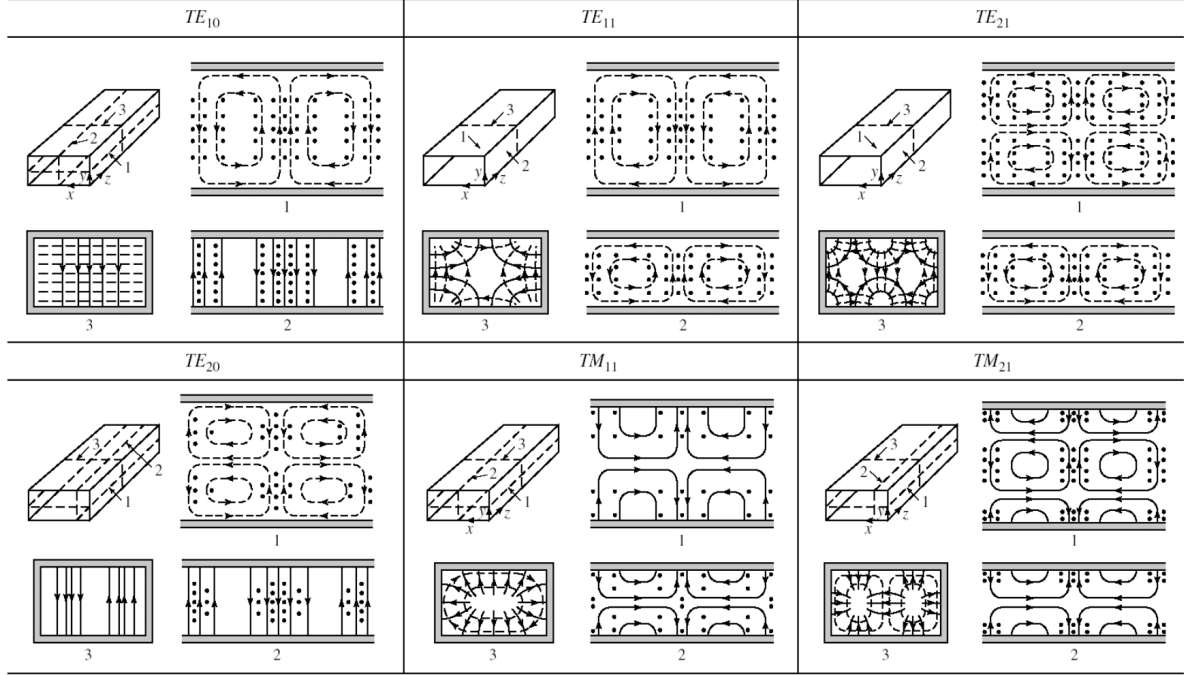


**Figure 2.7:** The lower possible waveforms in a rectangular waveguide. The solid lines denote the electric field, while the dotted lines represent the magnetic field. Taken from [10].

The wavepatterns formed in the cavity are dependent on the dimensions of the cavity and the frequency applied. In general two modes exist: transverse electric, with the electric field being only in the direction perpendicular to propagation, and transverse magnetic, with the magnetic field being perpendicular to the direction of propagation. Which modes are available in the waveguide depend on the applied frequency and the size of the waveguide. With higher order modes only existing in either higher frequencies, or generally thinner waveguides. In this thesis, only the transverse electric 10 ( $TE_{10}$ ) mode is dominant in the system.

### 2.4.1. Wave and phase velocity

When multiple waves are propagating together, their constructive and destructive characteristics will result in a superposition of the waves. The same principle holds in waveguides. Here, the electric field is due to the superposition of multiple electromagnetic waves scattering in the waveguide, resulting in the pattern described in figure 2.7. The lowest possible wavelength that can propagate (corresponding to the cutoff frequency) of a rectangular waveguide corresponds to double the length of the widest section of a rectangular waveguide.

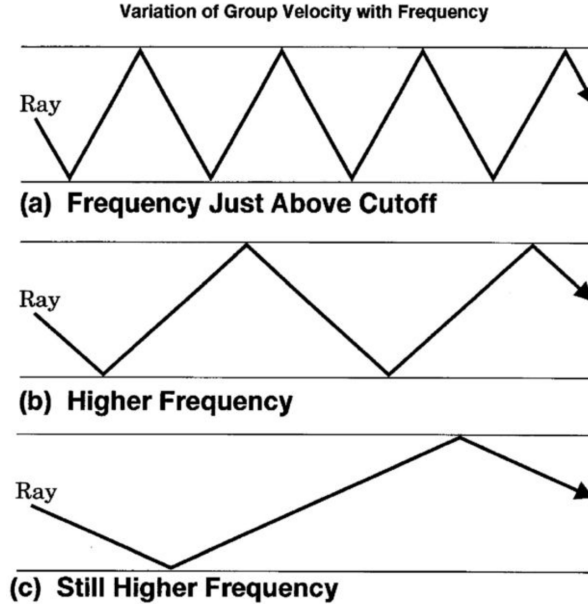


**Figure 2.8:** 2D Schematic a ray path in a waveguide with varying frequency. Taken from [62]

The speed at which the individual rays travel along the length of the waveguide (group velocity) is lower than the speed of light. This is due to the increased path length, as described in figure 2.8. However, the phase of the electric field, generated by the superposition of each individual ray, travels along the waveguide faster than the speed of light [18]. The phase velocity ( $v_p$ ) for a waveguide is given in equation 2.30.

$$v_p = \frac{c}{\sqrt{\mu_r \epsilon_r}} \frac{1}{\sqrt{1 - (f_{mn}/f)^2}} \quad (2.30)$$

Here,  $f_{mn}$  is the cutoff frequency and  $f$  the excitation frequency. In this thesis specifically, an X-band waveguide is used, with standardized dimensions, having an cutoff frequency of 6.557 GHz in the context of this thesis [50]. In resonant cavities (described in chapter 2.5), the usual frequencies do not align with the cavity's dimensions. The higher phase velocity that arises compensates for the mismatch by increasing the wavelength along the direction of power transfer. As a result, standing waves can form within the resonant cavities, creating a unique resonance effect.

## 2.5. Resonant cavity

Electromagnetic resonant cavities are characterized by the fact that they are able to amplify the electromagnetic radiation by means of trapping the power temporarily. These cavities are enclosed structures where the dimensions are usually around the same magnitude as their operating wavelength. To establish resonance, the following principles play a role:

1. The electromagnetic energy is supplied by using a waveguide, allowing the electromagnetic energy to propagate towards the cavity.
2. The cavity is separated by means of a coupler. This is usually an iris, namely a hole in a thin metallic plate. This will form the boundary between waveguide and cavity, reflecting some power, and allowing some power to pass through. Furthermore, some power of the cavity leaks back out through the coupler.
3. At specific resonant frequencies, the dimensions of the cavity will relate to the excitation wavelength of the electromagnetic waves sent out by the microwave generator, allowing a standing wave to form within the cavity. This will amplify the electric and magnetic fields compared to the source.
4. The cavity is made of (good) conducting walls. This is a requirement since the amplified electric field inside the cavity will induce currents in the walls, inducing power losses. A higher conductivity of the walls will decrease losses [66].

As discussed before, only specific frequencies are able to form a standing wave, creating constructive interference. This only happens at discrete frequencies, specified by equation 2.31

$$f_{mnl} = \frac{c}{2\sqrt{\mu_r\epsilon_r}} \sqrt{\left(\frac{m}{a}\right)^2 + \left(\frac{n}{b}\right)^2 + \left(\frac{l}{d}\right)^2}, \quad (2.31)$$

Here,  $a, b, d$  are the lengths of the sides of an arbitrary shaped rectangular cuboid,  $m, n, l$  positive integers representing the number of antinodes of the electric field along their respective lengths, and  $c$  the speed of light in vacuum. Described later in this thesis, a cavity will be used as well. Treating this real world cavity with dimensions  $48 \times 10.16 \times 22.86 \text{ mm}$  as an example [53], a resonant frequency of this cavity will be  $f_{201} = 9.056 \text{ GHz}$ . The standing waveform of this ideal cavity is shown in figure 2.9.

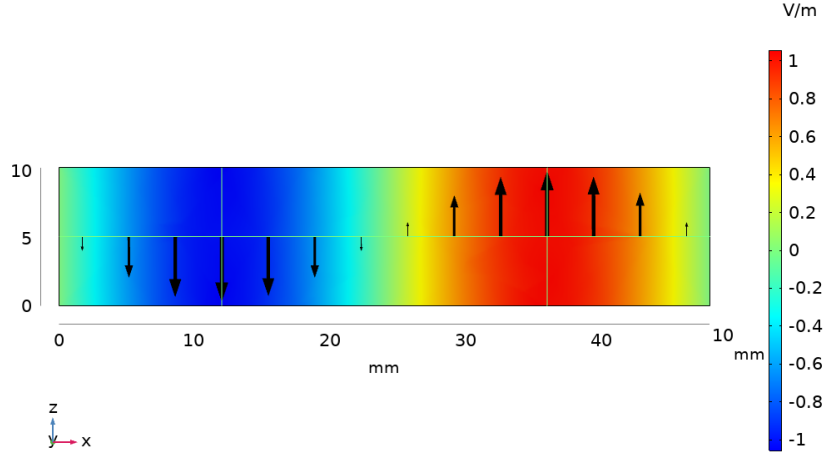


**Figure 2.9:** Normalized standing wave pattern of a  $TE_{201}$  formed in a cavity after excitation. Only the electric field is shown. The coupling iris is omitted for simplicity. Here,  $a, b, d$  are in the  $y, z, x$  direction.

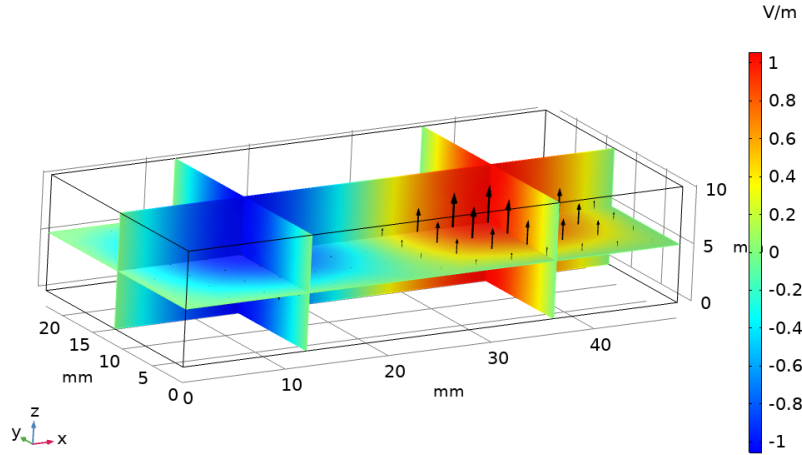


**Figure 2.10:** Normalized standing wave pattern of a  $TE_{201}$  formed in a cavity after excitation. Shown with a different view to highlight the  $y$  direction. Here,  $a, b, d$  are in the  $y, z, x$  direction.

One can see that in a resonant cavity with a  $TE_{201}$  waveform, the maximum of the electric field will be at  $1/4$  and  $3/4$  in the  $x$  direction of the cavity. Furthermore, this field in the cavity will be oscillating defined by the phase velocity, as described by equation 2.30.

### 2.5.1. Quality factor

The quality factor is in literature one of the most important properties of a resonant cavity. A higher quality factor prescribes better resonant properties by definition, given in equation 2.32.

$$Q \equiv 2\pi \frac{U_s}{U_{dis}} \quad (2.32)$$

Here,  $Q$  is the quality factor,  $U_s$  the average total electromagnetic energy stored in the cavity and  $U_{dis}$  the energy dissipated per cycle [44]. This dissipation is either due to leakage back out of the cavity to the waveguide, or due to Joule heating induced by the electric field in the walls of the cavity [66]. Since these properties are often hard to determine analytically, a different representation of the  $Q$  factor is given in equation 2.33.

$$Q = \frac{f_{mnl}}{FWHM} \quad (2.33)$$

Here,  $FWHM$  is the full width at the half maximum of the power reflection coefficient [65]. This will be described in more detail in chapter 3.

Usually when using cavities, the interaction between a material and electric or magnetic field inside the cavity is studied during measurements. Hence a higher  $Q$  factor is usually preferred, representing a higher energy stored, hence a higher electric and magnetic field oscillating in the cavity.

### 2.5.2. Power to electric field strength

In a cavity, the distribution of the waveform is independent on the power used to supply the cavity [31], since the spatial distribution is independent, a simple conversion can be done between incidence power and electric field strength. This means that if the electric field distribution in the cavity is known for a specific power, it can be scaled for all powers. The relevance of this scaling will be clarified in chapter 3 and 4. This scaling relation is given in equation 2.34.

$$\sqrt{\frac{P_{i,2}}{P_{i,1}}} \vec{E}_1 = \vec{E}_2 \quad (2.34)$$

Here,  $P_{i,1}$  is the incidence power with a known electric field  $E_1$ , and  $P_{i,2}$  a new incidence power with a scaled, unknown electric field  $\vec{E}_2$ .

In chapter 4, a model will be developed with a reference incidence power of  $P_{i,1} = 1$  W. To scale the corresponding electric field with the correct powers, the following scaling factors have been used:

$$\frac{\vec{E}_{1,empty}}{2.5586} = \vec{E}_{2,empty} \quad (2.35)$$

For the loaded cavity with a quartz slide inserted in the cavity, at the location corresponding with approximately maximum electric field strength, the scaling is as following:

$$\frac{\vec{E}_{1,quartz}}{2.4859} = \vec{E}_{2,quartz} \quad (2.36)$$

The difference in power is due to the nonlinear power characteristics across different frequencies of the microwave generator. In all further work, when a figure of the electric field strength is shown, this is the electric field at the usual maximum power of the setup for easier interpretation of the results.

## Characterisation techniques

Two measurement techniques will be studied, both closely related and using the same principle: resonator cavities. The first measurement technique is SSMC. This technique studies the characteristics of a material at various frequencies. In specific, a thin film semiconductor mounted on a quartz slide. Furthermore, this is a technique that only probes steady state properties. This can be either in dark conditions or during continuous illumination. The second measurement technique is TRMC. This technique measures at a single (resonant) frequency to maximize sensitivity. This is achieved by illuminating a thin film semiconductor mounted on a quartz reference plate with a pulsed laser, indirectly probing the electron/hole pair generation, decay and mobility over time.

The resonant cavity used for both these experimental methods is not a perfect resonator as described in chapter 2.5. Figures with the inner dimensions are found in appendix A. The most important deviations from a perfect cavity are as following.

1. A grating is included in the cavity to enable around 80% of light to be transmitted. This grating allows laser light to pass through without diffraction, but is designed in such a way that it stills allow resonant properties in the microwave range. However, the discontinuities of the resonator walls influence the resonant properties.
2. An thin polymer membrane is placed in front of the iris. This is to seal the cavity from ambient air, which can interact with the sample placed inside. This effect on the resonant properties should be minimal.
3. The quartz slide, sample, the indentation to hold the quartz slide, coupling iris and grating will perturb the standing waveform. The waveform will still approximately behave as described in chapter 2.5, having two antinodes and three nodes along the length of the cavity. However, the spacing, and corresponding electric field intensity between these nodes will be non-uniform. The distribution of the electric field will later be studied in the results.

### 3.1. Steady State Microwave Conductivity

SSMC is a non-destructive, non-invasive method of probing dielectric properties of unknown materials. This technique is pioneered by radar technology development during World War 2, with scientific research already using the properties of resonant cavities to probe dielectric properties in 1946 [36]. SSMC utilizes the increase of the electric field in the resonant cavity. This is achieved by placing a quartz slide with a thin film sample in the cavity at the location of maximum electric field. Next, a microwave source sends out electromagnetic waves through an X-band waveguide designed for frequencies between 8.2 – 12.4 GHz to the cavity [46]. A schematic of this setup is given in figure 3.2. Note that during SSMC, the laser is turned off, varying only the frequency of the microwave generator. Ideally, the properties of the sample can be quantified by comparing them to a reference quartz slide. This allows the properties of the thin film to be probed by comparing the difference with a reference.

As stated before in section 2.5, only at, and close to these frequencies a standing waveform can be

formed. A standing waveform also means that the cavity stores this energy, raising the electric field strength by multiple orders of magnitude inside the cavity. A thin film sample with a conductivity will react with the oscillating electric field, introducing an additional power loss. Furthermore, the permittivity of the thin film will shift the resonant frequency. Since the permittivity of a semiconductor is generally higher than air, the shift of frequency will be to lower frequencies. Intuitively, this can be derived from equation 2.31.

An SSMC measurement comprises of a minimum of three components: (1) A measurement of the reflected power of the resonant cavity, with a sample placed inside, while the frequency is swept along frequencies, and (2) a reference measurement of the reflected power of the cavity with a reflecting flat plate placed at the location of the iris, while the frequency is swept along the same frequencies. Finally, (3) the frequency scan should be normalized appropriately using equation 3.1.

$$R(f) = \frac{P_r(f)}{P_i(f)} \quad (3.1)$$

The power reflection coefficient ( $R(f)$ ) is a function of frequency, allowing the exact resonance frequency to be determined. In microwave engineering, this property is often denoted as  $\Gamma(f)$ , but in context of SSMC/TRMC  $R(f)$  is more appropriate. Furthermore,  $P_r(f)$  is the power reflected back with the cavity connected, decreasing in value around the resonant frequencies due to induced losses in the cavity. Lastly,  $P_i(f)$  is the incident power, measured using the backplate in step (2) above. Some losses will incur due to the microwaves having to travel through the waveguide and back towards the measurement source, but these can be neglected. Now,  $R(f)$  can be used to locate the resonant frequencies and study the dark conductivity. Figure 3.1 shows a schematic of effect of the sample properties on a SSMC measurement.

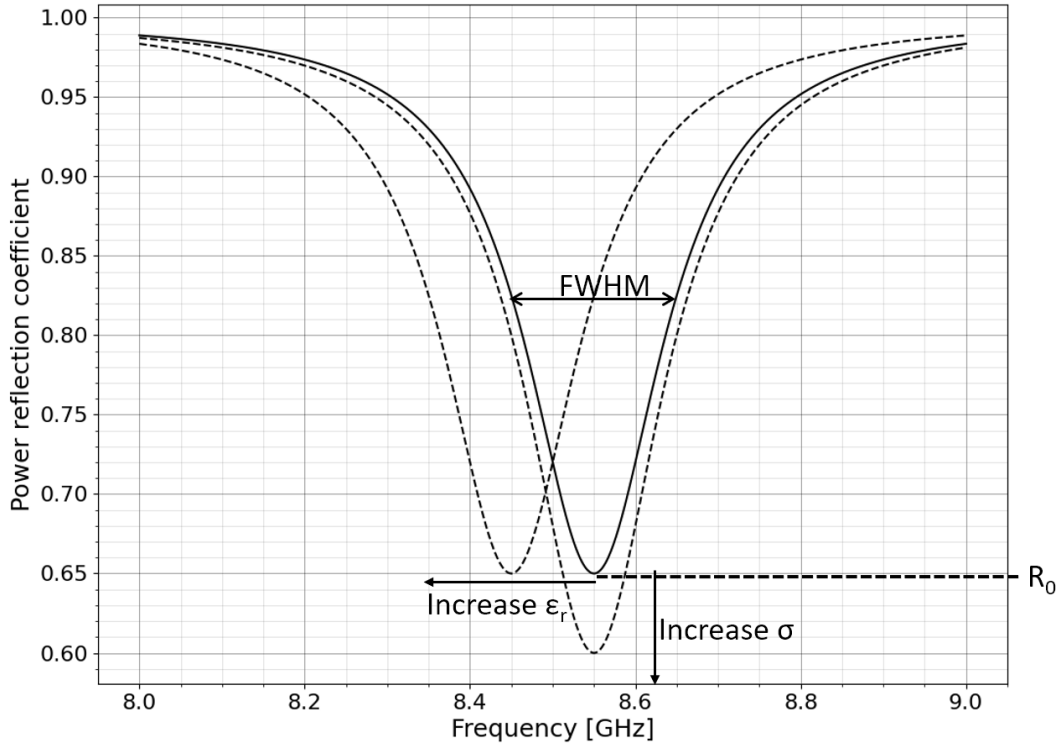


**Figure 3.1:** Schematic of normalized SSMC measurement. The effect of a sample's material is shown, increasing the permittivity will shift the resonance frequency slightly to lower ranges. Furthermore, increasing the conductivity will shift the resonance dip down. The full width half maximum is also shown for the solid line. Furthermore the power reflection coefficient at resonance is denoted as  $R_0$ .

### 3.2. Time resolved microwave conductivity

With TRMC the dynamics of charge carrier in materials as a function of time can be studied after illumination with a light pulse. The usage of TRMC increased during the 1960 when the interest in semiconductors such as silicon and germanium increased [44]. More recently, TRMC is being used in the characterisation of (thin film) perovskites [29] since this technique allows the study of photo-induced charge separation and charge recombination. Resonant cavities, due to their ability to store power higher than the microwave generator supplies, allows small variations in dielectric properties to be measured with relatively low noise.

To probe the charge carrier dynamics after illumination, a laser beam is send using an Ekspla NT342B pulsed laser to generate 3 – 5 ns wide optical pulses at a frequency of 10 Hz. Next, these pulse(s) are passed trough metallic neutral density filters to vary the amount of photons to a desired amount ranging between  $10^9$  up to  $10^{14}$  photons/cm<sup>2</sup> in this setup [29]. These photons will excite electrons from the valance band to the conduction band and holes from the conduction band to the valence band, resulting in an increase in conductivity (see equation 2.2). These transient photo-generated carriers absorb some power due to the acceleration induced by the time harmonic electric field in the resonant cavity. This photo-induced power absorption is measured by the electronics, resulting in an initial signal. After illumination, the generated charge carriers will recombining and falling back to the ground state over time, resulting in less absorption of power and hence a time dependent signal [48] [29]. This change in reflected microwave power is (ideally) only influenced by the change in conductivity over time. A schematic of the TRMC setup is shown in figure 3.2.

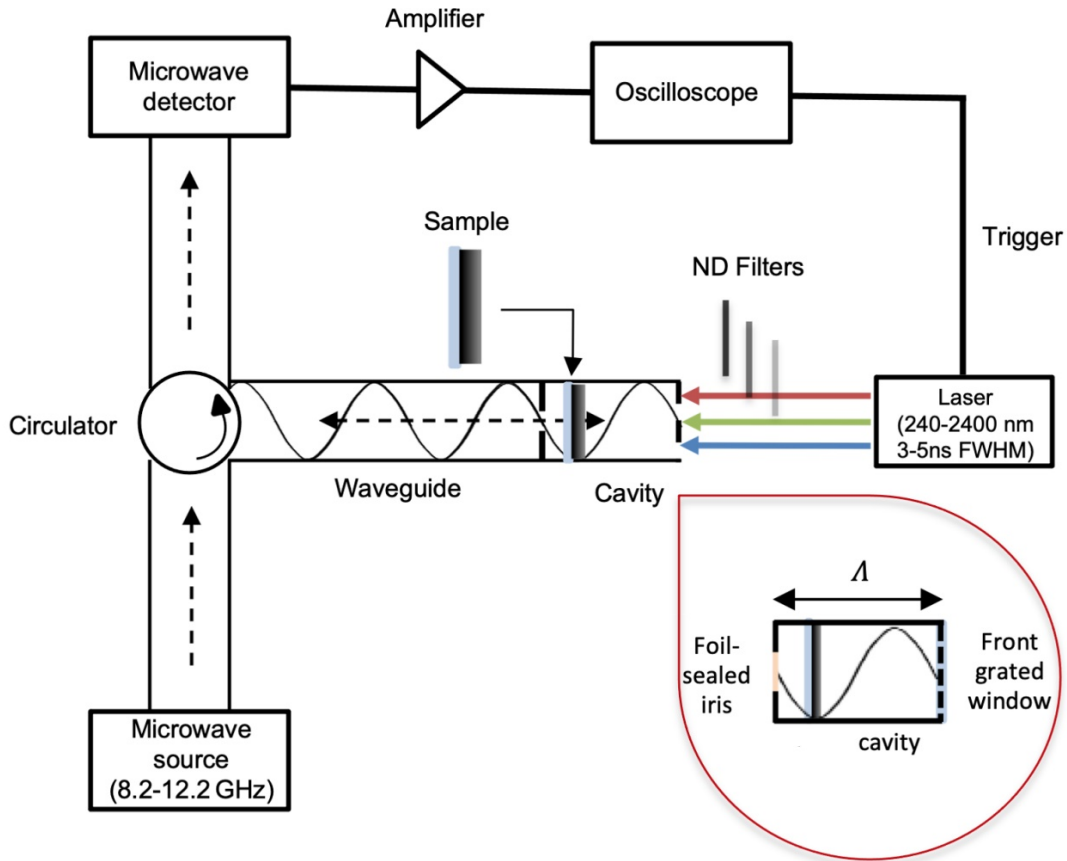


**Figure 3.2:** Schematic of the TRMC/SSMC set-up and zoomed in on the resonant cavity, showing a simplified version of the electric field incoming in the resonant cavity. In this example, the sample is mounted on a quartz slide (not explicitly defined). The sample is placed at 3/4 the length of the cavity, which approximately corresponds to a local maxima of the electric field. A more exact description of the resonant cavity will be given in chapter 4.3. Taken from [11]

The goal of the TRMC technique is to relate the measured reflected microwave signal to the intrinsic material properties. The intrinsic properties of importance here are the conductance and the product of

the yield and mobility of these photo induced charge carriers. An issue in this technique is that although the cavity has well defined physical dimensions, the resonant cavity has some physical properties that are unknown (although usually approximated) that influence the measured reflected signal. Some of these unknown properties are the exact electric field distribution across the sample, the influence of a quartz slide in the cavity and induced losses in the cavity.

To arrive at an expression for the reflected signal strength and the intrinsic material properties, it is wise to first start at the definition of conductance ( $G$ ), given in equation 3.2.

$$\Delta G = \Delta \sigma \frac{A}{l} = \Delta \sigma \frac{aL}{b} \quad (3.2)$$

Here,  $\Delta \sigma$  is the change in conductivity due to illumination,  $A$  the surface area perpendicular to the direction of the current flow generated by the alternating electric field (in the direction of the generated electric field) and  $l$  the length of the material in which the current flows through [48]. In this thesis with the waveform studied, the surface area orthogonal to the electric field is given as  $a \times L$ , where  $a$  is the sample height, and  $L$  the thickness of the sample, and  $b$  the width of the sample. These dimensions correspond to the inner dimensions of the X-band waveguide, and are denoted explicitly at the right side of appendix A. The generation of charge carriers (and hence conductance across the sample) might not be linear. However, for this thesis, a uniform conductance is approximated [51].

Measuring electric field strength, or the reflection coefficient is not trivial. To measure the (varying) reflected electric field, a Schottky barrier diode is placed in the waveguide terminator. This Schottky diode is able to measure the electric field strength, and outputs this as a voltage. The voltage over this diode is related to the electric field strength in the following manner:

$$n \cdot \frac{\Delta V}{V_r} = \frac{\Delta P}{P_{ref}} \quad (3.3)$$

Here,  $P_{ref}$  is the power reflected initially before illumination,  $\Delta P$  the change in reflected power reflected power due to absorption of power by excited charge carriers ( $\Delta P = P_{signal} - P_{ref}$ ). On the LHS of equation 3.3 something comparable is present. Here,  $\Delta V_r$  is the change in voltage reported by the diode due to a change in reflected power, induced by illumination.  $V_r$  the reference voltage reported at  $P_{ref}$ . The factor  $n$  is a calibration factor, allowing the (device specific) voltage characteristics of the diode to be translated to the change in electric field.  $n$  is not a constant since realistic diodes are non-linear and is internally used in the software as a lookup table.

The RHS of equation 3.3 can be further simplified (see equation 3.4) to allow for an arbitrary power, i.e

$$\frac{\Delta P}{P_{ref}} = \frac{\Delta R_0}{R_0} \quad (3.4)$$

Here,  $R_0$  is the power reflection coefficient at resonance in the steady state, schematically shown in figure 3.1 and  $\Delta R_0$  the change in power reflection coefficient due to illumination. The assumption is made that the cavity is (ideally) over/under coupled. Hence  $R_0$  is ideally 'far' from zero [48]. Now, to relate this to the material properties, in specific conductance, one can use equation 3.5 [51].

$$\frac{\Delta P}{P_{ref}} = \frac{\Delta R_0}{R_0} = -K \Delta G \quad (3.5)$$

With the sensitivity factor ( $K$ ), obtained in equation 3.6

$$\frac{\Delta R_0}{\Delta G} \frac{1}{R_0} = -K \quad (3.6)$$

In literature,  $K$  is often described as a (dimensionless) constant number. An option to obtain the values for  $K$  for various  $\frac{\Delta R_0}{R_0} / \Delta G$  is to either do measurements with samples with known conductances in a SSMC measurement. However, within the TU Delft a in-house program was introduced, modelling SSMC frequency scans to retrieve the  $K$  factor.  $K$  is a function of  $R$  and hence indirectly related to dark

conductance. This is due to the fact that with an increase in conductance, the electric field strength in the cavity drops. A proposed alternative method is the absolute sensitivity ( $K R_0$ ) of a cavity, given in equation 3.7 [48].

$$\frac{\Delta R_0}{\Delta G} = -K R_0 \quad (3.7)$$

Previous work [48] has shown that that equation 3.6 introduces some problems, an increasing  $K$  factor can represent a decrease in either  $R_0$ , or an increase in the measured signal  $\Delta R_0$  (or it's equivalents in  $P$ 's). Due to its fractional properties,  $K$  does not contain all properties of the response. The claim that this alternative representation shown in equation 3.7 is defensible, stems from the fact that in the ideal under-coupled scenario, where  $R_0$  approaches unity,  $K R_0$  in equation 3.7 converges to  $K$  equation 3.6.

Historical, these values of  $K$  obtained were obtained in a discrete experimental manner. Later on, by the TU Delft a (simplified) model was used to obtain the  $K$  factor, in 2017 other groups computed the  $K$  factor numerically using a computational method [48]. However, since now computational methods exist to study exactly the effect of a conductance on the power reflection in a (seemingly) continuous manner, one can deduce the  $K$  factor for various dark conductances by writing equation 3.6 in differential form.

$$\left. \frac{dR}{dG} \right|_{R_0} \frac{1}{R_0} = -K \quad (3.8)$$

Here,  $\frac{dR}{dG}$  is obtained by simulating steady state conductances of the sample and their corresponding resonant depths and taking the derivative. This derivative should be evaluated at power reflection coefficient at the resonance frequency. This method allows for the non-linear characteristics of the measured signal. These characteristics arise due to a possible decrease of the initial power reflection  $R_0$ , that may exist due to a high dark conductance. Hence, this  $K$  factor obtained numerically, is a function of dark conductance, which is obtained experimentally via a SSMC measurement. The  $K$  factors above, and other cavity related parameters, will be obtained by simulating the full geometry of the resonance cavity while varying the conductance of the sample computationally while simultaneously computing the corresponding power reflection coefficient.

For signals with  $R_0$  approach zero,  $R_0^{-1}$  approaches infinity and can dominate the absolute sensitivity of the cavity  $\frac{dR}{dG}$ . Following equation 3.7, the absolute sensitivity again will be defined as in equation 3.9.

$$\left. \frac{dR}{dG} \right|_{R_0} = -K R_0 \quad (3.9)$$

Hence, the absolute sensitivity is defined as the change in power reflection, due to an small change in conductance, at an specific initial dark conductance.

In literature, usually not the change in conductance is reported, but the product of the yield and sum of the mobilities ( $\sum \mu = \mu_e + \mu_h$ ). Reasoning behind this is that the geometric thickness of the film drops out, allowing easy comparison between samples. Furthermore, it also incorporates the mobility. The yield of a semiconductor is given in equation 3.10 [51].

$$\phi = \frac{L(\delta n + \delta p)}{F_A I_0} \quad (3.10)$$

Here,  $F_A$  is the fraction of absorbed light and  $I_0$  the number of incident photons. If one now rewrites equation 2.3, assuming equal number of free electrons and holes generated and using equation 3.2, one arrives at equation 3.11:

$$\sum \mu = \frac{\Delta \sigma}{e(\delta n + \delta p)} = \frac{\Delta G}{e(\delta n + \delta p)} \frac{b}{aL} \quad (3.11)$$

Now, finally using equation 3.11 and equation 3.10 one arrives at the following result.

$$\phi \sum \mu = \frac{\Delta G}{e F_A I_0} \frac{b}{a} \quad (3.12)$$

This result above is often presented in literature [29]. This property incorporates the yield, directly relating to excitation efficiency, and mobility, usually an indirect indicator for photovoltaic cell efficiency [40].

# 4

## Modelling

Discretization has historically been used in various fields of study such as computer science, mathematics, physics and engineering. It involves the transformation of continuous models, functions, or data sets into discrete data sets, which allows it to be handled computationally. One of the numerical techniques that rely on discretization is the FEM. It is widely used to solve complex physical problems where no analytical solutions are available. Analytic problems are usually obtained by solving partial differential equations and their respective boundary equations. However, as geometries become more complex, it is usually impossible to find an analytic solution to the partial differential equations governing the system. This method involves dividing the simulation domain into small interconnected subregions, called finite elements. Individually all finite elements should adhere to the laws of physics such as continuity equations or other partial differential equations describing the local element. For a solution to be smooth and physically accurate, it is necessary that the solution of each finite element is consistent at the vertex shared with its neighboring finite element. Each finite element can hence be described as a set of equations, dependent on the governing equations and the location and distance of the other finite elements in the global system. All the systems of equations of each finite element is recombined in a global system matrix, which is solved for to approximate the global solution.

In this chapter, the geometry of the cavity cell will be described in more detail and highlight some of the effects on the cavity. Furthermore different components used by the FEM will be described and the underlying electrodynamics. Since the commercial software COMSOL [38] has been used to arrive at results, not much focus will be put on the underlying mathematics of the FEM itself. However, all the components used in COMSOL to arrive at the final results will be discussed. All simulations have been conducted using COMSOL 5.6 multiphysics, using the RF (radiofrequency) module. More specific information on the simulation itself can be found in chapter 5.

### 4.1. Meshing

The subdivision of the simulation domain into smaller volume elements is called meshing. These individual smaller elements will next be used to solve a set partial differential equations, with its boundary conditions described by its neighbouring elements, while the element itself must adhere to its own governing equations of the simulation. Each individual mesh element will also have to adhere to individual conservation laws [32], dependent on the study applied. Although the meshing is relatively automatized in the software environment of COMSOL, some proper evaluation is required. In general, a course mesh will yield inaccurate results, while an more refined mesh will yield more accurate results at the cost of computational power used. An example of a fine mesh used in found in figure 4.1

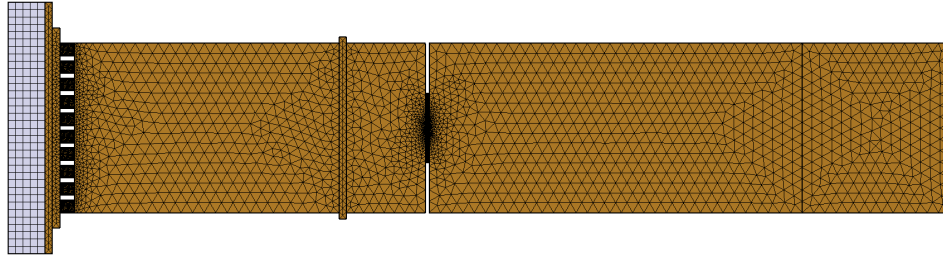


**Figure 4.1:** An overview of an mesh used. Clearly visible is that the meshing is dynamic, increasing in density when the dimensions of the geometries in the model decreases.

#### 4.1.1. Number of elements

For any wave-like electromagnetics model, the mesh must have a meshing dependent on the wavelength of the excitation source used. The minimum is the defined by the Nyquist frequency, having at least 2 elements per wavelength resolved. However, this is usually orders of magnitudes too course to solve any geometric problems. COMSOL by default creates a mesh of 5 second order tetrahedrons per wavelength in a dielectric medium, which for more complex problems still much too course. Since in this model steady state problems are studied, with a relatively low change in excitation frequency, the mesh has been kept constant in between simulated frequencies. [20]

#### 4.1.2. Element order shape

When subdividing a geometry in discrete elements, the shape, size and spatial distribution of the elements are of importance. When using a first order element, linear (first order polynomial) shapes are the only possibilities for a vertex. For second order elements, the vertices are able to be curved according to a second order polynomial. Higher order shapes correspond with a higher order polynomial curves. First order elements are usually less computational costly, however having the drawback that near circular shapes the number of elements increases significantly. Usually second order elements give a good representation of the geometry, while keeping computational requirements at an acceptable level. Higher order polynomial are usually not used, except in some rare use cases. In this model, second order elements are used. [15]

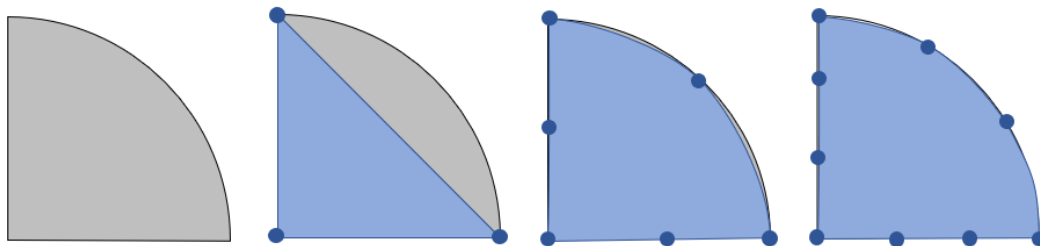


**Figure 4.2:** The effect of the element shape order based on the geometry simulated, simplified in 2D. From left to right: (1) The to be discretized geometry. (2) A first order element approximating the shape, introducing significant artifacts. (3) A second order element allowing the vertices of the triangle to bend, making a good approximation of the geometry. (4) A third order element, approximating the circular shape almost perfectly. Taken from [15].

### 4.1.3. Element order solution

For 3D electrodynamics simulations it is usually not sufficient to simulate using first order tetrahedrons [15]. Not only first order tetrahedrons approximate the geometry poorly, but also the solution within each finite element is poor. First order elements are only able to have the solution  $y = ax + c$  (For 1D problems) inside its domain. This would require the electric field to be only linearly distributed across each FE. This is not sufficient, for example if one wants to evaluate the magnetic field corresponding with this system, according to equation 2.18, the magnetic field will be continuous across each element, with discrete jumps in amplitude between each element. Second order polynomials however, allow quadratic solutions in the form of  $y = ax^2 + bx + c$ . This allows smooth magnetic fields [34] to be derived from the electric field. Finally, the most obvious reason for choosing a second order element, is that the electric field in a resonant cavity is not linear across a volume, and a quadratic solution (or a general higher order) for each element is a better approximation. The shape of a quadratic second order tetrahedron is shown in figure 4.3. Higher order tetrahedra (or in general: higher order other shapes) give better solutions. However the computational requirements are usually not worth the increase in accuracy.

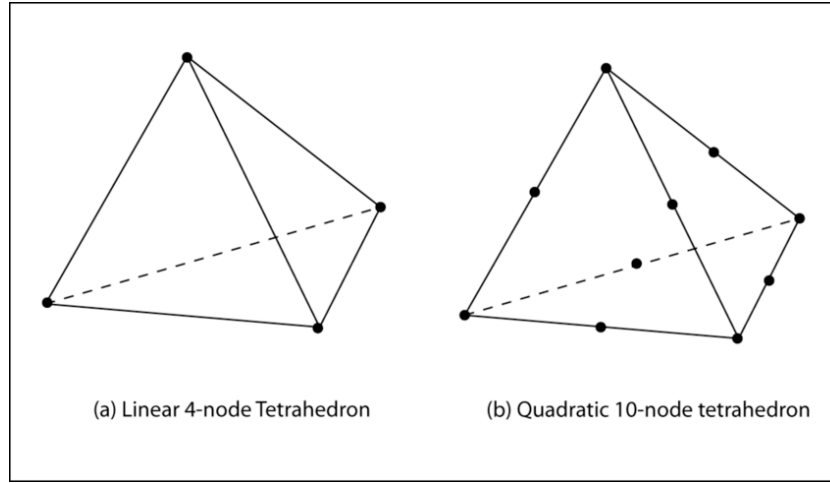


**Figure 4.3:** First and second order elements used in a FEM analysis. Taken from [4].

### 4.1.4. Meshing quality

The main value COMSOL uses for meshing quality is the distribution of the skewness of the elements. A finite element is considered as highly skewed if the angles between the vertices of the element are different from ideal element types. The definition for equiangular skew is given in equation 4.1.

$$\text{skewness} = 1 - \max \left( \frac{\theta - \theta_e}{180 - \theta_e}, \frac{\theta_e - \theta}{\theta_e} \right) \quad (4.1)$$

Here,  $\theta$  is the angle over a vertex (2D) or edge (3D) for an ideal element and  $\theta_e$  is the ideal angle of the corresponding vertex or edge. For tetrahedron  $\theta_e = 60^\circ$ . The equiangular skew is evaluated for all edges of a face, and the minimum value is taken of all these faces of a single element. A high quality mesh represents distribution of equilateral skew defined in equation 4.1 as close to 1 as possible. Evaluating the equiangular skew is an important measure to check the overall quality of the mesh, which is a factor for correctness of the solution [22] [14]. The histograms of the models used in this thesis are given in figure 4.4.

## 4.2. Solver

There are generally 2 types of solvers used in FEM to solve the obtained sets of linear equations; a direct solver that obtains the 'exact' solution in a single step, and an indirect solver that makes an initial guess and uses iterative methods, such as variants to the gradient descent to approximate a new solution. In general, direct solvers are more memory intensive, while indirect solvers are less memory intensive, but requiring more computation time.

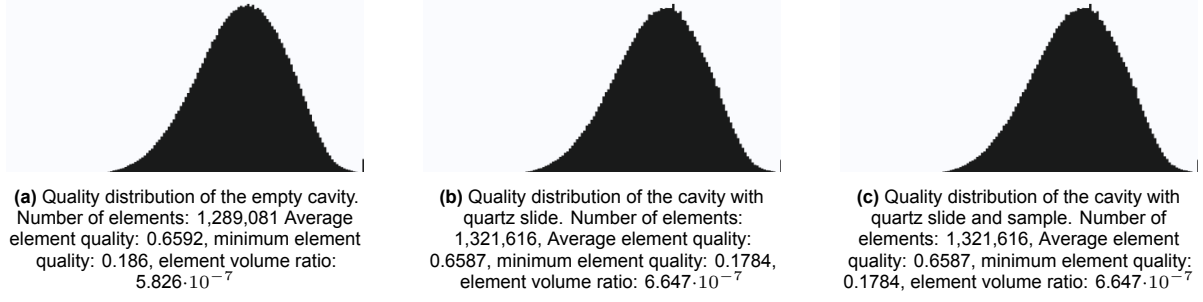


**Figure 4.4:** Distribution of the skewness of the finite elements used in 3 models.

#### 4.2.1. Direct solver

The main usage for using direct solvers in electromagnetic FEM systems is to find the eigenfrequencies of a system. This is rewriting the system of linear equations to be written in a system of eigenfrequencies and eigenmodes. Some of these eigenfrequencies correspond to a real resonant frequency. Direct solvers take all the linear equations of a system into account, and solve these directly in one (big) step. The direct solver used in this thesis is the 'PARallel DIrect SOLver' (PARDISO). This solver is a thread safe software library that allows solving large sparse systems generally using a lower upper decomposition to solve big systems of linear equations. In conjuncture with the usage of cluster computing, PARDISO is a good method to obtain solutions for these large systems [54]. A main drawback of this solver is that the memory requirements for big systems can still exceed the available memory, forcing PARDISO to work out-of-core, dumping the memory to the storage, while simultaneously decreasing computation speed by orders of magnitude. Having PARDISO work out-of-core should be avoided.

#### 4.2.2. Iterative solver

Iterative solvers are used mainly in arbitrary frequency solutions. This hence means that it is not a requirement that eigenfrequencies must be calculated, and hence this types of solvers can be used to study quality factors. These require a range of frequencies around the resonant frequency. Furthermore, the memory requirements of these types of solvers are usually significantly less than the direct solvers, allowing larger meshes. In this thesis, the iterative solver first starts with some proposed initial solution, before using the Generalized Minimum RESidual (GMRES) method. This method uses the initial (guessed) solution to calculate a new solutions, that is (should be) closer to the actual solution. During each iteration the GMRES tries to improve it's previous solution by proposing a better approximation of the solution. Finally, if the proposed solutions seem to converge between each iteration and the change between proposed solutions seems to approach a beforehand set tolerance value, the algorithm is considered converged and the last value of the GMRES algorithm is taken as the solution. A drawback of the GMRES method is that the solutions to all previous iterations must be stored. Hence, if the solution does not converge fast enough, the system can run out of memory. [5]

### 4.3. Geometry

A combination of measurements and blueprints of the cavity cell have been used to establish the dimensions of the cavity cell. The used dimensions can be found in appendix A. The dimensions shown are only the inner dimensions of the cavity cell since this is the only part where the electric field is of interest. Solving for the volume in the walls of the cavity is not possible (and not interesting). Furthermore the penetration depth of the microwaves is so small it would introduce an unreasonable amount of finite elements and the system would become computationally unsolvable. It must be noted that the indentation to hold the sample has been decreased by 0.1 mm to remove the sliver of air between the simulation domain and the sample. Small slivers do not only increase computation costs significantly due to big amount of extra small finite elements used, but also decrease the accuracy of the FEM. [37]

### 4.3.1. Iris modelling

The circular hole defining the boundary between the resonating parts in the geometry and the non-resonating parts is an important aspect of the model. Despite the iris being spatially separated from the sample itself, the iris is an defining component of the resonant cavity. Ignoring the more trivial elements such as conductive walls and a general shape, the iris can be considered the most important part of the resonant cavity. The first reason is that the losses per surface area induced in this cavity are highest in the region around the iris. However, the losses in this area are noisy without some proper modelling. For example figure 4.5 can be consulted as an example with improper modelling. Here, the losses manifest as noise and are highly dependent on the meshing used. A slight change of the geometry somewhere, even in unimportant areas, will result in a different constructed mesh, and will result in different (noisy) losses in the iris. Since losses define the quality factor of the cavity, it is important to have consistent losses. Hence, in the model it has been chosen to fillet away the sharp boundaries of the iris. This will usually remove singularities present in the model, which can present as (locally) unreasonable results. Not only this, but fillets also increase accuracy of a simulation, especially in areas that have sharp corners [3]. Although adding fillets increases the number of finite elements present in the system significantly, it also forces the meshing to consistently create small finite elements in the region around the iris, reducing noisy losses in general, and generating a smooth lossy area. A representation of the effects of fillets can be found in figure 4.6, showing consistent, smooth losses in the iris.

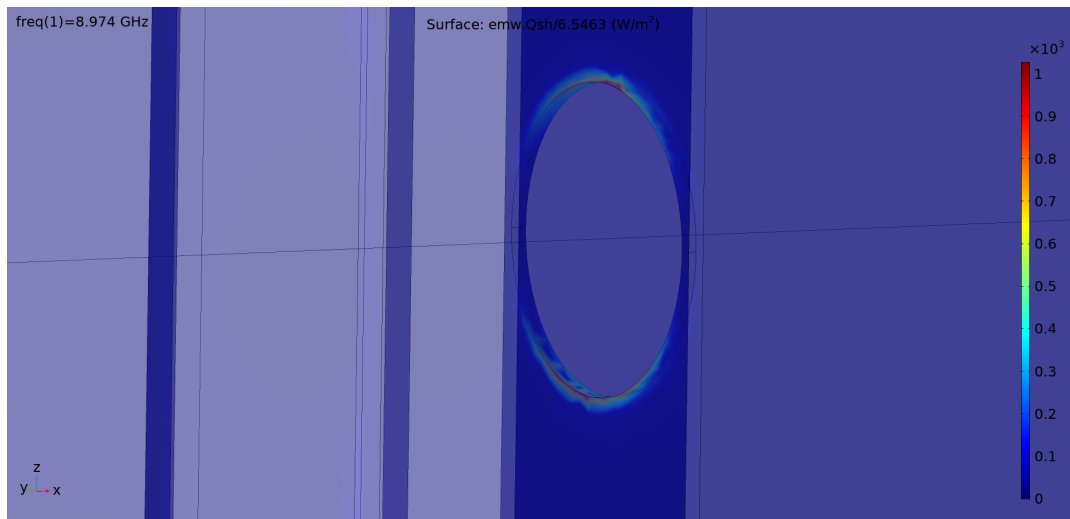


**Figure 4.5:** The losses of the iris in close up with a lower quality mesh. The blue hue is caused by the transparent (blue) walls of the simulation domain. The losses near the iris are noisy, and are inconsistent when the mesh is varied.

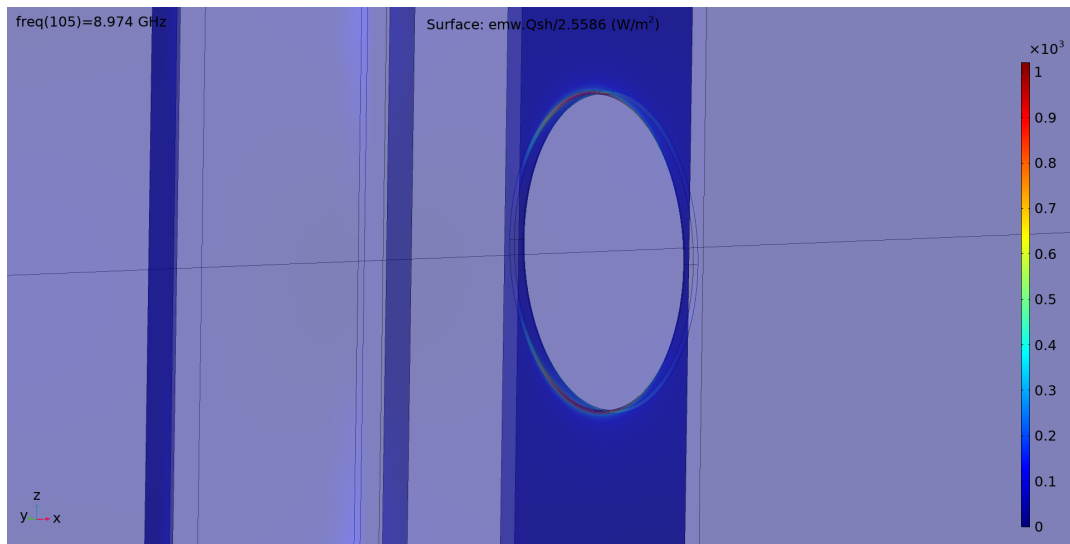


**Figure 4.6:** The losses of the iris in close up. The blue hue is caused by the transparent (blue) walls of the simulation domain. Notice how on the top and bottom of the iris a region is present with the highest (localized) region of Ohmic losses in the full geometry. The losses however, are smooth and seemingly continuous.

#### 4.3.2. Grating modelling

The grating is a subregion of the cavity cell that allows laser light to reach the sample. The grating is one of the places with the most details in the simulation domain. Small cylindrical shapes are present in this region, forcing the finite elements to reduce in size, increasing the total amount of finite elements. This will increase computational complexity significantly, even though some areas of the grating are less dominant in the characteristics of the cavity. It has been chosen to remove the small surface elements using the '*remove details*' feature in COMSOL. Since circular elements, such as the cylindrical elements present in the grating, are approximated by regular polygons, the *remove details* feature will effectively decrease the amount of these regular polygons approximating a circle. This will allow the meshing to be more coarse and consist of less elements, being less computationally expensive. There is still importance to properly model the grating, since (with exception of the iris) the current density at the inner parts of the grating is highest, directly inducing losses. This is the result of the fact that all the current gets concentrated on all of these, individual, parallel elements. The losses are attributed by the oscillating electric field existing in the cavity, which is accompanied by currents resonating along the boundaries. Since these currents are unable to exist in air due to its low conductivity, and currents (or better, charge) must be conserved, the currents are highly located in the grating. The normalized current density of the grating is shown in figure 4.7.

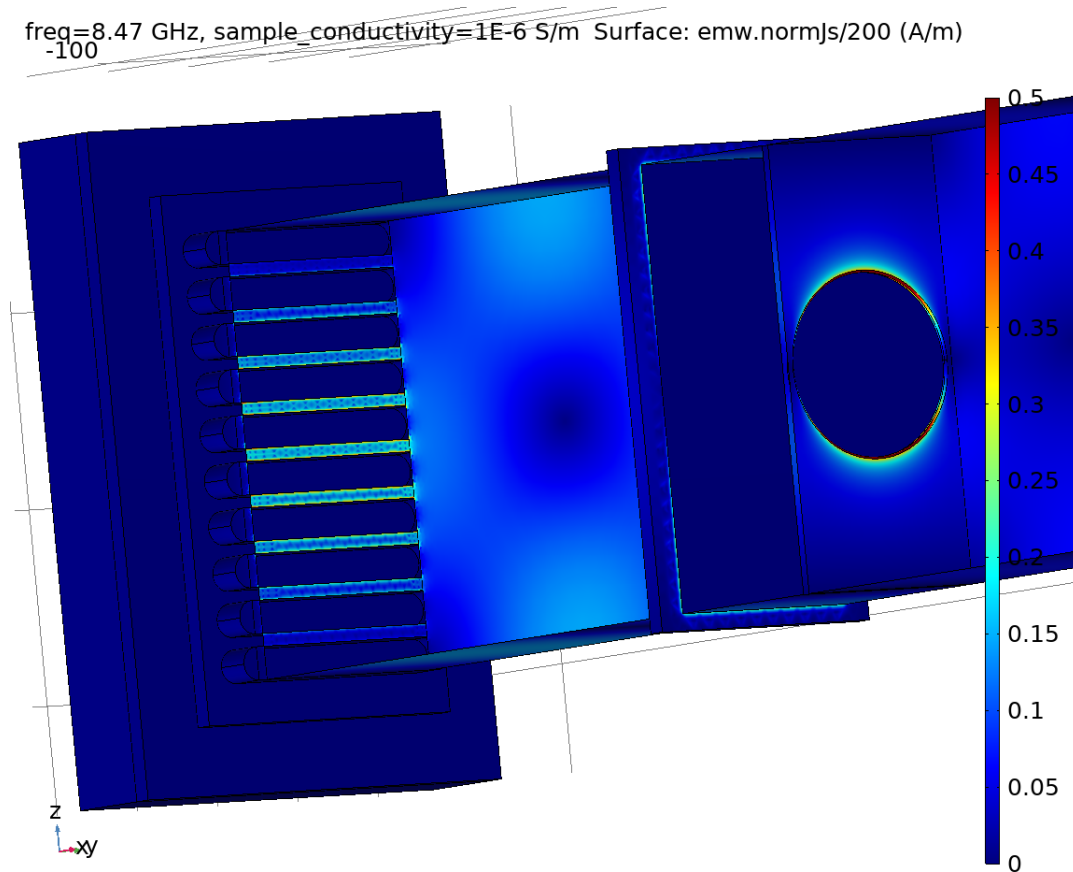


**Figure 4.7:** The normalized current density of the cavity cell. Notice how the current gets concentrated along the grating of the cavity.

Since the power loss in the cavity scale with current, the fraction of conducting material to air should be ideally as high as possible. However, due to the requirement that a sample should be illuminated with a light source, the grating should have some trade-off between open space to allow for illumination and highly conductive material.

#### 4.3.3. Perfectly matched layers

The boundaries of the simulation domain are marked by the following boundaries:

- The walls of the cavity cell/waveguide, reflecting all power keeping it inside the domain.
- The power port in the waveguide used to excite and measure the electromagnetic power. This surface freely allows the transfer of energy.
- The frontal quartz window mounted on top of the grating transmitting (albeit minimal) electromagnetic power to the environment. This environment outside of the cavity absorbs most of the electromagnetic radiation, having little secondary effect on the field in the cavity itself.

Since modelling the full environment outside the cavity cell is unfeasible, the domain must be truncated. However, the electromagnetic radiation should still be allowed to transmit, although not absorb, to the region outside of the domain. To model this behaviour, an absorbing layer instead right outside the frontal quartz window is placed. This fictitious absorbing layer has been (computationally) 'perfectly matched' in a sense that it absorbs electromagnetic radiation by varying its (purely computational) dielectric properties, while keeping induced reflections due to the discrete variation in dielectric properties to a minimum, simulating a generalized outside environment. [21]

## 4.4. Electrodynamics node

Within electrodynamics various disciplinary domains exist e.g., electrostatics, magnetostatics and quasistatic. Each line of work, uses different governing equations, assumptions and boundary conditions [66]. Although COMSOL has many modules with the governing equations stored, one does still need to select the correct general study based on its underlying physical foundations. Furthermore, specific material properties must be assigned in the model, while simultaneously postulating governing equations to each material. These assigned properties with the governing equations in each subdomain constitutes the overall behaviour of the electromagnetic wavelike characteristics in the system. This system is subdivided by so called domains. Since the simulation domain is constructed by adding many different geometric shapes, where each geometric shape added constitutes a domain. Furthermore, all these domains can be either sliced or conjoined to either increase a domain size, or decrease a domain size. In particular, for each domain 4 additional parameters may be specified:

1. The material properties withing the volume of the domain.
2. The material properties at the boundaries of the domain.
3. The governing equation within the volume of the domain. These are usually the partial differential equations being solved for.
4. The governing equation at the boundaries of the domain. These are usually the boundary conditions of the partial differential equation being solved for.

Furthermore if one wants to use the RF frequency domain modelling of COMSOL used in this thesis, some extra preconditions on the system as a whole apply. These are outlined below.

1. The ray approximation does not hold [14].
2. The electromagnetic fields within the simulation domain will change sinusoidally in time at the chosen resonant frequencies [23].
3. The wavelength of the exciting electromagnetic wave must be comparable to the dimensions of the simulation domain [23].
4. All material properties are constant with respect to field strength [23].

In this thesis, the above mentioned requirements are assumed to be true. A further consequence of item 4 is that the characteristics in the model will scale well when the excitation power changes, allowing the model to be evaluated at a different power when its characteristics are scaled with a (not specifically linear) constant.

In this subchapter, the characteristics described by the governing equations withing each domain, and its corresponding boundaries, are discussed. Each domain is constituted by a so called *node*, a way of describing a namespace; a declarative region that provides a scope to identifiers (material properties, governing equations, boundary conditions, initial conditions, functions, variables etc.) to conveniently organize the software environment in a single overview and allow easy use. [59]

### 4.4.1. Wave equation - Electric

The wave equation - Electric node is used to describe the propagation of the electromagnetic characteristics of the ambient air and nitrogen in the cavity cell and the waveguide inlet. The relative permittivity is considered to be unity, and no discrepancy is made between ambient air and nitrogen in terms of permittivity. The governing equation is given in equation 4.2 and is derived in section 2.2.1.

$$\nabla \times \mu_r^{-1} (\nabla \times \vec{E}) - k_0^2 (\epsilon_r - \frac{j\sigma}{\omega\epsilon_0}) \vec{E} = \vec{0} \quad (4.2)$$

Here,  $\mu_r$  is the relative permeability,  $\vec{E}$  is the electric field,  $k_0$  the wavenumber in vacuum,  $\epsilon_r$  the relative permittivity of the medium,  $\sigma$  the conductivity of the medium,  $\omega$  the angular frequency and  $\epsilon_0$  the permittivity of vacuum. The wavenumber in vacuum ( $k_0$ ) is given in equation 2.27.

Since  $\frac{\sigma}{\omega\epsilon_0} \ll 1$  holds in air and nitrogen, the imaginary component is approximately zero when traversing free space. In the model, this factor is approximated by zero in free space, hence considered a lossless material.

#### 4.4.2. Wave equation - Lossy dielectric

The quartz substrate used is an (albeit lowly) lossy material, and hence introduces some power losses. These have been modeled using the free space node, as described above, while introducing an lossy factor in the calculation of the displacement field. The electric loss tangent is described in equation 4.3. Here,  $\delta_e$  is the electric loss tangent,  $\epsilon'$  the real component of the relative permittivity and  $\epsilon''$  the imaginary component of the relative permittivity.

$$\tan \delta_e = \frac{\epsilon''}{\epsilon'} \quad (4.3)$$

Hence the complex relative permittivity is given in equation 4.4

$$\epsilon_r = \epsilon'_r(1 - j \tan(\delta_e)) \quad (4.4)$$

Although it might sound obvious that this (or other representations of the) loss factor should be taken into account, one does need to explicitly specify this in COMSOL. Later in this thesis, this loss tangent (indirectly the imaginary component of the relative permittivity) is used in the calibration of the depth of the power reflection curve, since these properties of the quartz slide are not exactly known.

Hence, the governing equation is given in equation 4.5. This exact equation follows equation 4.2, with a alternative representation for the permittivity.

$$\nabla \times \mu_r^{-1}(\nabla \times \vec{E}) - k_0^2 \epsilon_r \vec{E} = \vec{0} \quad (4.5)$$

Furthermore, due to the insertion of a medium with a higher permittivity than the nitrogen in the cavity, the standing wave pattern is perturbed. This is due to the increase of the real component of the permittivity.

#### 4.4.3. Impedance boundary condition

An incident electromagnetic plane wave on a bulk matter with a finite conductivity will result in an damping of the electric field, where the electric field will only penetrate a small amount in the material, known as the skin effect. Furthermore the electric field will induce surface currents in this area inducing the reflected electric field [66]. In this thesis, the impedance boundary condition is used with the properties of gold, since the penetration depth is so small that only the gold coating is of interest. Simulating the electric field in the gold walls is impossible due to the extremely small skin depth (see figure 2.6). All current is considered localised at exactly the boundary of the simulation domain. Hence, we treat the gold plated walls as a boundary condition. This boundary condition allows the mathematical usage of conductivity resulting in a small loss of energy due to the finite conductivity of the material, allowing losses induced by the current and finite conductivity, while not simulating the electromagnetic field explicitly. The governing equation at these boundaries is given in equation 4.6.

$$\sqrt{\frac{\mu_0 \mu_r}{\epsilon_0 \epsilon_r - j \frac{\sigma}{\omega}}} \vec{n} \times \vec{H} + \vec{E} - (\vec{n} \cdot \vec{E}) \vec{n} = (\vec{n} \cdot \vec{E}_s) \vec{n} - \vec{E}_s \quad (4.6)$$

Here,  $\vec{E}$  and  $\vec{H}$  are the corresponding electric field and magnetic field, the material properties specified in this equation are the (simulated) gold layer,  $\vec{n}$  is the normal of the surface and lastly,  $\vec{E}_s$  is the electric field generated by an external source, considered  $\vec{0}$  in this model. This equation has not been derived but has been used in literature before [48] [14].

#### 4.4.4. Transition boundary condition

A transition boundary condition is used to approximate the sample. Although usually in finite element methods geometries are explicitly modelled, this is not feasible in this case for thin film samples due to their thickness being in the 200-600 nm range [19], while dimensions of the cavity are in the order of centimeters. Since the properties of the sample have an influence on the electric field of the cavity, but having dimensions that are too small to explicitly model with finite elements, a boundary condition is applied. This boundary condition is placed on the boundaries of the connecting finite elements at the samples location. The boundary condition in the model representing the sample can induce a discrete jump in the tangential electric field amplitude. This discrete jump will be accompanied by a induced current on both sides of the sample, losing some electromagnetic power across the mathematically

thin layer. The mathematical description for the transition boundary condition is given in equations 4.7 - 4.11.

$$\vec{J}_{s,1} = \frac{Z_S \vec{E}_{t,1} - Z_T \vec{E}_{t,2}}{Z_S^2 - Z_T^2} \quad (4.7)$$

$$\vec{J}_{s,2} = \frac{Z_S \vec{E}_{t,2} - Z_T \vec{E}_{t,1}}{Z_S^2 - Z_T^2} \quad (4.8)$$

$$Z_S = \frac{-j\omega\mu}{k} \frac{1}{\tan(kd)} \quad (4.9)$$

$$Z_T = \frac{-j\omega\mu}{k} \frac{1}{\sin(kd)} \quad (4.10)$$

$$k = \omega \sqrt{\epsilon + \left(\frac{\sigma}{j\omega}\right)\mu} \quad (4.11)$$

Here,  $\vec{E}_{t,n}$  the tangential electric field on side  $n$ ,  $\vec{J}_{s,n}$  the induced surface currents densities on side  $n$ ,  $d$  the thickness and  $\mu, \sigma, \epsilon$  the usual dielectric material properties. Usually the transition boundary condition is used for propagating waves and not in resonant cavities. The effect is that the described equations are unexpected, the current seems to be different on both sides of the sample, and a discrete jump in tangential electric field strength is present [14]. In the case of a traveling wave (hence not reflected due to the transition boundary condition) some power will be lost due to the transition boundary condition. This will result in a discrete drop between electric field strength across the boundary. Consequently, this discrete drop has a different induced surface current on the other side of the boundary condition. However in this model, a resonant cavity is applied. This has the effect that the electromagnetic waves are incident from both sides, evening out the discrete jump in current and electric field strength. These above equations have not been derived in this thesis, but this boundary condition has already been implemented in literature for similar models [13].

The transition boundary condition is comparative to the impedance boundary condition due to the fact that it is placed specifically on a surface. The main differences lie in the fact that a transition boundary allows transmission and can be used in the middle of a simulation domain, while the impedance boundary condition can only be used on domain edges and does not explicitly allow transmission.

#### 4.4.5. Port excitation

In computational simulations no 'real' electromagnetic waves are created, however one does still need to specify a source for traveling waves and some mathematical description of the wave characteristics. In this model, the port excites the waveguide with a TE<sub>10</sub> waveform as described in chapter 2.4. This port allows the calculations of  $S_{11}$  parameters, better known in transmission theory as the scattering parameters. Usually, the  $S_{11}$  parameter is defined as a complex value between 0 and 1, where the real component relates to the amplitude of the electric field and the imaginary component to the phase shift due to propagation distance and reflection(s). Since the Schottky barrier diode measures power and not scattering parameters, the  $S_{11}$  parameter must be converted to a power reflection coefficient. In this thesis, the power reflection coefficient is evaluated as in equation 4.12.

$$R = \frac{P_r}{P_i} = |S_{11}|^2 \sim \frac{|\vec{E}_r|^2}{|\vec{E}_i|^2} \quad (4.12)$$

Here,  $\vec{E}_i$  is the incidence electric field and  $\vec{E}_r$  the reflected electric field. The power reflection coefficient is equal to  $R$  in the SSMC measurements and is a fractional value. In the FEM, no actual measurement devices exist, hence the total electric field is evaluated at the 2D boundary by applying equation 4.13. This equation uses the knowledge of the applied electric field applied to calculate the scattering parameters.

$$S_{11} = \frac{\int_{\partial\Omega} (\vec{E} - \vec{E}_1) \cdot \vec{E}_1}{\int_{\partial\Omega} \vec{E}_1 \cdot \vec{E}_1} \quad (4.13)$$

Here, to calculate the  $S_{11}$ , the computationally known applied electric field ( $\vec{E}_1$ ) across the full rectangular waveguide 2D boundary is compared to the total electric field ( $\vec{E}$ ), effectively including  $\vec{E}_1$ , over the full boundary (port).

## 4.5. Calibration

Material properties are often not exactly equal to values given in the literature. Furthermore these values in the literature are often not exactly determined for the specific frequency used in this model. To allow for (small) changes in properties of the cavity cell and quartz slide, a calibration method has been implemented to calibrate the simulation results with actual measured results. This calibration has been split in 2 stages. A calibration of the simulation results using an empty cavity and a calibration with a quartz slide placed at maximum electric field strength with no transition boundary applied. Especially for the quartz slide the calibration is of use since the exact dielectric properties in the gigahertz range are not consistently reported in literature. The goal is not to artifice the results, but to carefully obtain parameters, and evaluate if these are reasonable compared to known literature values. Furthermore, some less relevant properties are unknown and will not be determined, such as for example surface roughness.

### 4.5.1. Empty cavity cell

Firstly the cavity is calibrated in an empty state, hence without quartz, samples or other perturbations present. The only two possible free relevant material variables are the dimensions and the conductivity of the interior gold plated walls. Although the quartz window slide also has unknown (exact) dielectric parameters, this quartz window slide has been chosen as a non-relevant property and variations have not been studied. Most of the dimensions have been measured. When impossible to accurately measure them, either approximations or the values used during the initial in-house design process conducted in 2012 are used. All used geometric values are shown in appendix A. During the modelling process, these geometric parameters were not further varied since the resonance frequency already matched the experimental values well.

Lastly, to change the power reflection coefficient, the conductivity of the gold interior walls can be changed. A lower conductivity represents more induced losses, and hence a decrease in the power reflection. Increasing the conductivity has the opposite effect. In this specific case, since the walls are only gold plated and some wear is present due to usage, a small decrease in (also computational) conductivity is sensible. This change in conductivity has no effect on the resonance frequency itself. These results can be found in chapter 6.1.1

### 4.5.2. Quartz slide

Secondly, the cavity has been calibrated with a quartz slide inserted in the correct position. This quartz slide has different dielectric properties than the surrounding nitrogen and hence perturbs the resonant pattern. Firstly, this shifts resonance frequency to a lower value due to the (partial) increase of permittivity. This is due to the wave impedance of this material being lower, decreasing the wavelength in this material [66]. Hence, a lower overall excitation frequency is required to construct a standing waveform. This quartz slide changes the distribution of the electric field, now being asymmetric in the direction perpendicular to the axis of its nodes and anti-nodes.

Secondly, the quartz slide is a lossy dielectric. Some of the electromagnetic power will be lost due to the imaginary component of the permittivity. Since the quartz substrate is placed at the maximum of the electric field, this value has non-negligible effect on the power reflection coefficient. Lastly, this value has not been reported in literature for the frequencies used. Furthermore, this lossy parameter is specific to the production process used. To calibrate the model with the experimentally used quartz slides, matching the experimental and numerical results while still being critical on the values obtained. The results of this calibration are shown in chapter 6.1.2.

# 5

## Simulation details

This chapter will describe in more detail the procedure used to arrive at the simulation results in chapter 6. It is mainly concerned with the computational steps, and simulation details of the results. The software environment used is COMSOL Multiphysics®, specifically 'The Electromagnetics module: RF Module, Frequency Domain Interface', and 'The Electromagnetics module: RF Module, Eigenfrequency Interface' [14]. The Eigenfrequency Interface allows resonant frequencies to be found and simulated without knowing beforehand what the resonant frequency are, while the Frequency Domain Interface allows simulating the response to a range of frequencies. Both can be used using the same geometry and features described in chapter 4, but not always in a single study. Running both studies in a single run will sometimes result in error messages, inadvertently changing settings, resulting in unworkable studies.

### 5.1. Simulation approach

To run the simulation with appropriate meshing, a fine mesh is required. However, for running tests, obtaining starting parameters, or a general response of the system, a courser mesh is preferred. This courser mesh allows all functionalities of COMSOL, while obtaining some less accurate results. However, final results require a high quality meshing, making some calculations non-trivial. A slightly elaborate method is required to run a simulation with the high quality meshing. Although COMSOL includes an eigenvalue solver, nevertheless, solving eigenvalues is more memory intensive than simulating a predefined frequency. Since the required memory for solving the eigenfrequencies exceeds the available memory for the high quality mesh, a manual method is conducted to find the eigenfrequencies.

1. Use the eigenvalue solver in the course mesh and write down the (desired) eigenfrequency found. This mesh is however, not sufficient enough for accurate results. These eigenfrequencies found will give a close indication of what the eigenfrequencies of the fine mesh will be.
2. Use the frequency domain study and select the high quality mesh. This mesh is optimized to give (more) accurate results. Put in a desired frequency range around the frequency found in step (1) and run the study. Next, calculate the power reflection coefficient.
3. If the minimum of the power reflection coefficient is captured in step (2), manually interpolate the data to approximate the power reflection coefficient. Now, choose a finer frequency range around this frequency and run the simulation again, iterate until the 'exact' eigenfrequency is found. It should be stated a single manual interpolation is often not close enough to the resonant frequency. If the minimum of the power reflection is not captured in step (2), increase the frequency range and repeat step (2).
4. The final found frequency can now be used when varying a samples conductivity to obtain the power reflection coefficient.

Changing the geometry or the real component of permittivity somewhere in the model, will shift the resonant frequency, requiring a new search for the resonant frequency. It is important to capture the exact resonant frequency, otherwise the analysis for obtaining the  $K$  factor will be inaccurate. Especially

for samples with a high dark conductance, an offset from the resonant frequency can yield unreliable results.

## 5.2. Simulation details

Four different sets of final simulations have been conducted. Usually varying either the complexity of the model, and sweeping across specific parameters. All of the final results have been studied using the Frequency Domain Interface, only using the Eigenfrequency Interface as a tool during the design process. All four of the different simulations are described below.

1. The empty resonant cavity swept across the frequencies surrounding the resonant frequency. This allows the general characteristics to be probed. This allows also the shape of the resonant peak to be simulated, allowing calculation of the quality factor. Only simulating the resonant frequency is not sufficient to check the reliability of the simulation.
2. The cavity with the quartz slide inserted swept around various frequencies surrounding the resonant frequency. Again, this allows the quality factor to be calculated. Furthermore, in chapter 6.1.2 of the results it will be clear that not all quartz slides have equal dielectric properties. Hence, this simulation is used to (arguably arbitrarily) select a quartz slide to approximate computationally. This has been achieved by slightly varying the computational dielectric properties, until the simulated data and experimental data are comparative. No rigorous analysis has been conducted to fit a specific quartz slide to the numerical results. This would allow only this specific quartz slide to be used and would only add marginal extra value. This process would take approximately one to two days computationally.
3. The cavity with the quartz slide inserted and the appropriate boundary condition applied have been simulated, describing the characteristics of an arbitrary thin film sample. Again, this has been swept across the resonant frequency to establish the characteristic behaviour. The thin film thickness has been selected as 250 nm. This film thickness is not only used in the calculations inside of COMSOL for determining the loss properties along this boundary condition, but also later in the analysis of the results.
4. The cavity with the quartz slide inserted and the appropriate boundary condition applied has been simulated, just as in the above simulation. However, only the resonant frequency is manually selected. Furthermore, more conductances than simulation (3) have been selected to study the effect of higher conductances in an appropriate manner. Ideally, this simulation should be conducted for a range of frequencies around the resonant frequencies such as the simulations described previously. However, the computation times would exceed levels that can be considered reasonable.

Each type of simulation has different computational requirements. The most important ones are listed in table 5.1.

**Table 5.1:** Computational requirements and the effects on the computation used for each configuration studied.

	empty cavity - freq sweep	quartz slide - freq sweep	sample and slide - freq sweep	sample and slide - conductance sweep
RAM requirements	36 GB	46 GB	46 GB	46 GB
simulation time	11:59:20	9:17:28	29:48:03	5:36:38
relative tolerance	0.001	0.001	0.001	0.0001
degrees of freedom	8,508,481	8,709,175	8,709,175	8,709,175

Here, the geometric effect of inserting the quartz slide inside the cavity is quite clear. Adding the geometry increases the degrees of freedom being solved for due to the mesh requiring a smaller size now across the quartz slide. The mesh used for the quartz slide/sample is equal, yielding similar memory requirements.

## 5.3. Hardware and software details

Due to the memory requirements of these simulations exceeding the available memory on most consumer grade laptops, all these simulations have been run on a High Performance Computing (HPC) cluster managed by the Linux systems department at the Shared Service Center ICT of the TU Delft [17]. This cluster allows computations to be run remotely on a centralized system. This allows an increase of computation power used and an increase in available memory. This cluster uses a system to determine how many resources are allocated to a job send to the queue manager. The queue manager (TORQUE) is a Parallel Batch System (PBS) implementation. An example PBS script sent to the queue manager can be found in appendix B.

It must be noted that further speeding up the simulation is likely still possible on the HPC cluster. For most of these simulations, usually only 1 node is used with 12 cores. Attempts were made to improve this. However, the internal job scheduler of COMSOL and internal settings seems to conflict with the TORQUE scheduler, yielding unexpected behaviour. Some examples of unexpected behaviour were node loads >10 times above what should be considered possible, running out of memory where similar configurations do not, or a general non-improvement of simulation speed. For some of the simulation files, more specific changes to settings have been made (not described in this thesis), but these achieved improvements are only marginal and can be disregarded. The default settings generated by COMSOL, combined with the job script provided in appendix B, are safe to use. The main utilization of the cluster is from the increase of available memory, which has been achieved.

Remote computing requires remote storage, hence some form of secure copy protocol (SCP) clients must be implemented, since simulation files need to be transferred to a remote directory in accordance to be run remotely on the HPC cluster. Furthermore, simulation files can be quite big, especially if previous iterations of models are stored as well. To access the remote directory of the cluster, WinSCP v.5.21.7 is used [47]. WinSCP is freeware, supporting various methods of secured file transfer. Furthermore, it includes a convenient Graphical User Interface (GUI) that allows all basic tasks, such as opening .txt files and transferring data with relative ease.

Further software used is PuTTY v0.78.0.0 [57]. This is a free implementation of the Secure Shell Protocol (SSH). SSH facilitates secure communication between a local user's computer and remote servers. SSH achieves this by providing a secure channel to which one can log in, execute applications, shell access in the Unix environment and more. SSH allows to load in specific packages, such as specific COMSOL versions and run them. PuTTY can be run in conjunction with WinSCP, allowing to setup a SSH channel with relative easy use to the same remote HPC cluster where the remote directory is located. Furthermore PuTTY allows submissions of job scripts to the TORQUE queue system as well, through the established SSH channel.

In conjunction with WinSCP and PuTTY, Xming v6.9.0.31 [26] is used as well. Xming is an X Window System for Microsoft allowing to establish a GUI on remote systems. To use Xming, first an SSH session is configured, in the GUI of WinSCP, using PuTTY. Next, one can run an application in the SSH session. The Xming server running in the background of the local machine will be able to display the GUI output of the remotely executed program. This allows user friendly changes to the model in the GUI of COMSOL, without having to download the files from the remote directory to the local computer first, before being able to make possible changes in the locally generated GUI. Since essentially the GUI is run remote, but controlled locally, some latency is present in the GUI. However, due to the size of the files generated by COMSOL and download/upload speed usually being limited, it is recommended to use any type of X Window System. Hence Xming in this scenario can be compared to a remote desktop connection, however only specifically for GUI of the programs running on the remote HPC cluster.

The setup has been done according to the HPC wiki of the TU Delft [17]. Different operating systems might require a different setup than described above, but the HPC wiki covers the most common operating systems.

Further software used is IGOR Pro v9.00 [30] and IGOR Pro v6.03, directly outputting the data out of the SSMC/TRMC setup and doing some preliminary analysis. However, all the main data analysis and visualization in this thesis is conducted in Python v3.10 [61], using the packages NumPy v1.24.0

[25] and SciPy v1.9.3 [63] for the data analysis and Matplotlib v3.6.2 [28] for the visualization. All corresponding code used in this thesis can be found in a public github repository at [https://github.com/JS-Koning/thesis\\_data](https://github.com/JS-Koning/thesis_data).

## Results and Discussion

In this chapter the results of the simulation and experimental work will be presented. First SSMC will be discussed, starting with an empty cavity, followed by a cavity with a quartz slide inserted at approximately  $3/4$  the length of the cavity. Both of these results will be compared to experimentally obtained results.

Next, TRMC will be discussed. Here, the previous model will be altered, adding a transition boundary condition to the quartz slide. This will allow the conductance to be varied, studying the response of the cavity which allows the determination of the  $K$  factor. Furthermore, the absolute sensitivity of the cavity will be determined.

Lastly, the effect of the electric field strength will be studied experimentally using two different CsMAFA perovskite thin film samples. Their absorption spectra are found in appendix F and the scanning electron microscopy measurements in appendix G. From these figures it is clear that the absorption spectra are comparative, but the average grain size is approximately doubled between samples. Although this is no guarantee for equal characteristics, this does allow two distinct average grain sizes to be studied, one on presenting an average grain size of 100 nm and one presenting an average grain size of 200 nm. Previous literature has suggested that grain size can be a factor in measuring mobilities using TRMC. This is induced by surface grains and the limited mobility of charge carriers crossing grain boundaries [49]. Hence, indirectly the electric field strength could play a role in determining the mobilities since a higher electric field strength increases the average distance travelled for each charge carrier. This should lead to different effects in samples with different average grain sizes, i.e. with a different extension of the grain boundaries surface area. Considering a sample with a small average grain size, charge carriers that (on average) get accelerated by a stronger electric field (higher microwave power) should come across grain boundaries more often than in the case of bigger average grain size. Therefore, the effect of varying microwave power should lead to more evident changes in the resulting TRMC measurements for samples with smaller grains than larger grains.

### 6.1. Steady state microwave conductivity

#### 6.1.1. Empty cavity cell

The measured power reflection coefficient of the empty cell will be compared to the simulation of the empty cavity cell. The results of this are shown in figure 6.1. The experimental empty cavity has a quality factor of  $Q = 304$ , while the simulated cavity has a higher quality factor of  $Q = 325$ . Both of these quality factors have been obtained from approximation in equation 2.33. Some differences between the simulation and the results are present. Some of these differences can be attributed to the following reasons.

- The frequency shift is likely attributed due to simulated geometrical inaccuracies. Even though the samples indentation size has been varied by 0.1mm, this is likely not the main reason behind this frequency shift.
- The bandwidth of the resonant curve possibly deviates due some non-simulated loss properties. Furthermore, the real world cavity used might have some contamination in its interior, introducing extra losses.

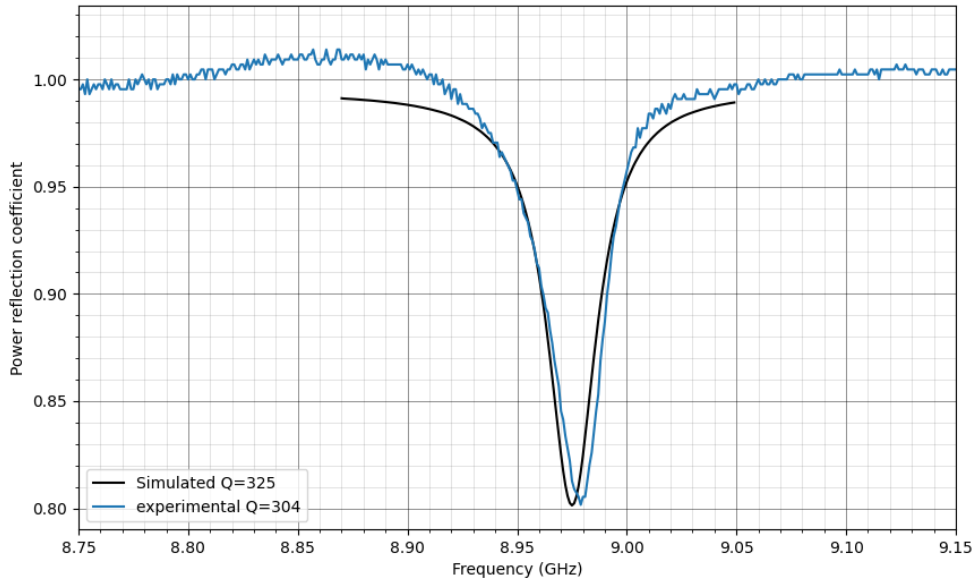


**Figure 6.1:** The experimental SSMC measurement of an empty cavity shown in blue, combined with the numerical results obtained for the model without the quartz slide.

An observation here as well is that the power reflection coefficient seems to increase above 1 slightly when the cavity is connected. This effect hence likely attributed due to an other component in the experimental setup than the cavity itself.

The conductivity of the walls of the cavity simulated is  $4.0 \cdot 10^7$  S/m. This is slightly lower than the literature value of  $4.11 \cdot 10^7$  S/m [27].

### 6.1.2. Quartz slide

The simulation results and the measured power reflection coefficient of various quartz slides are shown in figure 6.2, along with the obtained quality factors using the method in equation 2.33. Various seemingly identical quartz slides are present in the experimental setup. However, the quartz slides seem to have differences in dielectric properties upon measurement. Some of the quartz slides measured are recycled in-house, these have been used in an unknown amount of previous sample depositions. Furthermore these quartz slides have been used in an unknown amount of different, unknown characterization techniques. Before measurements, these slides were cleaned using the method described in appendix C. Furthermore, 5 pristine slides have been measured in an attempt to establish a baseline.

From figure 6.2 it is clear that all quartz slides behave significantly different. Moreover, it is not possible to distinguish the pristine slides from the recycled slides using SSMC. Additionally, the effect of cleaning the pristine quartz slides according to the method described as in appendix C has been studied. No further effect was found when the SSMC signal of the directly out of the factory packaging was compared to the same slides after two cycles of cleaning.

It has been chosen to simulate the higher  $Q$  factor quartz slides (closer to the 8.5 GHz frequency) and ignore the lower performing quartz slides. Simulating all possible variations in dielectric properties of the quartz slides is non-trivial, and hence has not been done. The dielectric properties used in the simulation, along with some reference values are found in table 6.1.

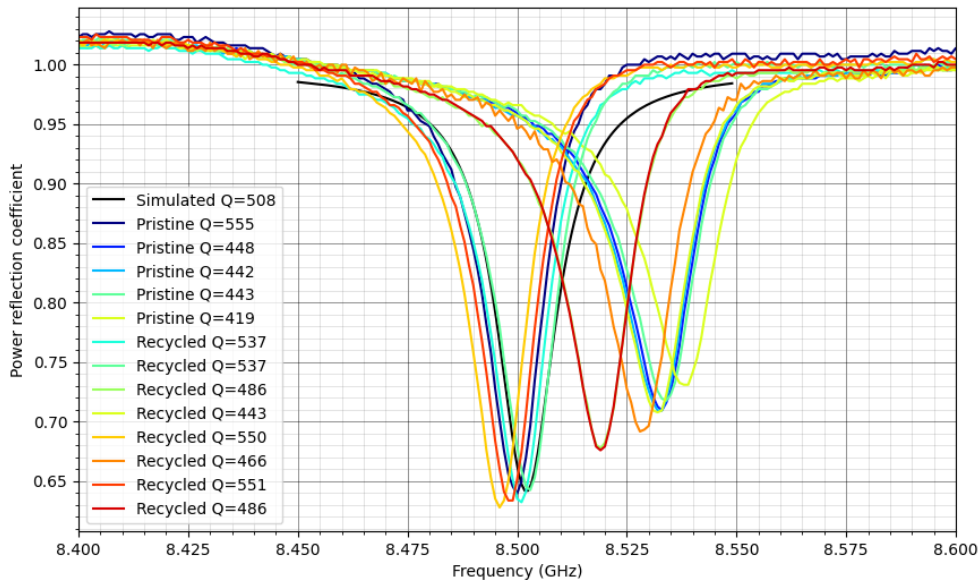


**Figure 6.2:** Simulated curve shown in black versus the measurements of the pristine and recycled quartz slides.

**Table 6.1:** Approximate dielectric properties of the supplier of the quartz substrates.

	Nikon NIFS Series*[60]	Tosoh ES-ED-H Series [58]	Simulated values $\sim 8.5$ GHz
Relative permittivity ( $\epsilon_r$ )	3.7 (up to 1 MHz)	3.9 (at 500 MHz)	4.0
Loss tangent ( $\delta_e$ )	$1.0 \cdot 10^{-4}$ (at 1 MHz)	$< 10^{-3}$ (at 500 MHz)	$3.1 \cdot 10^{-4}$

\*used literature values

It is clear from figure 6.2 that the quartz slides do not have the same dielectric properties. Since a higher Q factor indirectly prescribes a stronger electric field, some quartz slides perform better than others. Additionally, it is evident that a trend exists, albeit the underlying physical reason behind this trend remains unclear. The change in dielectric properties can be attributed to the following reasons:

- The fabrication process of these quartz slides has possibly changed over time. Although this does not explain the differences between pristine slides, it can explain the differences between various recycled slides.
- The quartz substrates are not designed for dielectric measurements but for optical properties. Hence quality control is likely focused on optical properties spectra, not dielectric measurements.
- It is likely that different types of quartz substrates are present in the recycled boxes. Also, the pristine quartz substrates contain some variation after a closer visual inspection.
- The quartz slides might be damaged after many uses, particularly high energy characterization techniques or during deposition of thin film samples, resulting in inhomogeneous dielectric properties, having an adverse effect on the resonant pattern in the cavity.

## 6.2. Sample conductivity

In the simulation, the sample's conductivity has been varied using the transition boundary condition. For all simulated figures shown, the thickness of the sample has been chosen to be 250 nm. All results shown in the COMSOL environment will be displayed using conductivity. However, to allow calculations for different thicknesses, only conductances will be presented when data analysis is conducted out of the COMSOL environment. In all these results, a conductivity of  $10^{-6}$  S/m has been chosen as a reference value, since introducing a 0 S/m material induces computational problems. The power reflection coefficient as a function of frequency is shown in figure 6.3 for various conductances.

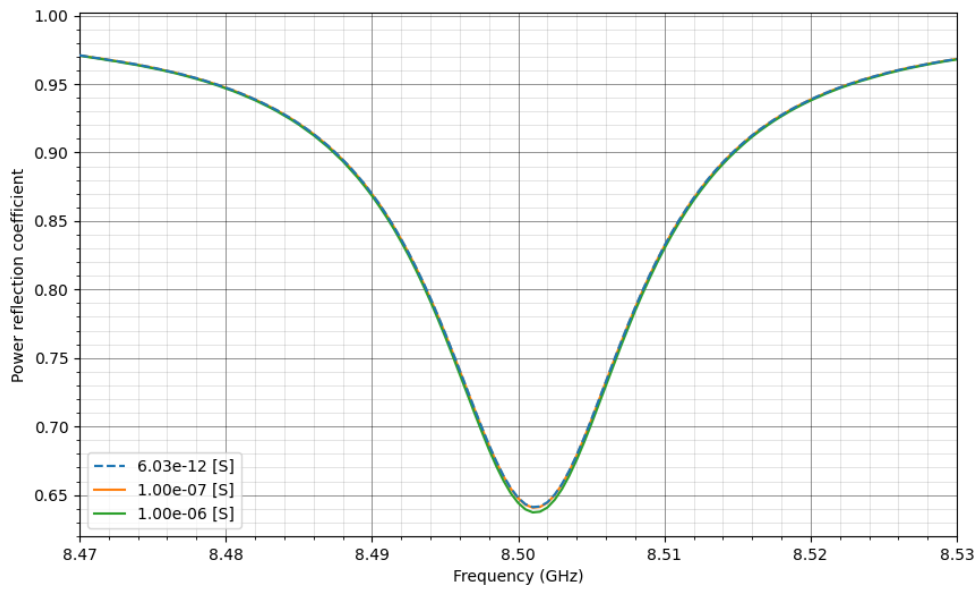


**Figure 6.3:** Simulation data of the power reflection coefficient with a varying conductance. The thickness of the sample is chosen to be 250 nm.

In figure 6.4 the resonance peak has been zoomed in. This shows that the approximation of  $10^{-6}$  S/m ( $= 6.03 \cdot 10^{-12}$  S) to be zero is valid, since increasing the conductance of the sample multiple orders of magnitude has barely an effect on  $R_0$ .

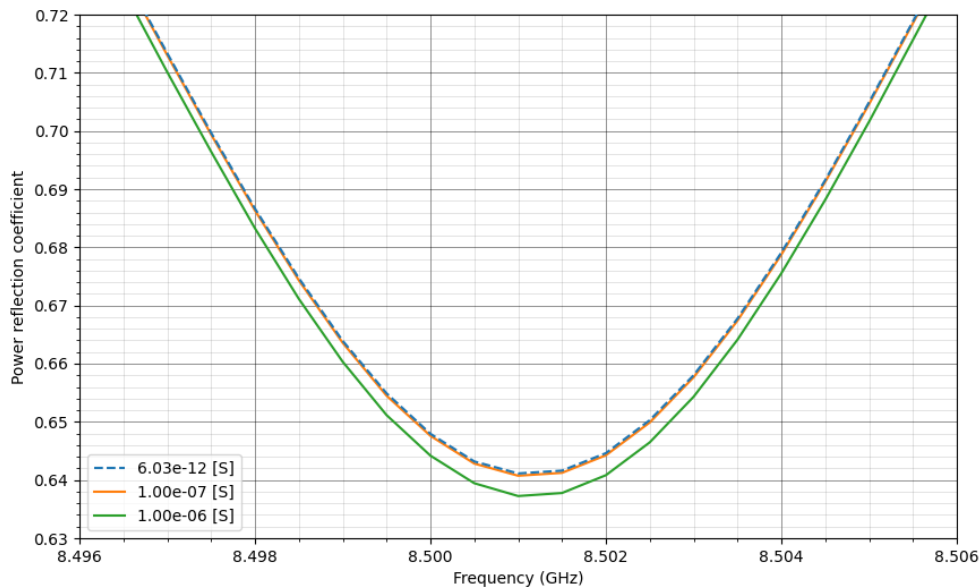


**Figure 6.4:** Zoomed data of the power reflection coefficient near the resonance frequency. The different curves represent different conductances of the sample. The thickness of the sample is chosen to be 250 nm.

Next, the minimum of the power reflection is found for a range of conductances. Only the exact resonance frequencies have been simulated to reduce computation time significantly.

In figure 6.5 the conductance versus  $R_0$  is shown. One can see that for low(er) sample conductances the response of the cavity is relatively stronger. A small change in conductance will vary  $R_0$  significantly. As conductance increases,  $R_0$  will approach zero.

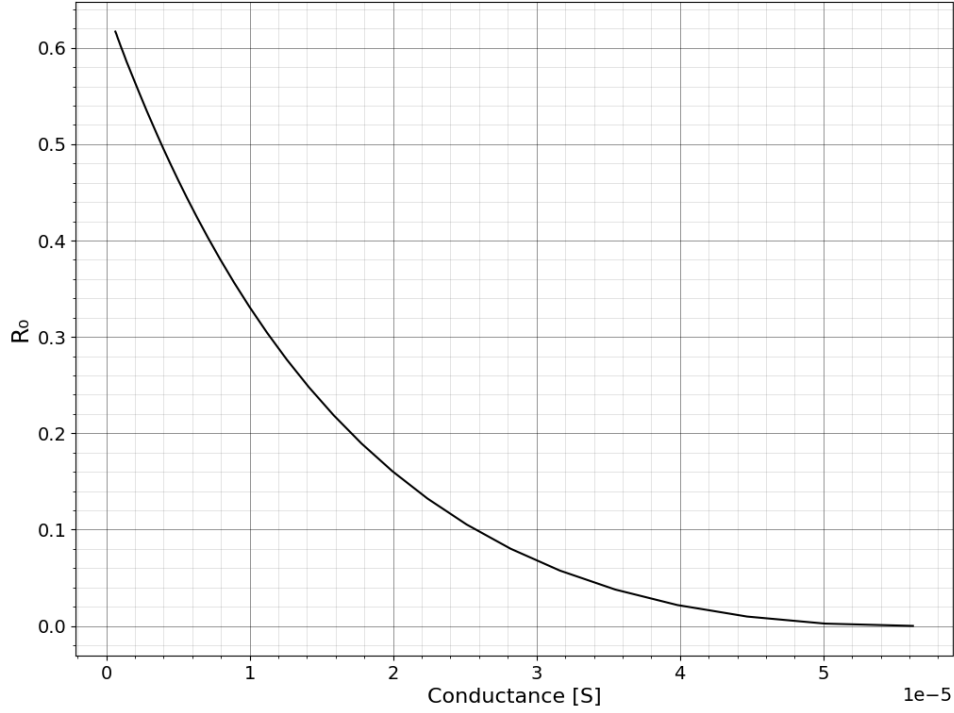
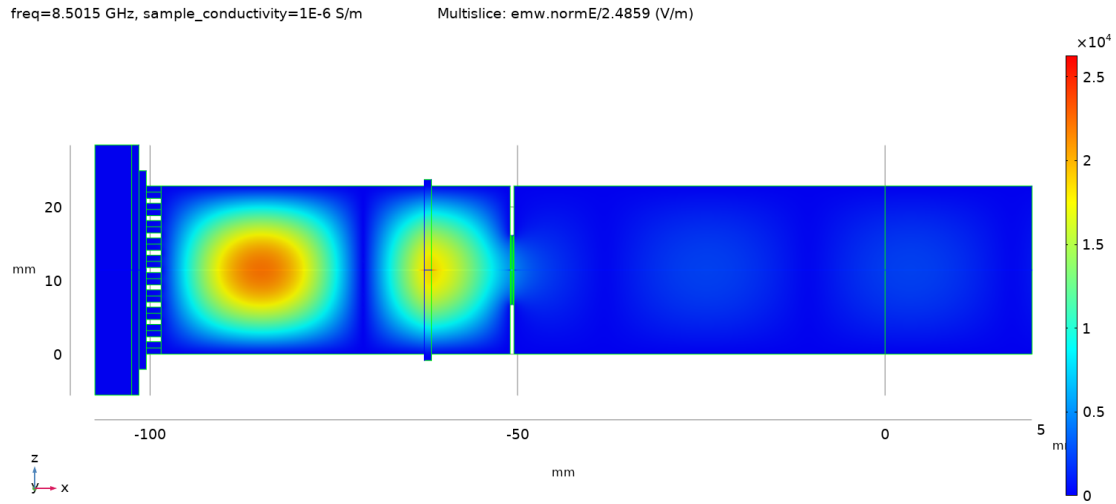


**Figure 6.5:** The minimum of the power reflection coefficient versus the conductance of the sample.

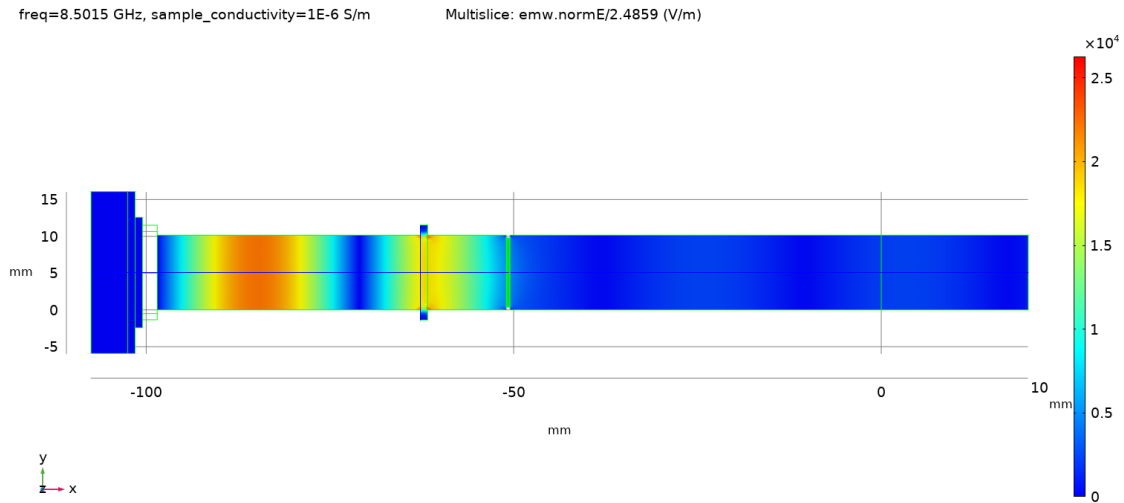
It has been chosen not to show a logarithm plot due to the unreliable results when very small values are included in the simulation.

### 6.2.1. Electric field distribution

In all figures the electric field strength is shown specifically for the instrumental setup used at the Delft University of Technology, at maximum power ( $P_i \approx 160$  mW). Furthermore, all the figures shown in this sub-chapter are for a sample conductance of approximately 0 S. The units of the figures are in V/m. The magnitude of the total electric field in the cavity is shown in figure 6.6 and 6.7.



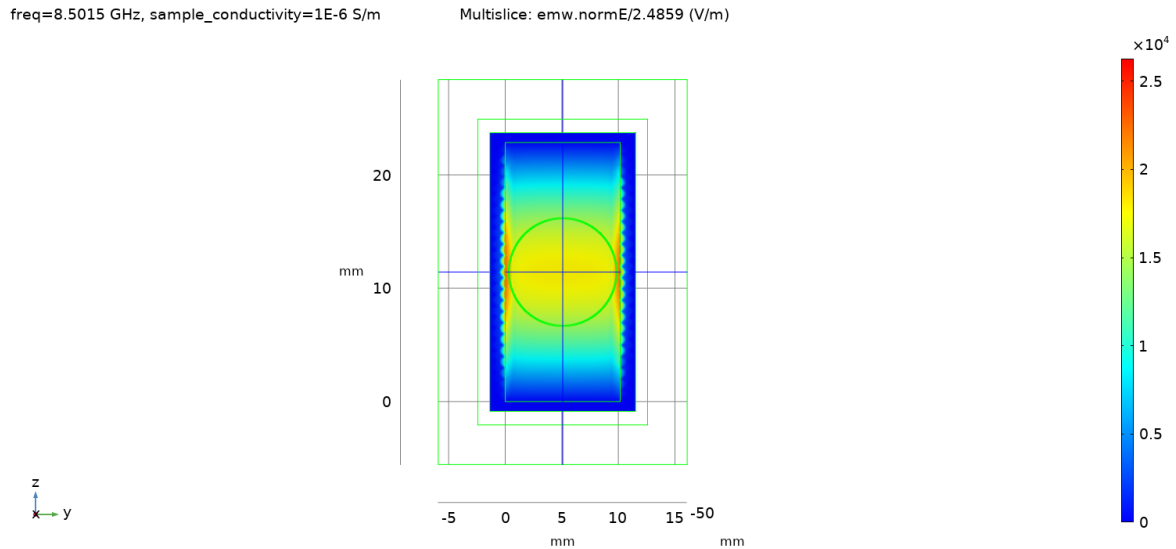
**Figure 6.6:** The amplitude of the electric field in the middle, along the length of the cavity cell. Note that the electric field is shown for the middle of the cavity. First side view.



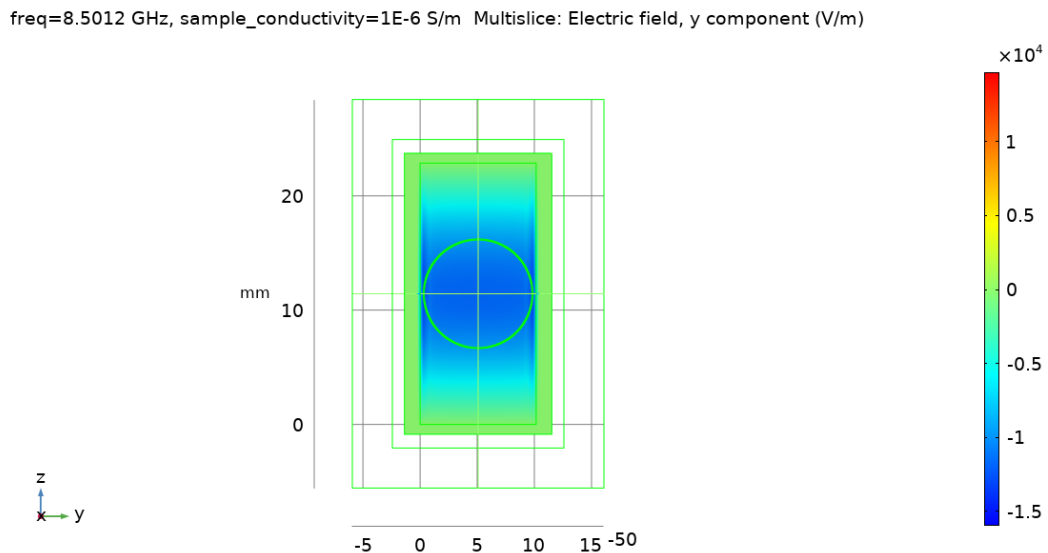
**Figure 6.7:** The amplitude of the electric field in the middle, along the length of the cavity cell. Note that the electric field is shown for the middle of the cavity. Second side view.

Figure 6.6 and 6.7 shows at a first glance that the electric field has a perturbation of the standing waveform. The anti-nodes are unevenly spaced as compared to an ideal cavity due to the higher permittivity of the quartz, changing the wavelength of the electric field.

In figure 6.8 the electric field at the location of the sample is shown. In figure 6.9 the amplitude of the electric field in the direction along the width (y-component) of the quartz slide is shown. More figures of the electric field distribution for various conductances of the sample can be found in appendix D.



**Figure 6.8:** The amplitude of the electric field strength at the location of the sample. Note that the electric field is nearly zero in the protruding edges.



**Figure 6.9:** The electric field strength at the location of the sample, in the y direction. The axis is shown in the bottom-left. Note that the electric field is nearly zero in the protruding edges

In figure 6.8, it is worth noting that along the edges, a strong sawtooth pattern is present with a relatively strong electric field. This is due to the electric field on the surface of the sample having a component in the direction of the normal vector of the sample. This electric field (direction) also has an effect on the power absorbed in the cavity, hence why it is highlighted in this section. In figure 6.9 the electric field in the y direction is shown. This field is tangential to the surface of the sample's surface. Clear from this image is that the electric field in this direction is more uniform, compared to figure 6.8. The non-uniform increase of the electric field in figure 6.8 near the edges of the quartz slide, along the z-axis, are physically relevant, and are not periodically dependent on the finite elements created, but created by reflections induced by the indentation of the sample holder. However, the triangular-like (sawtooth) pattern in figure 6.8 along the edges of the quartz slide are non-physical but an artifact introduced in the FEM. A close-up of this field can be found in figure 6.10 and a element quality analysis in figure 6.11.

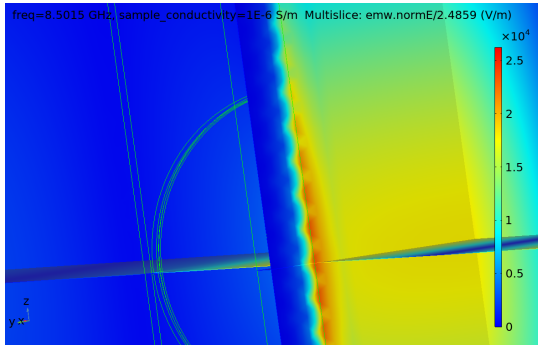


**Figure 6.10:** Absolute electric field at the edge of the surface of the sample. Zoomed in on the sawtooth pattern.

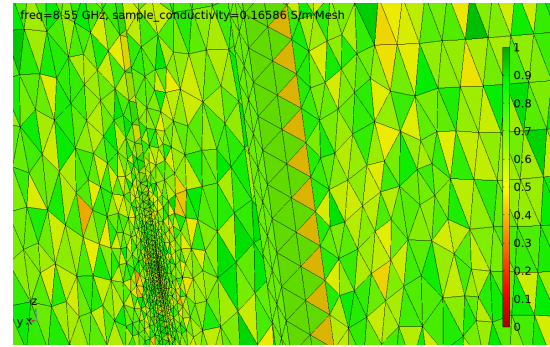


**Figure 6.11:** Mesh quality of the volume elements, at the same location as shown in figure 6.10. The sawtooth pattern corresponds to low quality elements.

Clear from these images is that the skewness of the finite elements is high in this region and the geometric location of these skewed finite elements align with the sawtooth pattern of the electric field. It can be concluded that this sawtooth like pattern is hence non-physical and a artifact of the FEM.

### 6.2.2. Electric field along the surface of the sample

The maximum value of the electric field along the middle of the surface of the sample has been evaluated. A representation of this line is shown in figure 6.12. Although the sides of the sample have a higher electric field strength, the middle of the length has a more uniform distribution and is might be preferred for analysis. Furthermore, the majority of the electric field along the line contains no artifact induced by the FEM, hence the evaluation. The maximum electric field versus the conductivity of the sample is shown in figure 6.13.

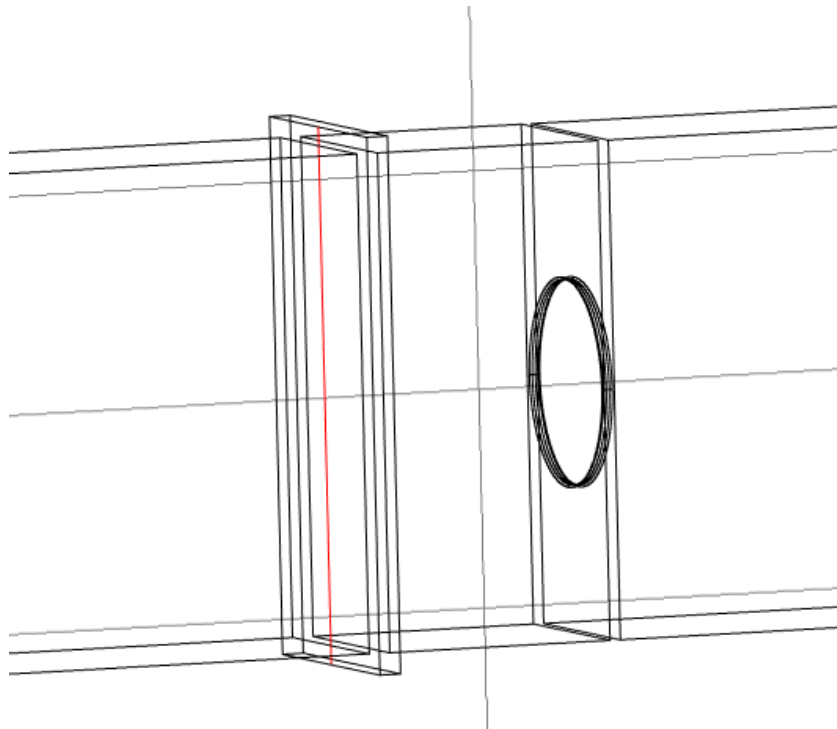


**Figure 6.12:** The red line represents the evaluated 1D line to find the maximum value of the electric field across the sample.

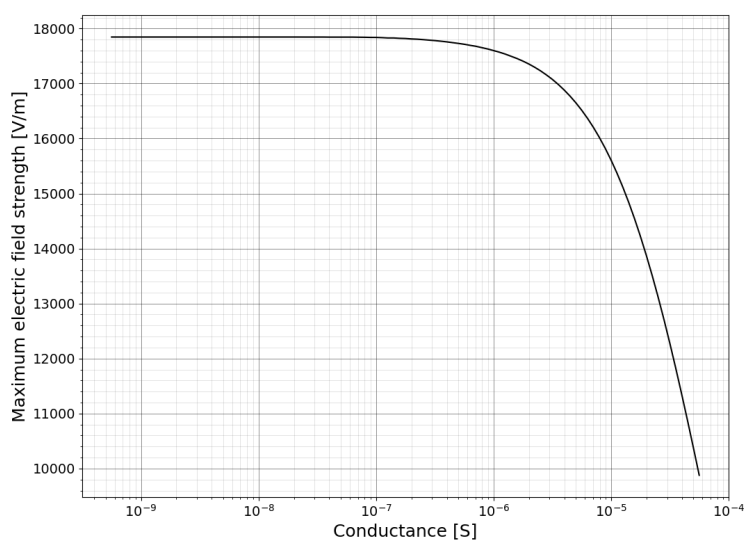


**Figure 6.13:** The maximum of the electric field along the line shown in figure 6.12.

Figure 6.13 indicates that the electric field strength is approximately 17,800 V/m and relatively indifferent for a conductance below  $10^{-6}$  S, but beyond this threshold, the electric field strength starts to decrease as the conductance of the sample increases.

### 6.3. Time resolved microwave conductivity

Properties related to the  $K$  factor in TRMC measurements will be given, all calculations are done according to chapter 3. In all these results, a conductivity of  $10^{-6}$  S/m has been chosen as a reference value since computationally simulating a value 0 S/m introduces computational problems.

#### 6.3.1. K factor - signal strength

Indirectly, the signal strength output by the TRMC electronics is denoted by  $\frac{\Delta R}{R_0}$ . The signal is hence a value between 0 and 1. First, the effect of the signal strength on the  $K$  factor is determined. This is illustrated in figure 6.14.

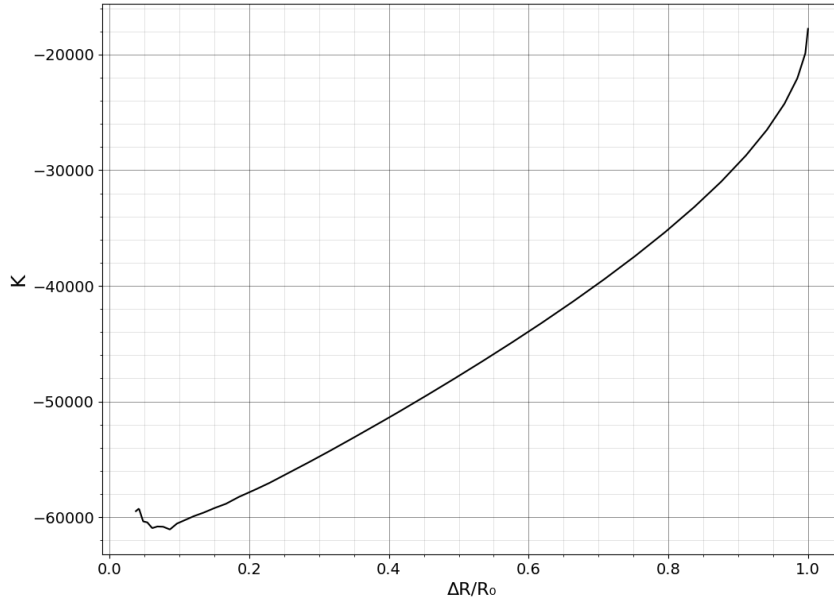


**Figure 6.14:** The obtained  $K$  factor for various signal strength outputted by the TRMC electronics. In this figure, at the initial state ( $R_0 \approx 0.64$ ) the dark conductance is 0 S.

The obtained  $K$  factor is varying dependent on signal strength. Furthermore, as the signal strength increases, the  $K$  factor seems to decrease. A decrease in  $K$  factor represents dividing the signal with a lower value leading to a higher photoconductance (see equation 3.5). Important background information is that actual signals (see equation 3.4) by the TRMC setup usually have a maximum measured value of  $10^{-2}$ . Hence, (ignoring the downward trend induced by artifacts and extrapolating the stable region) approximating the  $K$  factor as a constant at  $\frac{\Delta R}{R_0} \approx 0$  allows to approximate  $K \approx -63,000$ . A non-constant  $K$  factor should only be considered when (unusual) high signals are measured. Simulating the lower values of  $\frac{\Delta R}{R_0}$  than shown in figure 6.14 introduces computational artifacts, some of these have been omitted in this figure to increase readability. Some are still present to highlight where the model is less accurate. Note, that in section 6.3.2, this value for  $K$  is reevaluated.

#### 6.3.2. K factor - high dark conductance

If the sample has a high dark conductance,  $R_0$  will be a lower value (for reference values see figure 6.5). In this thesis, it will be assumed that a different value of  $R_0$  will not have any effect on the generation and recombination mechanisms. However, the response of the cavity to a induced photoconductance by the incoming laser pulse will be different. The  $K$  factor for high dark conductance will be determined by two different methods. The first method will be using the differential method of determining the  $K$  factor, closely analogous to the classical method of calculation, given in equation 3.8. The second method will be calculating the absolute sensitivity factor ( $dR/dG$ ), given in equation 3.9.

### $K$ factor

The determination of the  $K$  factor as a function of  $R_0$  is shown in figure 6.16. Here the noise in the higher  $R_0$  range is caused by numerical errors.

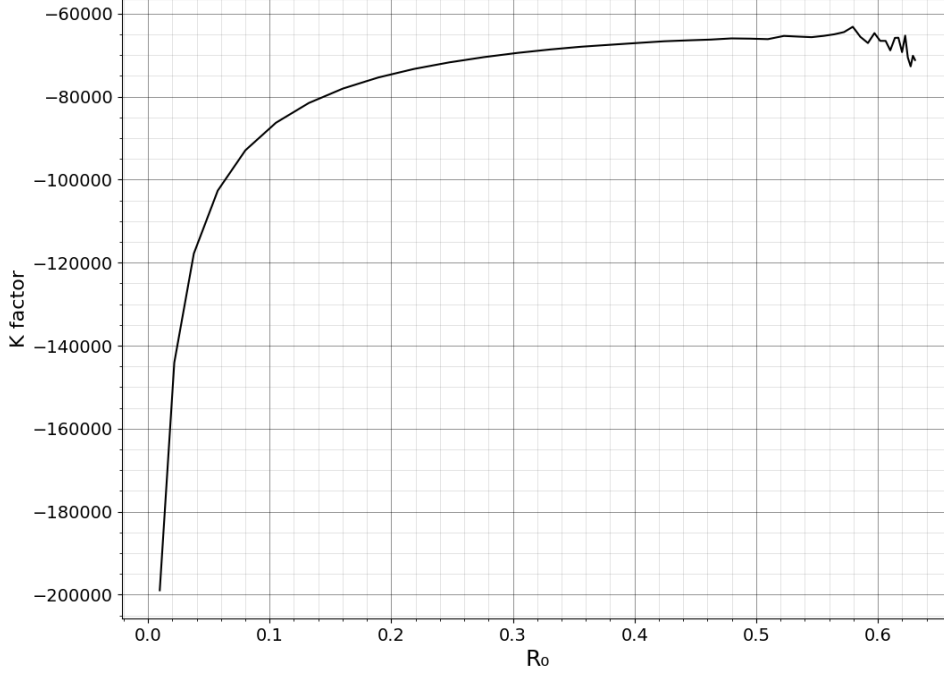


**Figure 6.15:** The  $K$  factor for various values of  $R_0$ , obtained computationally using equation 3.8. An extrapolated linear relation only including the stable region leads to  $dR/dG|_{0.64} \cdot R_0^{-1} \approx -64,000$ .

For lower values of  $R_0$  the  $K$  factor is decreasing. This can be attributed to 2 possible reasons.

1. The  $R_0^{-1}$  term is likely dominating for lower values of  $R_0$  when calculating the  $K$  factor.
2. The absolute sensitivity of the cavity,  $dR/dG$ , is either increasing, or decreasing at a slower pace than  $R_0^{-1}$

Furthermore, the results in figure 6.15 indicate that for a higher dark conductance, the signals are more responsive, i.e. if the dark conductance increases in a sample, and if the time dependent signals outputted during a TRMC measurement are the same for both (different) dark conductances, the actual photoconductance is lower in the sample with a higher dark conductance. If one ignores (re)combination mechanisms, the same principle holds for the product of the yield and mobility.

In literature [48] the computationally  $K$  factor determined for a comparative cavity cell is approximately  $K \approx 29,500$  at zero dark conductance. This is however for a induced change in conductance of  $\Delta G = 1.0 \cdot 10^{-7}$  S. In this thesis, these (low) values of  $G$  still introduce numerical errors, underestimating the  $K$  factor significantly. It is not certain if the comparison between literature and this model is appropriate.

### Absolute sensitivity

The absolute sensitivity can be denoted as  $KR_0$ , but a more intuitive notation is likely  $dR/dG$ . This absolute sensitivity as a function of  $R$  is given in figure 6.16. This shows that at zero dark conductance,  $dR/dG$  can be approximated as  $-42,000$ .

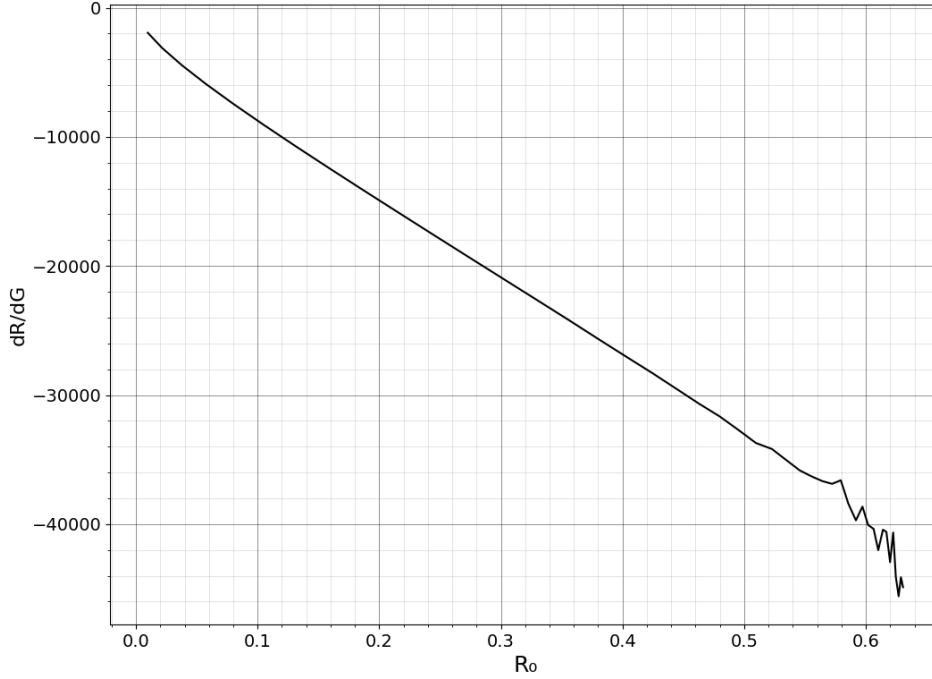


**Figure 6.16:** The absolute sensitivity of the cavity at various resonance depths, obtained computationally using equation 3.9. An extrapolated linear relation only including the stable region leads to  $dR/dG|_{0.64} \approx -42,000$ .

These results show an increasing absolute sensitivity for an increase in dark conductance. Following the same reasoning for the  $K$  factor, now treating the absolute sensitivity as the  $K$  factor, the results in figure 6.15 indicate that for a lower dark conductance, the signals are more responsive, i.e. if the dark conductance increases in a sample, and if the time dependent signals outputted during a TRMC measurement are the same for both (different) dark conductances, the actual photoconductance is higher in the sample with a higher dark conductance. Again, if one ignores (re)combination mechanisms, the same principle holds for the product of the yield and mobility.

This reasoning can be considered more intuitive, since figure 6.16 illustrates that when  $R_0$  decreases, a change in photoconductance ( $dG$ ) is accompanied by a relatively smaller change in power reflection coefficient ( $dR$ ) at resonance ( $R_0$ ).

In literature [48] the computationally absolute sensitivity (denoted in literature as  $KR_0$ ) determined for a comparative cavity cell is approximately  $dR/dG \approx 18,000$  at zero dark conductance. Again, this is however for a induced change in conductance of  $\Delta G = 1.0 \cdot 10^{-7}$  S, which is considered too low to yield any accurate results in this model.

### 6.3.3. Notes on previous work

Only one previous published paper has major significance in this thesis [48]. The cavity of the group used is significantly different. The variations in work will be discussed next to establish major differences between previous work and work done in this thesis.

1. A significant contact resistance at the joints of the waveguide and cavity cell has been included in previous work. This dominated the results of previous work. In this thesis, no need was found to include this. The geometry modelled was already sufficient to have comparative results to experimental results.
2. The relative permittivity of quartz used in previous work has a value of  $\epsilon_r = 3$ . This is too low in reality and significantly influences results. It shifts the resonance frequency quite significantly, and does not align with literature values found for quartz. Furthermore, the default value for quartz is  $\epsilon_r = 4.2$  in COMSOL. In this thesis, the default value of COMSOL has been used for the quartz window, with the quartz slide permittivity determined by calibration.
3. The geometries of the model described in previous work differs from the cavity used in this thesis.
4. In previous work the sample is placed on the other side of the quartz. Hence, the sample location is even more different.
5. The loss tangent for quartz is quoted to be within a factor of 2. However this uses no references and can not easily be validated at the frequency used.
6. The iris has a quartz window at the inside of the cavity placed in contact with the iris blocking ambient air from entering the cavity in previous work. This will however significantly influence the standing waveform due to the higher permittivity of quartz compared to nitrogen. This hinders comparison
7. The modeled cavity walls in previous work are of copper and brass, having different conductive properties to the gold plated walls in this thesis.
8. The simulated change in conductance of  $\Delta G = 1 \cdot 10^{-7}$  S in previous work is likely not sufficient to stabilize the results of the FEM. To see where the model is inaccurate, one can look at figure 6.14. These low values of  $\Delta G$  significantly underestimate the  $K$  value. However, the model used in previous work might not have these issues, although this is unlikely.

However, the claim that the  $K$  factor is stable at conductances of the sample below  $\sim 10^{-5}$  S is correct and has been verified in this model. This corresponds to an reflection coefficient at resonance of approximately similar to the quartz slide used.

## 6.4. Simulation inaccuracies

The simulation in COMSOL introduces some inaccuracies inherent to a FEM analysis. A clear example of this is for example given in figure 6.16. Here, the numerically obtained different  $\Delta R_0$  for  $G < 5 \cdot 10^{-9}$  are in the order of  $10^{-13}$ . Since  $R_0$  is numerically calculated in the order of  $10^0$ , we should ignore these solutions. This is not the resolution in where an FEM is accurate, and it should not be treated as such. After the signal increases, the  $K$  factor and its corresponding derived values converge. It is possible to extrapolate the data of figure 6.15 and 6.16 to find the  $K$  factor for these values of  $R_0$ . This claim that the  $K$  factor for low values of  $R_0$  can be extrapolate is supported by the fact that the driving simulated electric field behind these power losses do converge and are stable in figure 6.13. This does show that the simulation is stable in these high  $R_0$  regions.

A less obvious inaccuracy of the FEM its inherent numerical errors always present. The error is loosely defined as the difference between the exact solution and the computed solution. Since the exact solution of this system is not known *a priori*, calculating the error exactly will not be possible. Although there are method to (approximately) quantify the errors present without knowing the exact solution, these will not be given here. A short description of some of the errors present in the model of this thesis are as following:

1. Modelling errors in the model, these are deliberately introduced to simplify the model [35]. Here an example is the perfectly matched layer simulating the outside of the cell, replicating the outside environment.

2. Formulation errors, materials not behaving (exactly) as described by the model applied. Within this model, a bulk conductivity in a thin film is simulated. However, there are indications that the morphology of a sample, such as the crystalline domain size of the individual grains have an effect on the mobility of the samples [49]. Furthermore, the equations governing the characteristics are described in chapter 4.4 might vary from experimental conditions.
3. Numerical errors, such as truncation errors when calculating numerical derivatives/integrals. These kind of errors will propagate through the system. Furthermore, round-off errors exist due to computers having finite precision [35].
4. Iteration errors, by the iterative solver, relating to the beforehand specified relative tolerance for which a solution is considered converged [35]. An example of this is the numerical obtained results for small values of  $R_0$ .

## 6.5. Influence of electric field strength

The effect of the supplied power on the TRMC traces has been investigated by varying the power supplied by the microwave source. The goal of this experiment is to establish if there is any experimental dependence on the supplied microwave power on the signals. The measurement taken at maximum power output  $P_i \approx 160$  mW was repeated subsequently to verify the stability of the laser. All measurements are taken in (relatively) quick succession to account for further setup drift. All the powers shown in this section is the power measured at  $R_0$ . Here, both the samples are a cesium methylammonium formamidinium (CsMAFA) perovskite thin film sample deposited on a quartz substrate with a varying average grain size as shown in appendix G.

The fraction of absorbed light for both samples is approximately equal for both samples, as shown in appendix F. A constant value for  $K = -64,000$  has been chosen to allow better comparison. Furthermore, the assumption has been made that the  $n$  factor relating the voltage to the power has been properly calibrated in-house. These results are shown in figures 6.17 - 6.20.

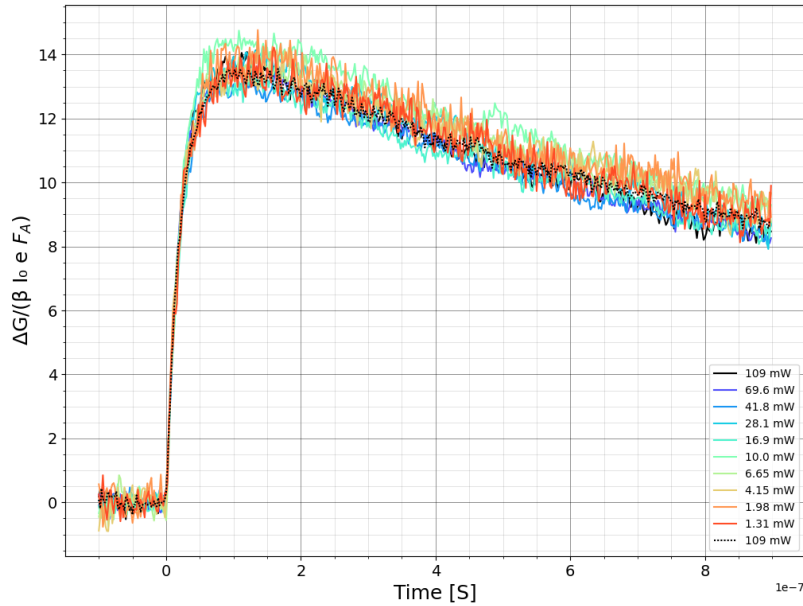


**Figure 6.17:** TRMC traces with the power varied between 109 mW and 1 mW, sample with an average grain size of 100 nm.

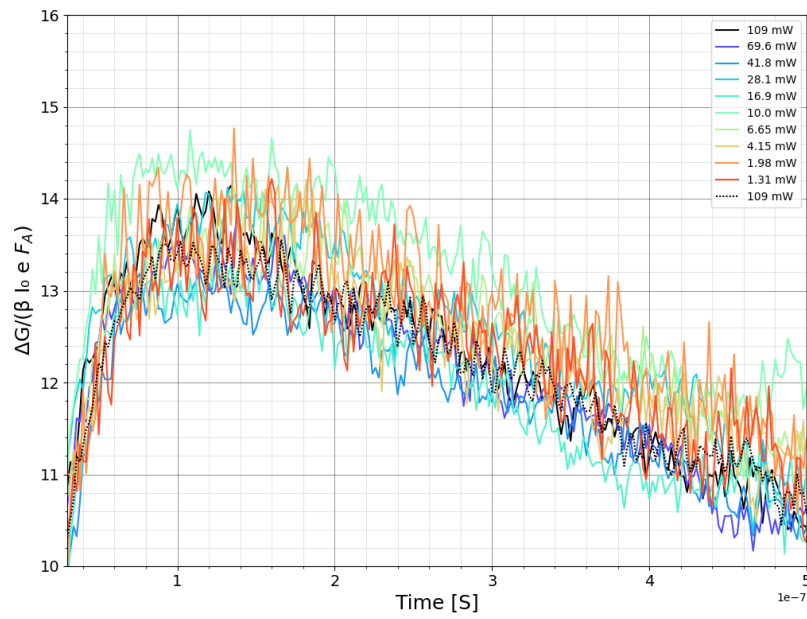


**Figure 6.18:** TRMC traces with the power varied between 109 mW and 1 mW, zoomed in on the maximum of the traces. Sample with an average grain size of 100 nm.

One can deduce from figure 6.17 and 6.18 that for the sample with the smaller grain size, there does not seem any dependence on the measured signals when the power is varied. Furthermore the baseline traces measured at maximum power seem to overlap, indicating that the laser power outputted was possibly stable during this measurement period.

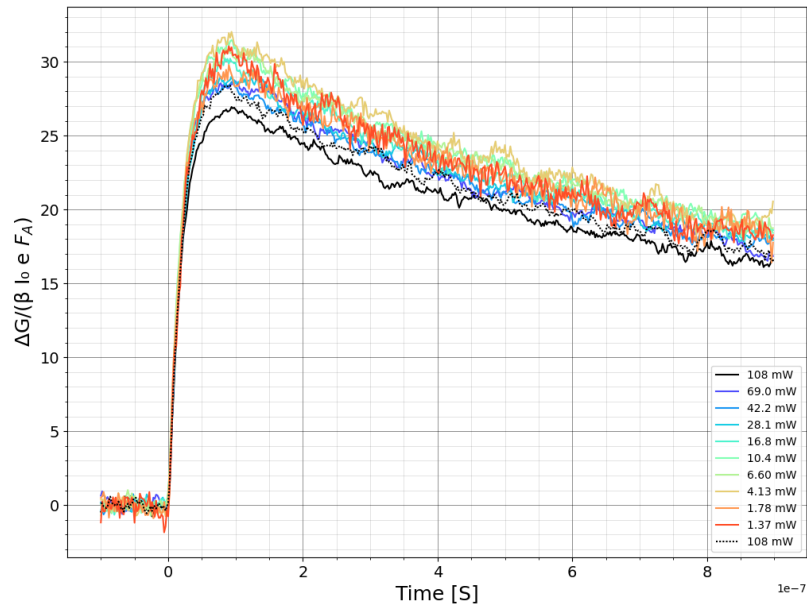


**Figure 6.19:** TRMC traces with the power varied between 108 mW and 1 mW, sample with an average grain size of 200 nm

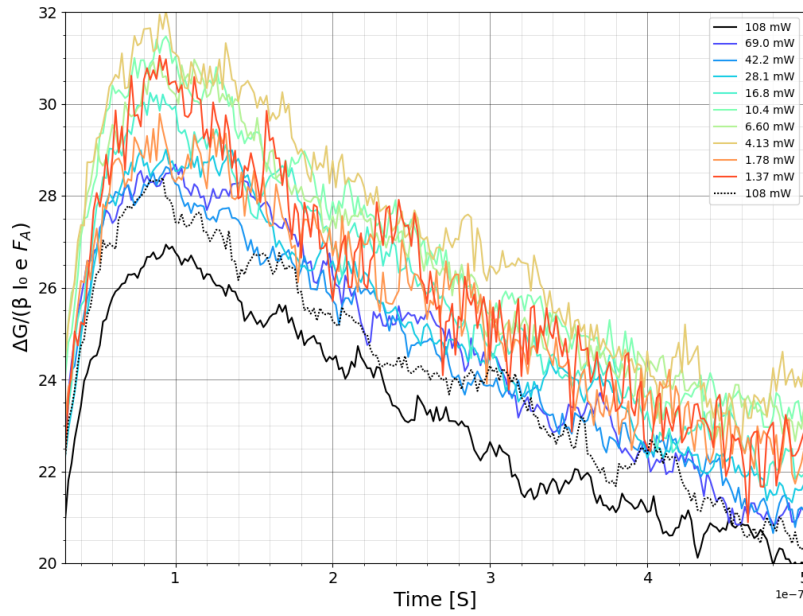


**Figure 6.20:** TRMC traces with the power varied between 108 mW and 1 mW, zoomed in on the maximum of the traces. Sample with an average grain size of 200 nm

For the sample with a bigger grain size, there does seem to be some dependence on power present, the signals seem to increase at first, before finally decreasing at powers below 4.13 mW. The measurements to establish a baseline at maximum power do not seem to overlap. This indicates that the laser has likely been unstable during these measurements.

Some more work has done to see how the SSMC behaves during a measurement. Some frequency scans have been measured for the sample with smaller average grain size. The results of these measurements are shown in appendix E. In previous measurements, some instrument drift has been found when normalizing each scan to the endplate measured at maximum power. To account for instrument drift, all normalization measurements involving the endplate have been conducted directly after measuring the sample at the (identical) measured power. In the region of resonance, no dependency on the measured power has been found. However there does seem to be some discrete switching present in the SSMC signals when measuring at lower powers. The effect of this on the measured TRMC traces is not clear. It is from these results regarding power variation unclear whether there is a dependency between the  $K$  factor and the power supplied to the cavity, if the sample exhibits different characteristics when subjected to varying power levels, or if the measurement setup is not stable enough to measure these characteristics.

Since literature has shown that the mobilities measured using TRMC are dependent on the average grain sizes [49], this could translate to the fact that some charge carriers transport properties might display a dependence on the relationship between electric field strength in the cavity and the morphology of the sample. This might be due to a higher electric field strength inducing a higher net movement of charges, being influenced by the morphological structure. Some samples have shown a dependence on electric field strength, but these results are inconclusive. Furthermore, the data in appendix E does suggest that the  $n$  values obtained in equation 3.3 might be too coarsely interpolated at these low powers, or some other property is inducing a discrete switching in the signal. This switching in the SSMC signal might also be present in the TRMC traces, but could be hidden by the averaging done internally by the TRMC to denoise the signal. Furthermore, the increase of the maximum product of the yield and mobility seems to be non-monotonic, while it is expected to be monotonic [49]. Moreover, the laser power seems unstable during these measurements, hindering accurate measurements.

Lastly, it is possible that the sample has degraded during the measurements, this has however not been confirmed. Hence, the results varying the power of the microwave source should be treated with care.

## Conclusion

In this thesis, a numerical model of the cavity cell used during SSMC and TRMC measurements is created. Furthermore, this model is used to model a thin film sample, allowing the frequency and conductance response to be studied numerically. This allows properties to be probed that are usually up to some degree unknown, such as electric field strength and distribution. The model has only been evaluated for a reference quartz slide with specific dielectric properties.

### 7.1. Electric field distribution

Using the model, the electric field distribution was studied for an empty cavity, a cavity with a quartz slide and a cavity with a quartz slide with a numerical method of modelling a thin film sample as a boundary condition. The insertion of the quartz slide will introduce a perturbation of the electric field distribution when compared to the empty cavity, changing the location of the anti-nodes. The modelled thin film sample has a thickness of 250 nm and a computationally varying conductivity. Furthermore, the electric field strength was obtained at the location of the sample. For low dark conductances, the electric field strength along the middle of the sample is approximately 17,800 V/m. Lastly, the electric field strength is relatively independent on dark conductance, however when increasing the dark conductance to a value of  $1.0 \cdot 10^{-6}$  S, the electric field strength starts to decrease significantly. This is matched by the reflection coefficient at the resonant frequency, decreasing when the dark conductance is in the order of  $10^{-6}$  S.

### 7.2. K factor for high dark conductance

To relate these steady state properties obtained to the TRMC technique, the  $K$  factor is calculated. For the specific quartz plate studied, the  $K$  factor obtained for a sample with no dark conductance equates to  $-64,000$ . The  $K$  factor is decreasing when the dark conductance is increased. This indicates that an equally measured signal at different dark conductances, represents a lower photoconductance for the signal induced by the sample with the lower dark conductance. Furthermore, the absolute sensitivity  $dR/dG$  has been obtained for the specific quartz plate studied. The absolute sensitivity obtained for a sample with no dark conductance is  $-42,000$ . The absolute sensitivity shows a different effect than the  $K$  factor. The absolute sensitivity increases linearly when the dark conductance increases. The characteristics of the  $K$  factor for high dark conductance can hence be attributed due to  $R_0^{-1}$  approaching infinite when dark conductance is high. A main drawback of modelling only the steady state solutions is that the actual time dependent response of the cavity is not studied. Modelling in a time dependent domain is advised to account for damping of the system. This damping will either overshoot or undershoot the measured maximum signal, possibly influencing the measured TRMC signals.

### 7.3. Power dependency on signal strength

To establish whether there is any dependence on the incidence power on the measured TRMC signals, the source power by the microwave generator has been varied and TRMC measurements have been carried out while attempting to keep the laser power stable. The goal was to establish whether there

is any dependency on electric field strength and grain size. There might be some dependency based on the samples measured, however the results are inconclusive. One sample of CsFAMA did display some characteristic behaviour when varying the power of the microwave generator. However, these results were nonmonotonic. Furthermore, the baseline TRMC measurements conducted at maximum power before and after varying the power are not equal, indicating that the power of the laser has drifted during the experiment. Moreover, it is possible that the sample has degraded during the measurements. Finally, a SSMC measurement seems to indicate that there might be some discrete switching in power supplied, or measured, when decreasing the power of the microwave generator. A second sample measured however, did not indicate any power dependency on the measured TRMC signal. During this experiment, no power drift was measured after conducting the baseline experiments. This however, does not rule out that the power of the laser has not drifted during the measurements and hence, these results should be treated with care.

## 7.4. Summary

The derived parameters in this thesis are all quantitative and can be used to derive quantitative results for thin film samples. This thesis serves as a second step in the global academic effort to quantify TRMC data, supporting research in thin film samples and hopefully contributing to higher efficiency photovoltaic devices. The first step, established by Reid et al., provides the foundational basis, although there may be variations in results and geometry and some critique on this previous work. Nonetheless, this thesis aims to assist in thin film sample research. Now, the research questions posed in chapter 1 will be explicitly addressed.

**What is the electric field distribution in the resonant microwave cavity used during SSMC and TRMC measurements.**

The figures of the electric field distribution can be found in section 6.2.1. Furthermore, the anti nodes are unevenly spaced due to the higher permittivity of the quartz slide. Lastly, the electric field strength is approximately 17,800 V/m and relatively indifferent for a conductance below  $10^{-6}$  S. When increasing the conductance further, the electric field starts to decrease. Lastly, when the power reflection coefficient at resonance is zero, the electric field strength is approximately 10,000 V/m.

**What is the  $K$  factor of this resonant microwave cavity and how is this influenced by dark conductance of the sample?**

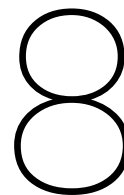
The  $K$  factor of the microwave cavity studied is  $-64,000$  at zero dark conductance. During a single measurement, the  $K$  factor can be considered constant. Once the power reflection coefficient at resonance starts to decrease due to an increase in dark conductance, the  $K$  factor starts to decrease as well. When the power reflection coefficient at resonance starts to approach zero,  $K$  starts to approach minus infinity. This asymptotic behaviour can be explained due to the factor  $R_0^{-1}$  present in the determination of the  $K$  factor, dominating the  $K$  factor. However, all these values are derived for a specific quartz slide with a permittivity of 4.0 and loss tangent of  $3.1 \cdot 10^{-4}$ .

**What is the absolute sensitivity of this resonant microwave cavity and how is this influenced by dark conductance of the sample?**

The absolute sensitivity of the microwave cavity studied is  $-42,000$  at zero dark conductance. Once the power reflection coefficient at resonance starts to decrease due to an increase in dark conductance, the absolute sensitivity starts to increase approximately linearly to 0. This shows opposite characteristics to the  $K$  factor. Again, all these values are derived for a specific quartz slide with a permittivity of 4.0 and loss tangent of  $3.1 \cdot 10^{-4}$ .

**How does the electric field strength in the resonant microwave cavity influence the measured signals during a SSMC and TRMC measurement?**

Electric field strength does not significantly influence the measured signals. Although there is possibly some dependency, from this research it can be concluded that the  $K$  factor does likely not require the need for an electric field strength term. However, to accurately study the dependency of grain size on measured mobilities, more research is required.



## Outlook

Some further work can be conducted to further close some gaps and obtain further information from the developed model. Some of these will be related to experimental work, allowing closer examination of the work and some of these will be related to further modelling.

### 8.1. Time dependent studies

The actual time dependent characteristics of the cavity cell perturbed by a transient change in photoconducance, followed by a period of relatively longer recombination mechanisms, has not been studied. Only the steady state solution is considered, while it is not studied how long it takes to establish an equilibrium. Since this resonant cavity can be considered an RLC or RL circuit [45] [56], unstudied time dependent parameters exist that influence the time response. For example, the damping characteristics affecting the TRMC signal have not been studied. A transient in photoconducance will perturb the system, forcing it to find a new equilibrium [7]. The type of damping, dependent on the system, will influence how the cavity will return to its equilibrium and in turn the TRMC signal. This is of great importance, as the observed charge carriers dynamics is affected too, as well as its interpretation. A schematic of this is shown in figure 8.1.

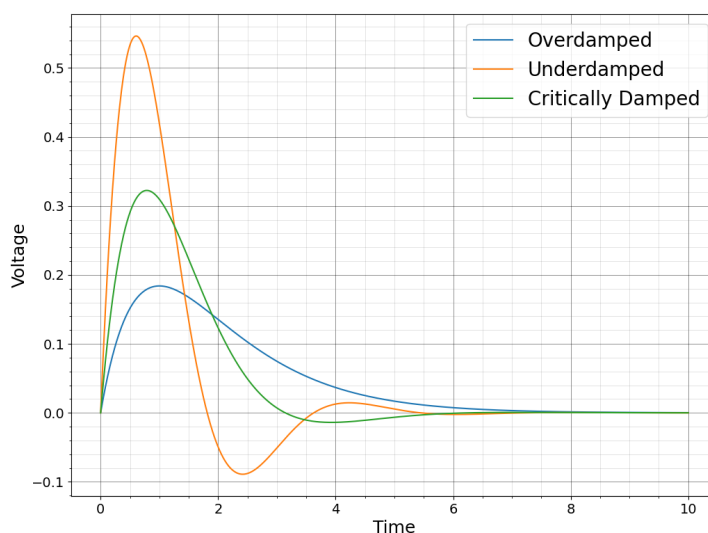


**Figure 8.1:** Response of a example RLC circuit based on the damping factor. The amplitudes have been exaggerated to highlight the response better. An underdamped system will overshoot and undershoot during a transient response, while a critically damped system will show very little harmonic behaviour. Finally, the overdamped system respond less strong to a transient, since this system takes longer to establish an new equilibrium.

It is of importance to continue validation for time dependent studies. This can likely be achieved using the current existing model build. Some adjustments could be made, such as studying the time domain instead of frequency domain. This should include modelling a time dependent conductance, and studying the power reflection coefficient over time. This will allow some more insight in the characteristics of the system when it is perturbed from its steady state solutions. However, ideally this would require more information from the system, such as the impedance of the microwave generator and further knowledge on the diode and detection system. Furthermore, it might require all the existing waveguides to be modelled. However, it is also likely that the model built in this thesis can be used to numerically approximate the cavity and its quartz slide as a RLC circuit [45] [56]. This allows a numerical or analytic solution to the time dependent domain to be constructed, without the need to explicitly model time dependent changes in (photo)conductance. Since time domain solutions will likely be computationally costly, it is recommended to first try to use the model to approximate an equivalent electrical circuit, allowing either numerical or analytic solutions to be calculated.

## 8.2. Experimental validation

To validate the modelling, it is advised to conduct experimental work. One could increase the dark conductance via means of degradation due to ambient air [42], light soaking [64], adding a steady state light source or other methods to increase the steady state conductance. This allows experimentally obtained TRMC signals to be scaled accordingly with the  $K$  factor obtained in this thesis. This could also shed insight in the  $K$  factor when it approaches low values of  $R_0$ . To validate the model ideally a sample should be used that can vary in dark conductance while not changing in opto-electronic properties.

## 8.3. Power dependency on signal strength

There is some indirect indication in literature that there is a dependency on grain sizes and microwave power [49]. Although this relation has not been confirmed in this thesis, a method is proposed to study this relation better.

Firstly, the laser power should be stabilized. The current setup shows a drift in laser power, hindering conclusions. This could be achieved by for example switching the TRMC setup, or the laser itself. An attempt has already been made to speed up the measurement as fast as possible to reduce possible instrument drift, but this was insufficient.

Secondly, preferably different grain sizes should be studied. Literature has shown that at varying laser fluence and a microwave power of approximately 100 mW, the yield-mobility product starts to increase at an average grain size of 4 nm and already starts to settle at an approximately steady state value at around 200 nm. In future research, it is recommended to use samples with a smaller grain size than studied in this thesis.

Lastly, different laser fluences should be researched. In this thesis, a single laser fluence has been studied. Different laser fluences might yield different results since the boundaries may act as traps for charge carriers. Different laser fluences, while varying the microwave power, might reveal some trapping dynamics [49].

# References

- [1] Minhaz Abedin. “A self-adjusting lin-log active pixel for wide dynamic range CMOS image sensor”. PhD thesis. Oct. 2015. DOI: 10.13140/RG.2.1.3871.8965.
- [2] Anton Akhmerov and Toeno van der Sar. *Open Solid State Notes*. [Accessed on 2023-05-19]. TU Delft. URL: <https://solidstate.quantumtinkerer.tudelft.nl/>.
- [3] Linus Andersson. *Fillet Away Your Electromagnetic Field Singularities*. <https://www.comsol.com/blogs/fillet-away-your-electromagnetic-field-singularities>. [Accessed on 2023-02-01]. Dec. 2014.
- [4] Nitin Bangera. “Development and validation of a realistic head model for EEG”. In: (Jan. 2008).
- [5] Noel Black and Shirley Moore. *Generalized minimal residual method*. <https://mathworld.wolfram.com/GeneralizedMinimalResidualMethod.html>. [Accessed on 2023-04-20].
- [6] Bladiebla. *File:vector ruimte.png - Wikimedia Commons*. [https://commons.wikimedia.org/wiki/File:Vector\\_ruimte.png](https://commons.wikimedia.org/wiki/File:Vector_ruimte.png). [Accessed on 2023-05-14]. Jan. 2018.
- [7] Kirt Blattenberger. *Transient (damped) responses*. <https://www.rfcafe.com/references/electrical/damped-response.htm>. [Accessed on 2023-05-22].
- [8] R. Brenot et al. “Time resolved microwave conductivity measurements for the characterization of transport properties in thin film micro-crystalline silicon”. In: *Thin Solid Films* 296.1 (1997). European Materials Research Society 1996 Spring Meeting, Symposium B: Thin Film Materials for Large Area Electronics, pp. 94–97. ISSN: 0040-6090. DOI: [https://doi.org/10.1016/S0040-6090\(96\)09377-7](https://doi.org/10.1016/S0040-6090(96)09377-7). URL: <https://www.sciencedirect.com/science/article/pii/S0040609096093777>.
- [9] Marc Burgelman et al. “Modeling thin-film PV devices”. In: *Progress in Photovoltaics: Research and Applications* 12.2-3 (2004), pp. 143–153. DOI: <https://doi.org/10.1002/pip.524>. eprint: <https://onlinelibrary.wiley.com/doi/pdf/10.1002/pip.524>. URL: <https://onlinelibrary.wiley.com/doi/abs/10.1002/pip.524>.
- [10] Helena Cano García. “New methods for determining the complex permittivity of different glucose concentrations by waveguide and antenna measurements at v-band”. PhD thesis. 2013.
- [11] V.M. Caselli. “Revealing loss and degradation mechanisms in metal halide perovskite solar cells: The role of defects and trap states”. English. PhD thesis. Delft University of Technology, 2022. ISBN: 978-94-6421-953-1. DOI: 10.4233/uuid:f8361576-f35d-4334-8bee-68a48ed70037.
- [12] Qianyu Chen. “The King of the New Generation Photovoltaic Technologies——Perovskite Solar Cells & the Opportunities and Challenges”. In: *IOP Conference Series: Materials Science and Engineering* 926.1 (Sept. 2020), p. 012010. DOI: 10.1088/1757-899X/926/1/012010. URL: <https://dx.doi.org/10.1088/1757-899X/926/1/012010>.
- [13] COMSOL. *Fabry–Perot Resonator*. [https://cn.comsol.com/model/download/840681/models.woptics.fabry\\_perot\\_resonator.pdf](https://cn.comsol.com/model/download/840681/models.woptics.fabry_perot_resonator.pdf). [Accessed on 2023-05-18].
- [14] COMSOL. *RF Module User’s Guide*. COMSOL 5.6. COMSOL.
- [15] COMSOL. *Understanding and Changing the Element Order*. <https://www.comsol.com/support/learning-center/article/Understanding-and-Changing-the-Element-Order-64391>. [Accessed on 2023-05-20].
- [16] Matthijs P. De Haas and John M. Warman. “Photon-induced molecular charge separation studied by nanosecond time-resolved microwave conductivity”. In: *Chemical Physics* 73.1 (1982), pp. 35–53. ISSN: 0301-0104. DOI: [https://doi.org/10.1016/0301-0104\(82\)85148-3](https://doi.org/10.1016/0301-0104(82)85148-3). URL: <https://www.sciencedirect.com/science/article/pii/0301010482851483>.
- [17] TU Delft. *HPCWiki*. [Accessed on 2022-10-01]. TU Delft. Oct. 2021. URL: <https://hpcwiki.tudelft.nl/>.

- [18] Steven W. Ellingson. *Electromagnetics, vol 2*. Virginia Tech Publishing, 2020.
- [19] Mathilde Fievez et al. "Slot-die coated methylammonium-free perovskite solar cells with 18% efficiency". In: *Solar Energy Materials and Solar Cells* 230 (May 2021), p. 111189.
- [20] Walter Frei. *Simulation tools for solving wave electromagnetics problems*. <https://www.comsol.com/blogs/simulation-tools-for-solving-wave-electromagnetics-problems/>. [Accessed on 2023-02-01]. June 2015.
- [21] Walter Frei. *Using Perfectly Matched Layers and Scattering Boundary Conditions for Wave Electromagnetics Problems*. <https://www.comsol.com/blogs/using-perfectly-matched-layers-and-scattering-boundary-conditions-for-wave-electromagnetics-problems/>. [Accessed on 2023-05-20]. Jan. 2015.
- [22] Hanna Gothåll. *How to inspect your mesh in COMSOL Multiphysics*. <https://www.comsol.com/blogs/how-to-inspect-your-mesh-in-comsol-multiphysics/>. [Accessed on 2023-05-26]. July 2022.
- [23] *Guide to Frequency Domain Wave Electromagnetics Modeling*. June 2015. URL: <https://www.comsol.com/blogs/guide-to-frequency-domain-wave-electromagnetics-modeling/>.
- [24] B. Gyüre et al. "A time domain based method for the accurate measurement of Q-factor and resonance frequency of microwave resonators". In: *Review of Scientific Instruments* 86 (May 2015). DOI: 10.1063/1.4929865.
- [25] Charles R. Harris et al. "Array programming with NumPy". In: *Nature* 585.7825 (Sept. 2020), pp. 357–362. DOI: 10.1038/s41586-020-2649-2. URL: <https://doi.org/10.1038/s41586-020-2649-2>.
- [26] Colin Harrison. *Xming*. <http://www.straightrunning.com/XmingNotes/>. [Accessed on 2023-05-15]. Nov. 2007.
- [27] Anne&nbsp;Marie Helmenstine. *A table of electrical conductivity and resistivity of common materials*. June 2019. URL: <https://www.thoughtco.com/table-of-electrical-resistivity-conductivity-608499>.
- [28] J. D. Hunter. "Matplotlib: A 2D graphics environment". In: *Computing in Science & Engineering* 9.3 (2007), pp. 90–95. DOI: 10.1109/MCSE.2007.55.
- [29] Eline Hutter. "Revealing the Fate of Photo-Generated Charges in Metal Halide Perovskites". PhD thesis. 2018.
- [30] *Igor Pro Manual v9.00*. WaveMetrics, Inc., 2021.
- [31] E. Jensen. In: *Proceedings of the CAS - CERN Accelerator School: RF for Accelerators, Ebeltoft, Denmark, 8 - 17 Jun 2010*. CERN, 2011, pp. 259–277.
- [32] J. van Kan, A. Segal, and F. Vermolen. *Numerical methods in scientific computing*. Delft Academic Press, 2014.
- [33] Leo K. Lamontagne. *Band Structures and the Meaning of the Wave Vector k*. Santa Barbara: University of California.
- [34] Antti Lehtikoinen. *Second-order finite elements - why, how, and when*. Oct. 2017. URL: <https://www.anttilehtikoinen.fi/research-work/second-order-finite-elements/>.
- [35] Jie Liu, Matthias Möller, and Henk M. Schuttelaars. "Balancing truncation and round-off errors in practical FEM: one-dimensional analysis". In: *Computer Methods in Applied Mechanics and Engineering* 340 (2018), pp. 60–76.
- [36] H. Margenau et al. "Physical processes in the recovery of TR tubes". In: *Physical Review* 70.5-6 (1946), pp. 349–357. DOI: 10.1103/physrev.70.349.
- [37] R.H. Moore and Sunil Saigal. "Eliminating slivers in three-dimensional finite element models". In: *CMES. Computer Modeling in Engineering & Sciences* 7 (Mar. 2005).
- [38] COMSOL Multiphysics®. *AC/DC Module User's Guide*. Stockholm, Sweden: v. 5.6., 2022.
- [39] National Renewable Energy Laboratory. *Solar Cell Efficiency Chart*. <https://www.nrel.gov/pv/cell-efficiency.html>. Accessed: May 28, 2023.

- [40] Donald A. Neamen. *Semiconductor physics and devices: Basic principles*. 4th ed. McGraw-Hill Higher Education, 2012.
- [41] Richard Newell et al. "Global Energy Outlook 2021: Pathways from Paris". In: *Resources for the future* (June 2021).
- [42] Ryosuke Nishikubo et al. "Minute-Scale Degradation and Shift of Valence-Band Maxima of (CH<sub>3</sub>NH<sub>3</sub>)SnI<sub>3</sub> and HC(NH<sub>2</sub>)<sub>2</sub>SnI<sub>3</sub> Perovskites upon Air Exposure". In: *The Journal of Physical Chemistry C* 121.36 (2017), pp. 19650–19656. DOI: 10.1021/acs.jpcc.7b06294. eprint: <https://doi.org/10.1021/acs.jpcc.7b06294>. URL: <https://doi.org/10.1021/acs.jpcc.7b06294>.
- [43] Jong Mun Park. "Novel Power Devices for Smart Power Applications". PhD thesis. Institut für Mikroelektronik, 2004.
- [44] Jacob Johan Piet. *Excitonic Interactions in Multichromophoric Arrays*. DUP Science, 2001.
- [45] D. M. Pozar. *Microwave engineering*. 2nd ed. John Wiley & Sons, ., 1998.
- [46] Precisionmmw. *Waveguide dimensions PDF - Engineers Chart*. <https://precisionmmw.com/waveguide-dimensions-pdf/>. [Accessed on 2023-05-03].
- [47] Martin Prikryl. Mar. 2000. URL: <https://winscp.net/eng/index.php>.
- [48] Obadiah G Reid et al. "Quantitative analysis of time-resolved microwave conductivity data". In: *Journal of Physics D: Applied Physics* 50.49 (2017), p. 493002. DOI: 10.1088/1361-6463/aa9559.
- [49] Obadiah G. Reid et al. "Grain-size-limited mobility in methylammonium lead iodide perovskite thin films". In: *ACS Energy Letters* 1.3 (2016), pp. 561–565. DOI: 10.1021/acsenenergylett.6b00288.
- [50] Everything RF. *Waveguide Sizes | Dimensions & Cutoff Frequency*. <https://www.everythingrf.com/tech-resources/waveguide-sizes>. Accessed: June 3, 2023. year.
- [51] Tom J. Savenije et al. "Quantifying charge-carrier mobilities and recombination rates in metal halide perovskites from time-resolved microwave photoconductivity measurements". In: *Advanced Energy Materials* 10.26 (2020), p. 1903788. DOI: 10.1002/aenm.201903788.
- [52] Tom J. Savenije et al. "Revealing the Dynamics of Charge Carriers in Polymer:Fullerene Blends Using Photoinduced Time-Resolved Microwave Conductivity". In: *The Journal of Physical Chemistry C* 117.46 (2013), pp. 24085–24103. DOI: 10.1021/jp406706u. eprint: <https://doi.org/10.1021/jp406706u>. URL: <https://doi.org/10.1021/jp406706u>.
- [53] Tom J. Savenije et al. "Revealing the dynamics of charge carriers in polymer:fullerene blends using photoinduced time-resolved microwave conductivity". In: *The Journal of Physical Chemistry C* 117.46 (2013), pp. 24085–24103. DOI: 10.1021/jp406706u.
- [54] Olaf Schenk and Klaus Gärtner. "PARDISO". In: *Encyclopedia of Parallel Computing*. Ed. by David Padua. Boston, MA: Springer US, 2011, pp. 1458–1464. ISBN: 978-0-387-09766-4. DOI: 10.1007/978-0-387-09766-4\_90. URL: [https://doi.org/10.1007/978-0-387-09766-4\\_90](https://doi.org/10.1007/978-0-387-09766-4_90).
- [55] Steven H. Simon. *The Oxford Solid State Basics*. 2019 reprint. Oxford University Press, 2013.
- [56] Max Sucher, Jerome Fox, and Moe Wind. *Handbook of Microwave Measurements*. Vol. 2. Polytechnic Press of the Polytechnic Institute of Brooklyn, 1963.
- [57] Simon Tatham. *PuTTY: a free SSH and Telnet client*. <https://www.chiark.greenend.org.uk/~sgtatham/putty/>. [Accessed on 2023-05-18]. Apr. 2023.
- [58] TOSOH. *Optical Silica Glass*. South San Francisco.
- [59] TylerMSFT. *Namespaces (C++)*. Mar. 2021. URL: <https://learn.microsoft.com/en-us/cpp/cpp/namespaces-cpp?view=msvc-170>.
- [60] Nikon Glass Business Unit. *Nikon NIFS Series Synthetic Silica Glass*. Sagamihara.
- [61] Guido Van Rossum and Fred L. Drake. *Python 3 Reference Manual*. Scotts Valley, CA: CreateSpace, 2009. ISBN: 1441412697.
- [62] P. Vijaya and Niraja. *Resonators and waveguides - presentation*. Jan. 2017. URL: <https://slideplayer.com/slide/12812380/>.

- [63] Pauli Virtanen et al. “SciPy 1.0: Fundamental Algorithms for Scientific Computing in Python”. In: *Nature Methods* 17 (2020), pp. 261–272. DOI: 10.1038/s41592-019-0686-2.
- [64] C Lowell Watts et al. “Light soaking in metal halide perovskites studied via steady-state microwave conductivity”. In: *Communications Physics* 3.1 (Apr. 2020). DOI: 10.1038/s42005-020-0350-2.
- [65] Eric W. Weisstein. *Full width at half maximum*. <https://mathworld.wolfram.com/FullWidthatHalfMaximum.html>. [Accessed on 2023-04-30].
- [66] Andrew Zangwill. *Modern electrodynamics*. Cambridge University Press, 2018.
- [67] Jiachen Zhou and Jia Huang. “Photodetectors Based on Organic-Inorganic Hybrid Lead Halide Perovskites”. In: *Advanced Science* 5 (Sept. 2017), p. 1700256. DOI: 10.1002/advs.201700256.

# A

## Appendix A - Modelled geometry

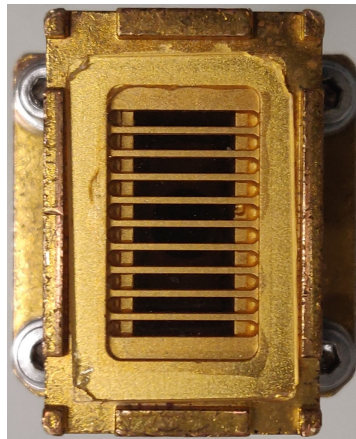
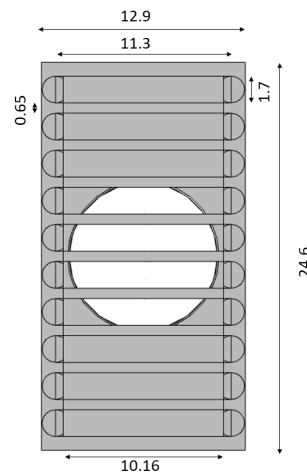


**Figure A.1:** Measured geometries of the inner wall dimensions with its corresponding outer dimensions of the cavity, side view A.

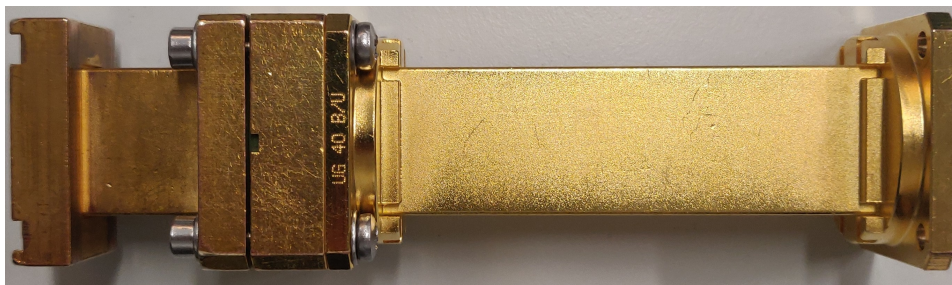
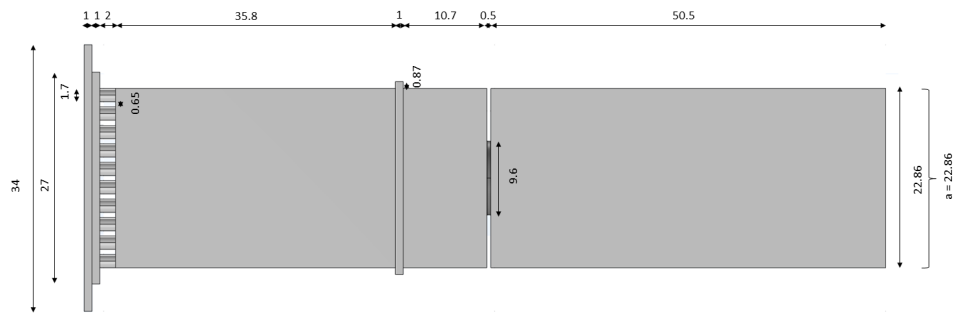


**Figure A.2:** Measured geometries of the inner wall dimensions with its corresponding outer dimensions of the cavity, side view B.

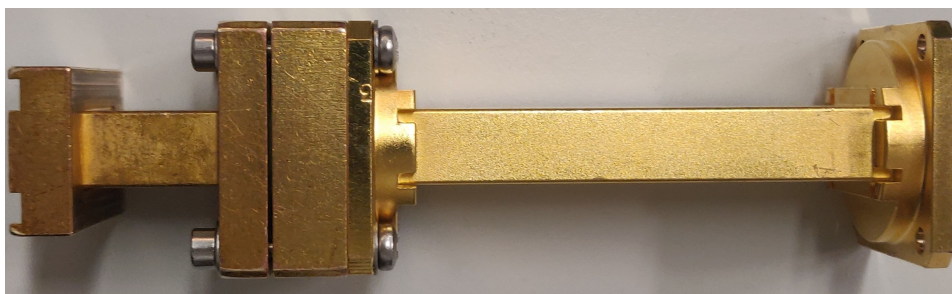
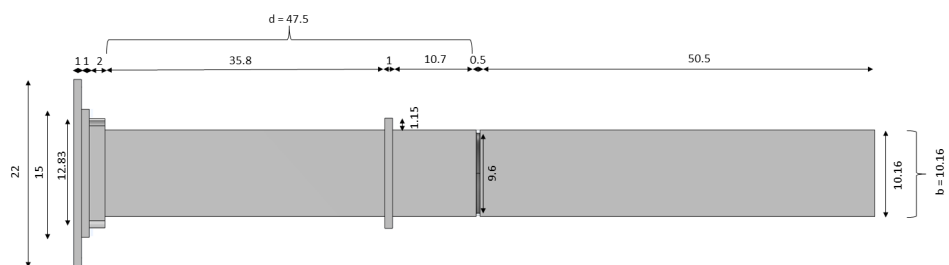


**Figure A.3:** Measured geometries of the inner wall dimensions with its corresponding outer dimensions of the cavity, side view C.

# B

## Appendix B - Example job script

```
1 #!/bin/bash
2
3 #PBS -l nodes=1:ppn=12:typh
4 #PBS -N "<PUBLIC_QUEUE_NAME>"
5 #PBS -q "cheme-om"
6 #PBS -o "${HOME}/logs/pbs.out"
7 #PBS -e "${HOME}/logs/pbs.err"
8
9
10 cd $PBS_O_WORKDIR
11 module load comsol/56
12 comsol batch -nn 1 -np 12 -inputfile <FILE_NAME.mph> -outputfile <FILE_NAME.mph>
```



## Appendix C - Cleaning of quartz slides

Recycled quartz slides have been randomly selected from various boxes to have as little bias as possible in the data. Furthermore some pristine quartz slides have been obtained from at least two different batches. To clean the quartz slides, the following procedure has been applied

- An ultrasound bath using acetone for 5 minutes.
- An ultrasound bath using isopropyl alcohol for 7 minutes.
- Drying in ambient air.
- Lint free cloth polishment.
- UV-ozone treatment for a minimum of 2 minutes.

A longer UV- ozone treatment of 8 minutes seemed to have no effect on the obtained SSMC signals.

# D

## Appendix D - Electric field distribution for various conductivities

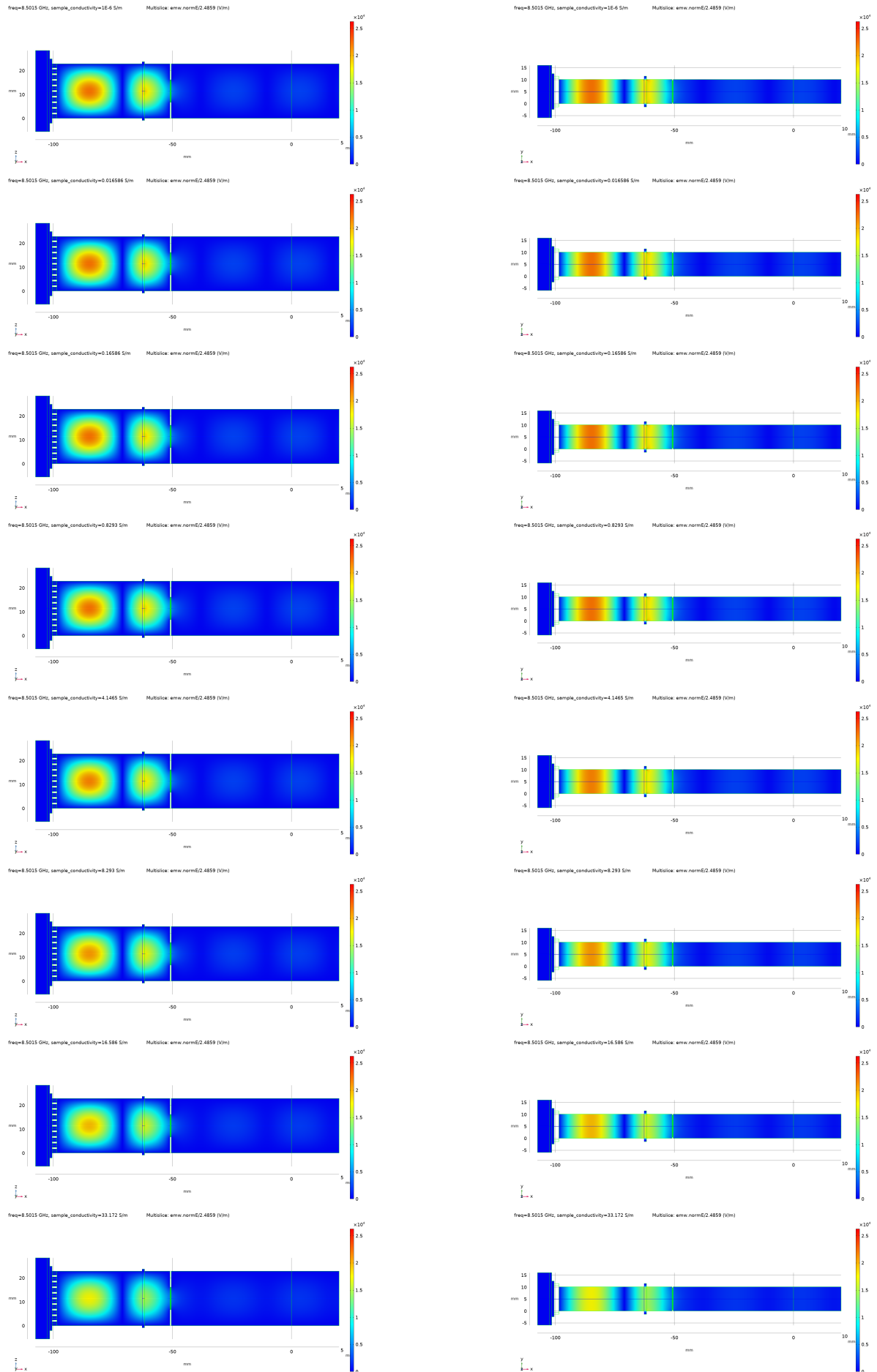


**Figure D.1:** Electric field distribution in the cavity cell for various conductivities. Units of the electric field are in V/m.

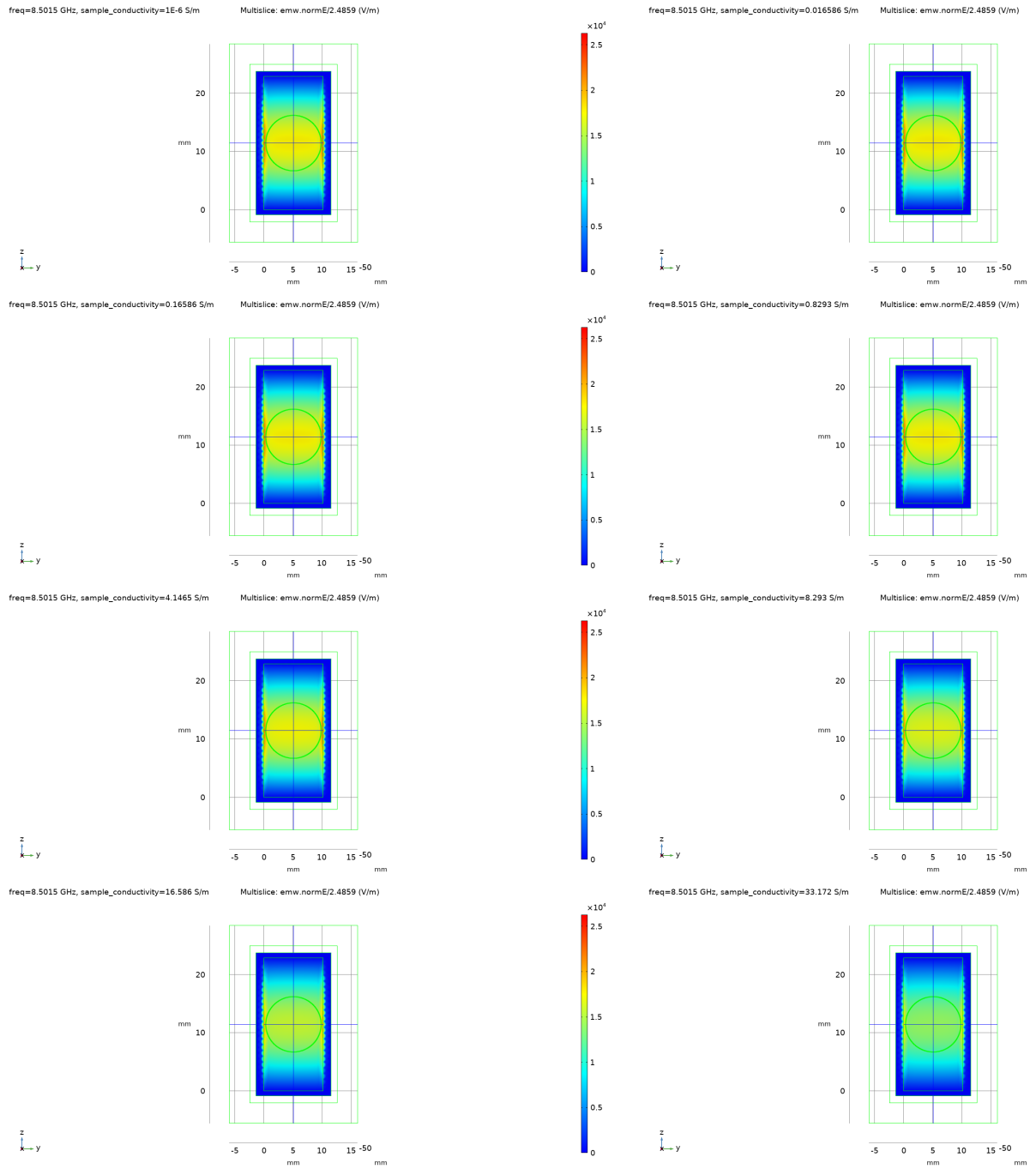


**Figure D.2:** Electric field distribution at the location of the sample for various conductivities. Steady State only. As the conductivity increases, the electric field decreases. Units of the electric field are in V/m.

# E

## Appendix E - SSMC at various powers

The steady state measurement at varying powers are shown in figures E.1 and E.2. These figures have some observations. It seems like some discrete switching is present in the measurement. This could be attributed to the fact that the  $n$  factor (see equation 3.3) might be coarsely interpolated, introducing discrete switching. Furthermore, there seems to be an artifact that is power dependent at around 9,35 GHz, highlighted in figure F.1

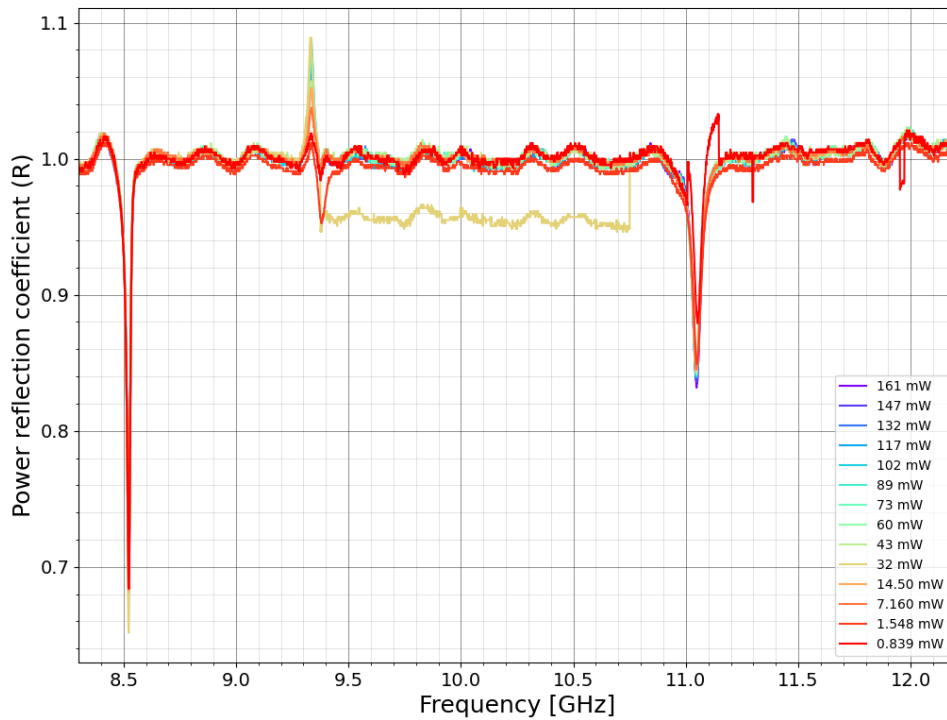


**Figure E.1:** SSMC measurements with varying microwave power.

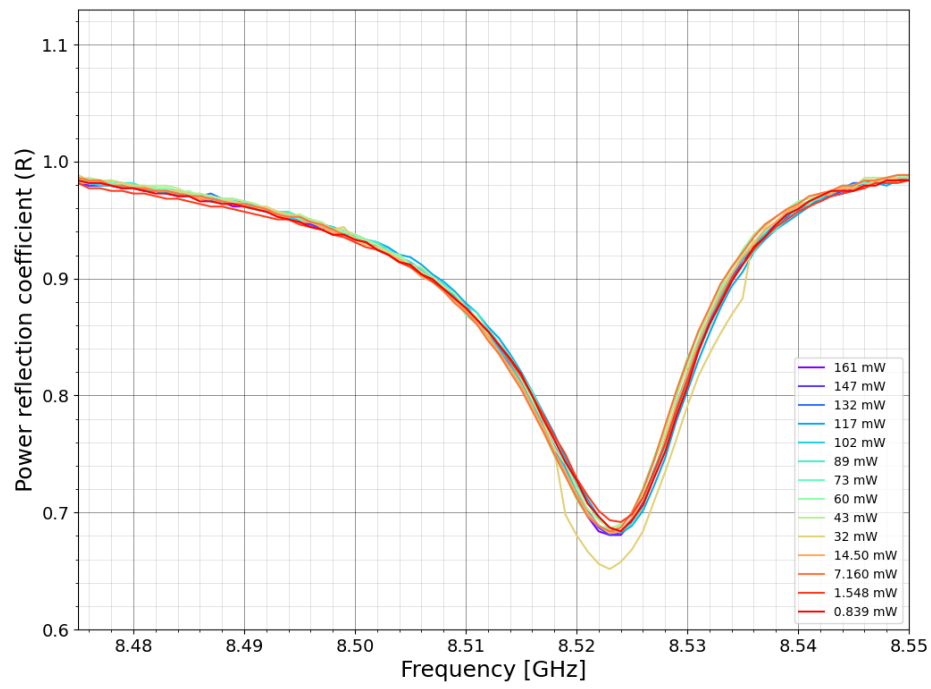


**Figure E.2:** SSMC measurements with varying microwave power, zoomed in on resonance.

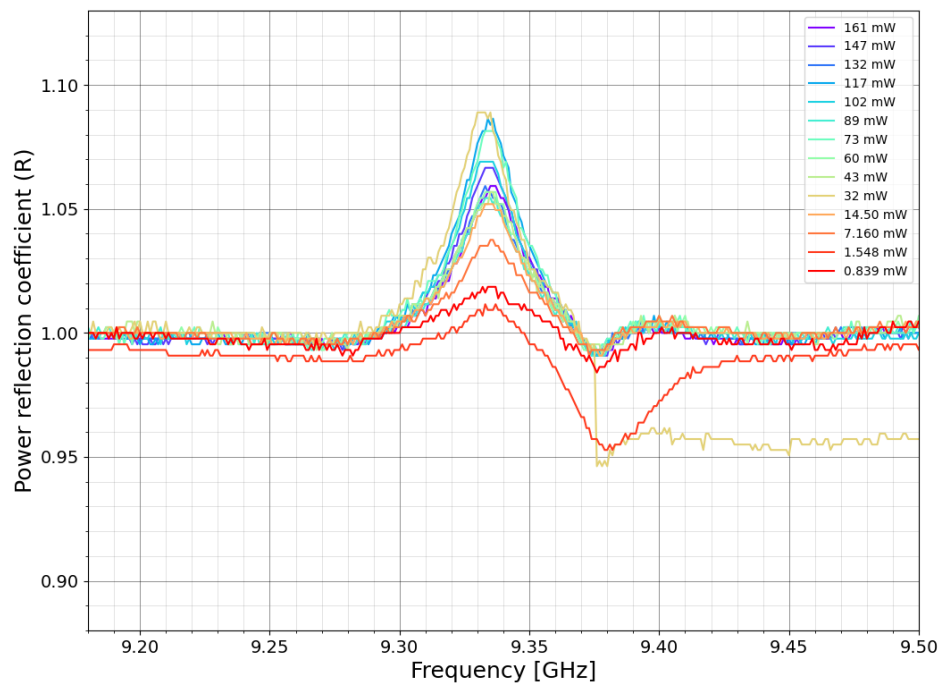


**Figure E.3:** SSMC measurements with varying microwave power, zoomed in on a point of interest that is power dependent.

# F

## Appendix F - Absorption spectra

The absorption spectra of the samples supplied in-house. The fraction of absorbed light is comparative for both samples. The photoluminescence is shown as well.

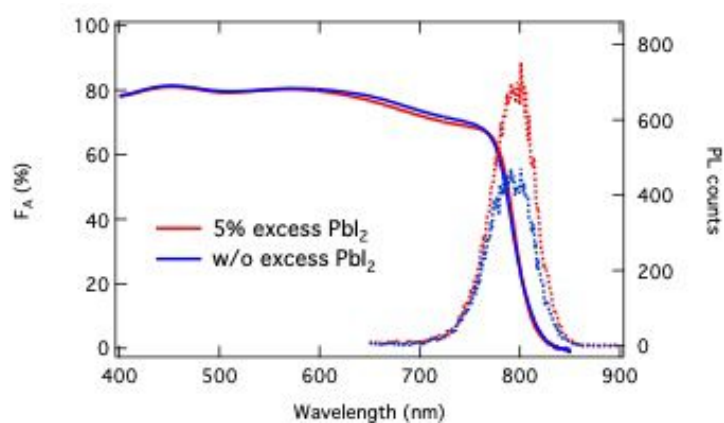


**Figure F.1:** Absorption spectra of the of the samples supplied-in house.

# G

## Appendix G - Domain sizes

The scanning electron microscope measurements of the samples supplied in house shown in figure G.1. The distribution of grain sizes is different shown in the overlay, showing a different distribution of grain sizes.

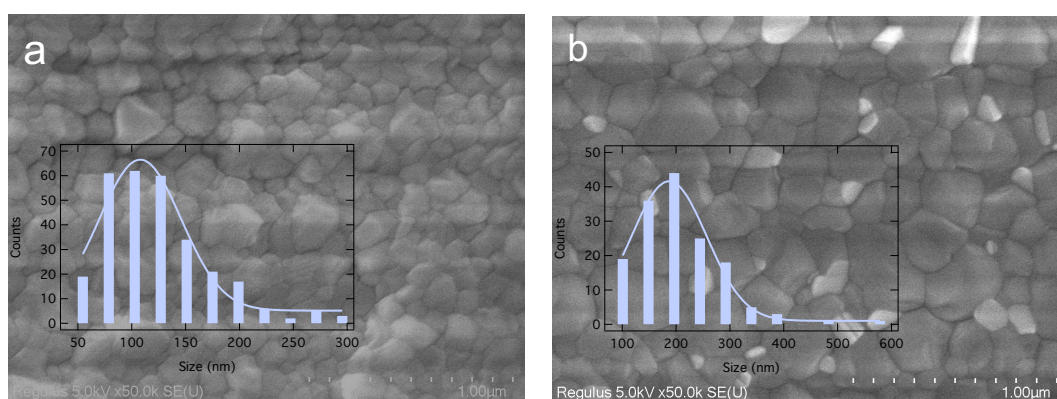


**Figure G.1:** (a) Scanning electron microscopy of a sample without excess  $\text{PbI}_2$ . (b) Scanning electron microscopy of a sample with 5% excess  $\text{PbI}_2$ .